Upconversion based mid-infrared hyperspectral imaging

Junaid, Saher

Publication date:
2018

Document Version
Publisher's PDF, also known as Version of record

Small changes in thesis after defence

- Section 1.6.1 , subsection External cavity configuration, first sentence is altered.
- Section 1.6.2, subsection OPG, equation 1.4 is added
- Section 2.1.1, equation numbers 2.15- 2.17 are corrected
- Section 2.1.7, equation 2.30 is altered
- Section 5.1, Table at the end of the section, last row, spatial resolution of upconversion imaging is changed.

Technical University of Denmark
Department of Photonics Engineering
Optical Sensor Technology

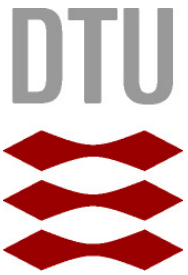

Upconversion based mid-infrared hyperspectral imaging

Saher Junaid

Submitted in partial fulfillment of the requirements for the degree of Doctor of Philosophy in Photonics Engineering of the Technical University of Denmark, November 2018.

Abstract

Hyperspectral imaging in the mid-infrared spectral range is an emerging technology utilized for a multitude of applications, but its full potential is held back by the lack of sensitive mid-IR detectors. Nonlinear frequency upconversion offers a promising alternative to direct detection for room-temperature mid-IR spectroscopy and hyperspectral imaging.

In this work, upconversion based hyperspectral imaging has been demonstrated in the 1 to 10 µm spectral domain using different kinds of illumination sources narrowband/broadband, continuous wave/pulsed, such as globar, Quantum Cascade Laser, Optical Parametric Oscillator and Supercontinuum source. Nonlinear media such as Lithium Niobate (birefringent and quasi phase matched) and Silver Gallium Sulfide have been exploited for sum frequency generation i.e. upconversion.

Large field of view and broad spectral coverage have been achieved using phase-matching scanning techniques such as temperature and angle tuning of a nonlinear crystal. Post-processing techniques have been developed for the construction of upconversion hyperspectral cubes based on both narrowband and broadband light sources.

A video-frame-rate upconversion imaging system is realized using a standard CCD camera, in synchronism with the crystal rotation of an upconversion system. This system is capable of acquiring 64 kpixel upconverted mid-IR images in 2.5 ms, without the need for post-processing. This approach is generic in nature and constitutes a major simplification in realizing video-frame rate hyperspectral imaging in the mid-IR.

Based on this setup, a pilot study on oesophageal tissues samples from a tissue microarray, is presented, in the 3 to 4 µm wavelength range using computer assisted classification. Comparing the stained sections evaluated by a pathologist to those obtained by either FTIR or upconversion hyperspectral imaging based on machine learning shows great promise for future research pointing towards potential clinical translation.

In the last phase of the project, point-spread function engineering in the upconversion process is presented. Dark field imaging of static and dynamic near-infrared phase objects is demonstrated – resulting in edge-enhanced upconverted images in the visible spectral

range. Through this scheme, the spiral phase filter operates at the pump wavelength rather than in the mid-IR signal wavelength which can potentially be broadband. This approach offers some advantages due to the lack of high-performance spiral phase filters and cameras operating at the signal wavelength (especially for mid-IR objects). Furthermore, upconversion dark field imaging is extended numerically and experimentally from collinear to non-collinear interactions between signal and pump.

Resumé

Hyperspektral billeddannelse i det midt-infrarøde spektralområde er en teknologi med stort potentiale inden for en lang række anvendes, men dets fulde udnyttelse begrænses af manglen på følsomme midt-IR detektorer. Ikke-lineær frekvenskonvertering er et lovende alternativ til direkte detektion i det infrarød område, specielt ved stuetemperatur midt-IR spektroskopi og hyperspectral billeddannelse.

I dette arbejde demonstreres frekvenskonversionsbaseret hyperspektral billeddannelse i 1 til 10 µm området, baseret for forskellige former for belysningskilder smalbånds/bredbånds, kontinuerlige/pulsede, såsom termiske kilder, kvante kaskade lasere, optisk parametriske oscillatorer og supercontinuum-kilder. Ikke-lineære materialer såsom lithium niobate og sølv gallium sulfid er benyttet til sumfrekvensgenerering, dvs. op-konversion.

Et stort synsfelt og bred spektraldækning er opnået ved anvendelse af fase-matchnings teknikker, baseret på temperatur og vinkel tuning af dobbeltbrydende ikke-lineær krystaller. Numeriske metoder til efterbehandling af billederne er udviklet til generering af hyperspektral information baseret på både smalbånds- og bredbåndslyskilder.

En system med fuld video hastighed, baseret på op-konversion billeddannelse er blevet realiseret ved hjælp af et standard CCD kamera, synkroniseret med rotationen af den ikke-lineære krystal. Med dette system er det muligt at optage monokromatiske infrarøde billeder med 64 kpixels på 2,5 ms, uden behov for efterbehandling af data. Denne fremgangsmåde er generisk af natur og medfører i en stor forenkling af fremtidige videobaserede hyperspektralt billeddannende systemer.

Baseret på dette system præsenteres en pilotstudie på vævsprøver fra spiserøret. Vævet afbilledes i 3 til 4 µm området og klassificeres ved hjælp af computer baserede algoritmer. Sammenlignes data med den tilsvarende analyse udført af en patolog baseret på traditionelt farvede biopsier, viser metoden stort potential for fremtidig computer baseret vævsanalyse til kliniske anvendelser.

I sidste del af projektet præsenteres arbejde med billedfiltreringsalgoritmer implementeret i billede op-konversion processen. Teknikker kendt fra mikroskopi testes på statiske såvel som dynamiske infrarød fasekontrast objekter. Dette resultere i op-konverterede billede

hvor fase-spring fremhæves i billeddannelsen. Baseret på spiral formede faseplader ved pumpe bølgelængden opnås afbildning af fasekontrasten i det infrarøde signal, hvorved der ikke behøves faseplader ved de infrarøde bølgelængder. Der præsenteres ligeledes både en numerisk model og praktisk realisering af fasekontrast billeder baseret på ikke co-lineær billeddannelses.

Acknowledgements

First of all I would like to thank my supervisors, Peter Tidemand-Lichtenberg and Christian Pedersen for always being there for the valuable discussions and ideas. I can not forget to mention Peter-John Rodrigo, who was more like an informal supervisor to me. Whether it was about discussing new ideas or working on complicated alignments in the lab, he never failed to inspire me through his skills. I would also like to thank my colleague Henning Engelbrecht Larsen for spending alot of time with me to polish my Labview skills. I would like to thank the whole ITN Mid-TECH network, specially Jan Tomko (Humboldt University Berlin), Chaitanya Kumar (ICFO, Spain) and Mahmoud Tawfieq (FBH, Berlin) for the great collaborative work. I would like to acknowledge my friend and fellow PhD, Morgan Mathez for making first half of my PhD more fun and for teaching a valuable lesson before leaving. In addition, I thank Thomas Niedereichholz of Hamamatsu for his assistance with the use of the LCOS-SLM and Peter M. Moselund of NKT Photonics for providing access to the SC source. Last but not the least, I would like to thank my husband for working on improving my programming skills.

Contents

List of Figures

1 Introduction

1.1 Publications

Journal publications

- **S. Junaid**, P. Tidemand-Lichtenberg, C. Pedersen, P. J. Rodrigo, "Point-Spread function engineering in Non-collinear upconversion imaging" (to be submitted).

- **S. Junaid**, S. Chaitanya Kumar, M. Mathez, M. Hermes, N. Stone, M. Ebrahim-Zadeh, P. Tidemand-Lichtenberg and C. Pedersen, "Video-rate, mid-IR hyperspectral upconversion imaging" (submitted, 2018).

- **S. Junaid**, J. Tomko, M. P. Semtsiv, J. Kischkat, W. T. Masselink, C. Pedersen, P. Tidemand-Lichtenberg, "Mid-IR upconversion based hyperspectral imaging", Opt. Express 26, 2203 (2018).

- M. Hermes, R. Brandstrup Morrish, L. Huot, L. Meng, **S. Junaid**, J. Tumko, G.R. Lloyd, W. T. Masselink, P. Tidemand-Lichtenberg, C. Pedersen, F Palombo and N. Stone, "Mid-IR hyperspectral imaging for label-free histopathology and cytology", J. Opt. 20 (2018).

Patent

- **S. Junaid** (inventor), P. Tidemand-Lichtenberg (inventor), C. Pedersen (inventor), "Wide field of view upconversion system" (Patent filed).

Conference contributions

- **S. Junaid**, P. Tidemand-Lichtenberg, C. Pedersen, "Upconverson based mid-IR hyperspectral imaging", Proc. CLEO EU, (2017).

- **S. Junaid**, P. Tidemand-Lichtenberg, and C. Pedersen, "Upconversion based

spectral imaging in 6 to 8 µm spectral regime", Proc. SPIE 10088, 100880I (2017).

- **S. Junaid**, P. J. Rodrigo, P. Tidemand-Lichtenberg, C. Pedersen, "Point-Spread Function engineering in upconversion imaging", OSA High brightness sources and light driven interactions congress, Strasbourg, France, March 2018.

- J. Tomko, **S. Junaid**, P. Tidemand-Lichtenberg, W. T. Masselink, "Novel mid-IR imaging system based on single-photon quantum cascade illumination and upconverson", CLEO EU, 2017.

- M. Hermes, J. Nallala, L. Huot, J. Tomko, **S. Junaid**, P. Tidemand-Lichtenberg, C. Pedersen, N. Stone, "Towards rapid high-resolution mid-IR imaging for molecular spectral histopathological diagnosis of oesophageal cancers", CLEO EU 2017.

1.2 Project Goals

This project is part of The Innovative Training network (ITN) MID-TECH project (Grant agreement 642661). The focus of the project is to further study and exploit mid-infrared (mid-IR) technology, in collaboration with several university and industrial partners.
The project is primarily consisting of three parts i.e., mid-IR sources, detection and applications. Our partners, NKT, Humboldt University Berlin, Ferdinand Braun Institute (FBH;Berlin) and The Institute of Photonic Sciences (ICFO;Spain), are responsible for mid-IR light sources in different spectral regimes interesting for specific applications. Exeter University, UK, and Lund University, Sweden, are working on the application part of the project. DTU is mainly working on the detection part of the project.

My project, in particular, is to exploit nonlinear frequency upconversion for mid-IR hyperspectral imaging primarily for medical diagnostics. Different kinds of mid-IR illumination sources provided by our partners, such as Supercontinuum source, Optical Parametric Oscillator and Quantum Cascade Laser, are studied and employed in combination with different nonlinear materials for upconversion.
In the first part of the project, the most basic mid-IR light source, a thermal black-body radiator i.e. a globar was used for broadband illumination in the 5 to 10 µm spectral regime. Spectral and spatial resolution of the upconversion imaging system were studied and a hyperspectral cube was constructed.

In the next step, the illumination source was replaced by a Quantum Cascade laser and the properties were studied and compared with that of the globar.
Furthermore, a pico-second pulsed Optical parametric oscillator in the 2 to 4 µm spectral

range was used as an illumination source, with synchronous pumping for high upconversion efficiency. This led to video-frame-rate upconversion imaging system. Biopsy samples were provided by our partner at Exeter University. Hyperspectral imaging of the cancerous and healthy tissue samples was conducted.

In the last part of the project, point spread function engineering in upconversion imaging was realized. Collinear and non-collinear phase-matching were studied for dark field imaging when using vortex pump beam. The principle was checked for both bulk and periodically polled crystal. Crystal angle and temperature tuning was employed to achieve a larger field of view.

1.3 Motivation

Mid-IR hyperspectral imaging is of major interest in diverse fields from medical diagnostics [1–5], to environmental monitoring [6–9], geology for mineral identification [10], and within the food industry [11]. The widespread applicability of the mid-IR wavelength range (e.g. 2 to 15 µm) is intimately linked to nature-given properties of molecular absorption, and includes the following main categories; (1) Vibrational spectroscopy used for unique identification of complex molecules such as food or tissue, (2) Gas spectroscopy characterized by fundamental band interaction between mid-IR light and most gaseous molecules including environmental gasses such as CH_4, CO_2, NO_X and SO_X, and (3) Sensing of heat radiation from room-temperature objects. Despite all the virtues of mid-IR spectroscopy and imaging, applications are in need of sensitive, fast detectors, and cameras operating at room-temperature [12].

Fourier Transform infrared (FTIR) spectroscopy is today the preferred technique for hyperspectral imaging in the mid-IR spectral range. A major limitation to FTIR imaging is that the cameras used for mid-IR detection are predominantly based on MCT (HgCdTe), InSb or microbolometers, which require cryogenic cooling for low-noise performance and are of high cost [6, 10–13]. Moreover, for hyperspectral imaging, large data storage and complex post-processing software is currently needed to transform raw data into useful information [14].
Nonlinear frequency upconversion provides an alternative route to fast, room-temperature mid-IR spectroscopy and imaging, due to orders-of-magnitude higher sensitivity and speed compared to direct mid-IR detectors [15].

Upconversion technology relies on converting the mid-IR signal to near-infrared (NIR)/visible (VIS) spectral regime, as illustrated in Fig. 1.1, and enables the use of NIR/VIS detectors/cameras which are cheaper and more sensitive.

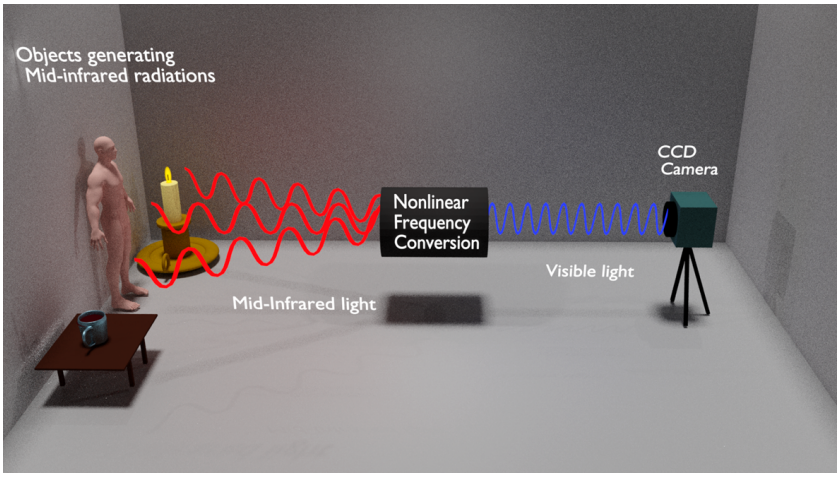

Figure 1.1: *Non-linear frequency upconversion.*

Figure 1.2 represents the detectivity D of the state-of-the-art detectors at different spectral regimes. It can be seen that the efficiency of the detectors drops towards mid-IR spectral domain whereas in the NIR and VIS spectral domain, detectors with higher detectivity and quantum efficiency are available. Therefore, converting mid-IR to NIR/VIS spectral domain via nonlinear frequency conversion is emerging as a promising technique for mid-IR detection with detectivity and quantum efficiency as high as that for VIS/NIR detectors.

1.4 Prior Work

Upconversion based mid-IR detection was first demonstrated in 1968 [16, 17] but was abandoned due to poor conversion efficiency. In 2012, upconversion based mid-IR detection was demonstrated again with improved conversion efficiency [15].
Upconversion detection has been employed so far, for both spectroscopy and imaging, used in both pulsed [18] and continuous wave [19, 20] configurations. Most work has been based on lithium niobate (LN) as the nonlinear medium, using either bulk [18, 21] or periodically poled [15, 19, 20, 22] crystals, however, applications of LN are limited by the transparency range of the material.

This work is the first demonstration of long wavelength infrared (IR) (5 to 10 µm), upconversion based hyperspectral imaging. Upconversion based hyperspectral imaging has been demonstrated before in 3 to 5 µm spectral domain only exploiting temperature tuning of the crystal which is a slow process [19].
In this work, a broadband illumination source i.e. a globar is used and an $AgGaS_2$ (AGS)

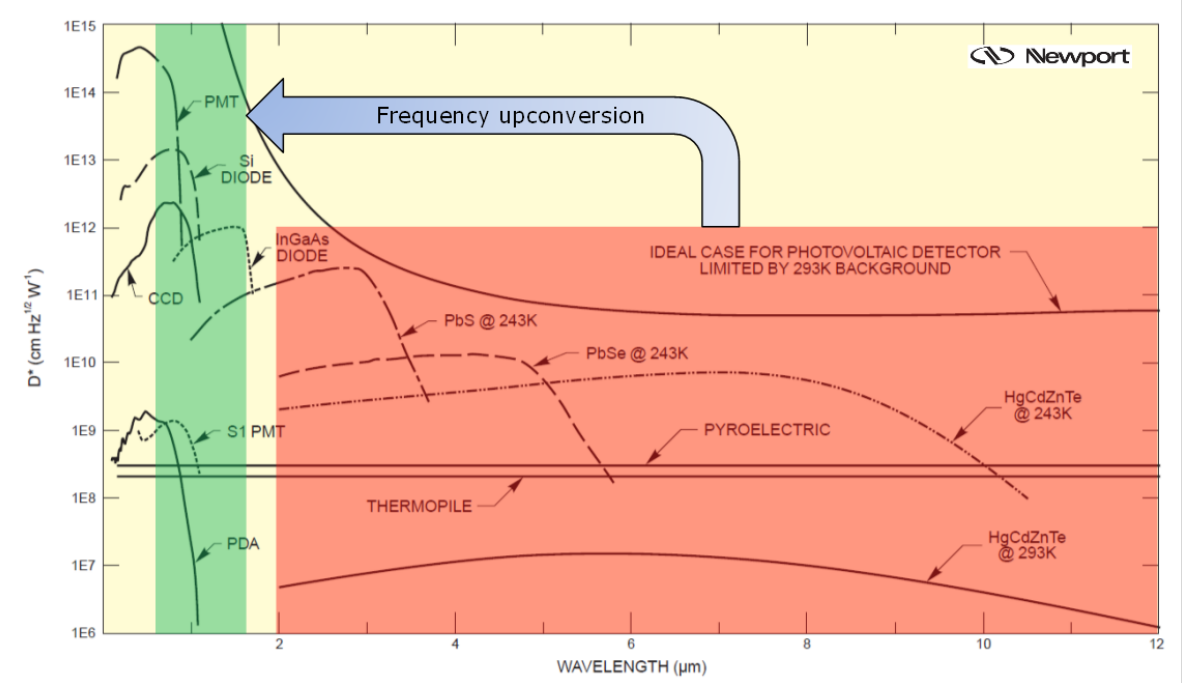

Figure 1.2: *Comparison of the detectivity of the state-of-the-art detectors being used in different spectral regimes.*

crystal is employed as the nonlinear medium. The post-processing algorithm to achieve a hyperspectral cube is developed.
Also, a video-frame-rate imaging system based on upconversion is realized and demonstrated. The system is based on synchronized pulsed light sources for higher conversion efficiency. Based on this system, imaging of the cancer biopsy is demonstrated with fast acquisition and high spatial resolution.
Point-spread function (PSF) engineering in upconversion has been demonstrated before, exploiting only collinear phase-matching [23, 24]. In this work, dark field imaging, based on upconversion, is presented exploiting collinear and non-collinear phase-matching. A periodically polled crystal is used with temperature tuning for extended field of view.

In the following section of the chapter, a theoretical description of the mid-IR light sources, used in this work is presented.

In the following chapter the upconverion theory is discussed with special focus on imaging aspect of upconversion technology.

In chapter 3, upconversion based hyperspectral imaging in 5 to 10 µm regime is presented using AGS as the nonlinear medium. A globar is used as a broadband illumination source and the post-processing algorithm is presented. In the later section, the globar is

replaced by a QCL. The comparison of the acquired upconversion hyperspectral cube is presented for the two illumination sources.

In chapter 4, Video-frame-rate upconversion hyperspectral imaging is presented where a picosecond pulsed OPO is used as an illumination source.

In chapter 5, the hyperspectral imaging of human tissue samples was is presented and the results are compared with FTIR based data.

Upconversion based point-spread function engineering is presented in chapter 6.

The last chapter summarizes this work with future prospects of the goals achieved during the project.

1.5 State-of-the-art mid-IR detectors

A primary limitation for widespread exploitation of the IR spectrum for imaging applications is associated with a lack of sensitive, robust and easy-to-operate detection systems. In comparison to visible detectors, mid-IR detectors generally suffer from noise originating from their own components emitting room-temperature black-body radiation; hence, low noise performance can only be achieved through cryogenic cooling. Cold shields can be used to minimize the contribution from black-body radiation from surrounding objects entering the detector.

Generally, light detection is based either on the absorption of photons by a sensor material resulting in a temperature increase which can then be detected (thermal detectors) or in the creation of electron-hole pairs giving rise to a current (photonic detectors). Both these principles are routinely used for IR detection and can be considered mature technologies optimised for decades. Nevertheless, these detectors are still hampered by the need for cooling resulting in high operational cost, complexity and size for low noise operation.

1.5.1 Thermal detectors

A thermal detector is based on the temperature increase produced by absorbed incident photons, which can be detected as a change in a temperature-sensitive physical property of the material. These detectors generally have slow temporal response, often in the millisecond range, set by the thermal relaxation time of the sensor material. The spectral

response of thermal detectors depends on the absorption characteristics of the material used. Thermal detectors are efficient for detection of high brightness signals, and can be operated without cryogenic cooling. One of the major sources of noise in thermal detectors relates to ambient thermal fluctuations transformed into a variation in the conductance of the sensor material. In general, thermal detectors need to have a low heat capacity for fast response time and good thermal isolation from the surroundings [12, 25]. Applications of thermal detectors are generally limited by their slow response time and lack of sensitivity, due to unwanted black-body radiation from surroundings and temperature fluctuations in the detector material particularly in the non-cooled versions. Thermal detectors are divided into different categories based on the physical property responsible for generating the output signal in response to the temperature variation. Two commonly used thermal detectors are presented below.

Bolometers

The bolometer is a widely used thermal detector in which the incident radiation is absorbed in the sensor material, increasing the temperature of the material relative to the surroundings. The sensor material has a temperature-dependent electrical resistance, which can be read out as a voltage when passing a current I through the bolometer. The voltage V can be expressed as:

$$\Delta V = IR\alpha\Delta T \qquad\qquad \alpha = \frac{1}{R}\frac{\mathrm{d}R}{\mathrm{d}T} \tag{1.1}$$

where α is the temperature coefficient of electrical resistance R of the sensor material that determines the sensitivity of the bolometer. Preferred materials for bolometers should have low heat capacity, low room-temperature resistance and a large thermal coefficient of resistance. IR imaging in the long wavelength regime, e.g. 8-14 µm, can be achieved using microbolometer arrays. These arrays typically consist of 320×240 pixels, however larger arrays with 640×512 pixels are emerging. The individual pixel dimension is of the order of 20×20 µm^2; however, as the pixel size decreases and thus the number of pixels per unit area increases, a larger noise-equivalent temperature difference results due to smaller pixels being less sensitive to IR radiation [26].

Thermopiles

The thermopile is another type of thermal detector, where the temperature change is measured through a series of thermo-coupled devices. An infrared absorption film is deposited on one side of the junction of a thermopile consisting of a series of thermocouple

pairs. Each pair has a junction of two conductors on either side of a thermal resistance layer, resulting in a voltage in the range 10-100 mV proportional to the temperature difference,

$$\Delta V = N\left(\alpha_a - \alpha_b\right)\Delta T \tag{1.2}$$

where α_a and α_b are the Seebeck coefficients (the magnitude of an induced thermoelectric voltage in response to a temperature difference across that material) of the two conductors forming the junction of the thermocouple pair, N is the number of thermocouple pairs and ΔT is the temperature difference caused by the absorbed IR radiation. The sensitivity and the frequency response of thermopiles are inferior to bolometers, nevertheless thermopiles are cost-efficient and have found several applications in the medical, farming and automotive industry [12, 25].

1.5.2 Photodetectors

The working principle of photodetectors is based on the photon absorption in a semiconductor material resulting in an electronic transition generating a free charge carrier. The bandgap of the semiconductor dictates the working wavelength range. Silicon (Si) is the preferred material for detectors in the visible and NIR range, between 350 and 1100 nm. Moving towards longer wavelengths, indium gallium arsenide (InGaAs) is the detector material of choice covering the range between 0.85 and 1.7 µm [27]. Indium antimonide (InSb) can be used in the range 3 to 5 µm, whereas mercury cadmium telluride (MCT) is commonly used in the wavelength ranges 3 to 5 and 8 to 12 µm [12, 28]. Generally, Si and InGaAs detectors can have very high quantum efficiency reaching more than 90%, thus approaching single photon counting sensitivity, and have a rise time in the order of 10-100 ps. In contrast, InSb and MCT based detectors typically have rise times in the order of 10-100 ns or more. The low bandgap energy of the IR detector has a great impact on the noise performance, both in terms of internal noise as well as sensitivity to black-body radiation originating from the detector surroundings. In practical applications where high sensitivity is needed, the InSb and MCT detectors are actively cooled in order to obtain low noise levels.

InGaAs and InSb detectors

Si and InGaAs detectors are divided into PIN diodes and avalanche photodiodes (APD). In both cases the detector operates in the reverse-biased region, which is known as photoconductive mode. The APDs work in the high voltage reverse-biased region, where the signal-to-noise ratio can be improved by the internal current gain due to the avalanche effect. APDs can be applied for single photon detection when operating in the Geiger

mode. Generally for all detectors, there is a trade-off between high quantum efficiency, low noise and high bandwidth. InGaAs can also be applied for NIR imaging. Compared to silicon-based cameras used for visible light imaging, the InGaAs cameras typically suffer from higher dark current and larger readout noise as a result of the lower bandgap. InSb photovoltaic detectors reach further into the mid-IR than InGaAs systems and cover the wavelength range from 1 to 5.5 µm [29]. They can be operated at room-temperature but with poor noise performance and require to be cooled with liquid nitrogen like MCT detectors. Their noise performance is better than for MCT but as their spectral coverage is smaller, they are not often used for biomedical imaging applications.

MCT based detector

MCT is an alloy composed of CdTe and HgTe. The absorption wavelength is determined by the amount of Cd in the alloy. MCT detectors can cover a relatively large wavelength range (2 to 12 µm), which makes them good candidates for FTIR spectrometers. MCT detectors have better performance than thermal detectors in terms of speed and noise, although they are still inferior to InGaAs detectors. However, MCT detectors have been the detector of choice for mid-IR wavelengths, to which the InGaAs detectors are insensitive. The bandgap of MCT is smaller than that of InGaAs allowing it to detect longer wavelengths; however, this is also the main reason for the higher noise level. In practical applications, MCT detectors are usually actively cooled (peltier, stirling cooler or liquid nitrogen) in order to reduce the noise.

1.5.3 Mid-IR hyperspectral imaging

Hyperspectral imaging (HSI) can be described as a combination of imaging and spectroscopy, since the images acquired in HSI contain both spatial and spectral information. In HSI, the full spectral information is measured for each pixel element of the image. Figure 1.3 is the schematic representation of hyperspectral imaging where x and y are spatial coordinates and λ represents wavelength.

HSI in the mid-IR range is a promising tool for a wide range of applications in medical diagnostics [30]. The traditional approach for mid-IR hyperspectral imaging is FTIR using Focal Plane Array (FPA) detectors [5, 13].
FTIR utilizes Fourier transformation to retrieve a spectrum from the measured data. Broadband light sources, such as globars are typically used in combination with a Michelson interferometer. The light coming from the source is split in two parts using a beam splitter, directing 50% of the light to the fixed mirror and the rest of the light

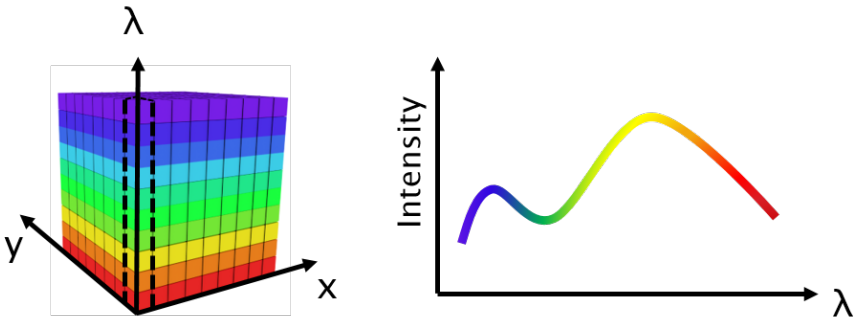

Figure 1.3: *Schematic demonstration of hyperspectral imaging.*

to the movable mirror. The light reflected from the mirrors interferes and directed to the sample and then detected to achieve the transmission spectrum of the sample. The movable mirror of the interferometer is moved in small steps with respect to its zeros position (the position of the movable mirror which corresponds to zero path delay between the light reflected from both of the mirror/arms of the interferometer), which leads to slightly different spectra at every step of the movable mirror. Fourier transformation is utilized to retrieve the spectrum from the acquired data [31]. A 2D array of mid-IR detectors i.e. FPA is typically used in combination with FTIR for mid-IR imaging. As mentioned earlier, the traditional detectors used for mid-IR imaging are MCT-based detectors [12].

1.6 Mid-IR illumination sources

The light sources are of primary importance in mid-IR imaging. The most common illumination source used for mid-IR imaging is a globar, which is a thermal light source based on silicon carbide heated to a temperature between 1000 °C and 1650 °C to produce black-body radiations according to Planck's law [12]. Globar is the cheapest source of broadband light, incoherent in nature and provides low brightness. Supercontinuum sources are also important candidates offering high brightness over a broad spectral range, however possesses high spatial coherence which gives speckles when used for imaging applications. Also, narrowband light sources such as Quantum Cascade Lasers and Optical Parametric Oscillators are of significant importance due to their high brightness and broad wavelength tunability. In the next section, the light sources used in this work are briefly discussed.

1.6.1 Quantum Cascade Laser (QCL)

QCLs are one of the main laser sources which can emit in mid to far infrared spectral regime. A wavelength range of 2.63 µm to 250 µm has been achieved so far [32]. The first QCL was reported in 1994 at 4.2 µm gives peak power of 8 mW [33]. QCLs are made of semiconductor material but are different from typical semiconductor lasers and rely on intersubband transitions based on periodic heterostructures Fig. 1.4. The QCL is pumped by injecting a current to the QCL chip enabling the electrons to move to the upper laser level in the conduction band. The transition of electrons from the upper to the lower level produces electromagnetic radiation with a wavelength depending on the transition band gap. In this process, electrons after undergoing radiative transitions, tunnel to the next period of the cascade and emit radiation again. This allows the quantum efficiency of the QCL to be greater than 100% [34]. By suitable engineering of the material layers of the cascade, population inversion between the two sub-bands can be achieved, which is required for laser emission [35, 36]. Since the emission wavelength is mainly dependent on the layer thickness of the cascade and not the material itself, a wide spectral range can be covered from the same material.

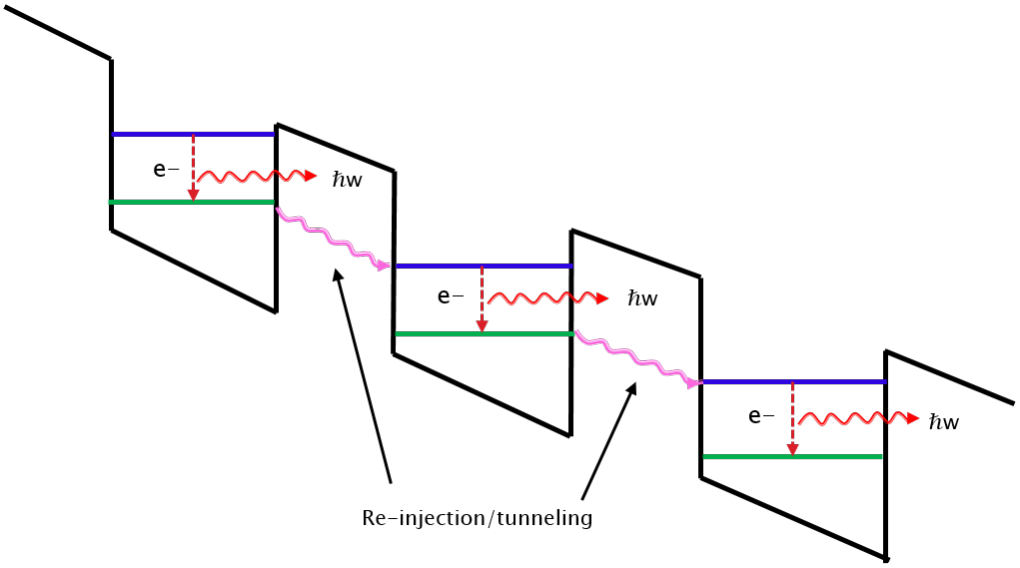

Figure 1.4: *Schematic figure depicting the cascade structure with electron intersubband transitions and photon emission. The figure also demonstrates the electron tunneling to the next period of the structure.*

In typical realizations, the quantum cascade gain medium is formed into a waveguide structure inside an optical cavity [37–39]. The most popular optical cavity types are discussed in the following:

i. Fabry-Perot The general form of a QCL is in a Fabry-Perot resonator configuration, formed by making a resonator of the gain medium waveguide. This is done by cleaving the end surface of the waveguide for feedback thus creating a resonator. In Fabry-Perot mode, the output spectrum of the QCL is about 10% broader than its central peak where the central peak is dependent on the design of the QCL [40].

ii. Distributed feedback A diffraction grating can be etched on the gain medium to provide feedback in a narrow spectral regime thereby providing single mode output. This provides a spectral tuning range of only 1% of the central wavelength which is implemented by exploiting temperature tuning of the grating. However, several gratings of different grating periods can be used to increase the tuning range [41].

iii. External cavity A QCL can also be realized with an external cavity configuration, where a simple Fabry-Peror laser is mounted in an external cavity. An anti-reflection coating on the chip facets is required in this case. A wavelength selection element, such as a grating, can be used for spectral tuning [42].

The QCL used in this work is in external cavity configuration and is described in more detail in section 3.2.

1.6.2 Optical Parametric Oscillator (OPO)

OPOs, which are based on χ^2 nonlinear processes, are one of the important sources for mid-IR light generation. The first theoretical demonstration of an OPO was done by R. H. Kingston in 1962 [43] while J. A. Giordmaine presented the first experimental OPO in 1965 [44] using $LiNbO_3$ crystal pumped by 0.529 µm, with output spectrum ranging from 0.97 to 1.15µm at the peak power of 6.4 kW.

Recently, OPOs are emerging as powerful mid-IR light sources and can be exploited for several applications due to their ability to generate output with wide spectral tunability, high brightness and several temporal domains (Continuous-wave to femtosecond pulses) [45]. The working principle of an OPO can be explained in a two step process, (i) Optical Parametric Generation (OPG), (ii) Optical Parametric Amplification (OPA).

i. OPG OPG, also called spontaneous parametric down conversion, is a nonlinear process in which a pump photon when incident on a nonlinear medium, splits into two lower

energy photons, i.e. signal ω_s and idler ω_i which has to follow the law of conservation of energy and momentum;

$$\omega_p = \omega_s + \omega_i \tag{1.3}$$

$$k_p = k_s + k_i \tag{1.4}$$

The wavelengths of the signal and idler are also determined by the phase-matching condition (described in detail in the following section) which is typically tuned by temperature tuning Fig. 1.5(a).

ii. OPA Based on difference frequency generation, OPA can amplify the signal photons ω_s when two beams are used as input with optical frequencies of ω_p and ω_s and also generate idler photons of ω_i. In the process of OPA, signal photons ω_s get amplified while idler photons ω_i are generated to obey the law of energy conservation (Eq. (1.3)). The phase-matching condition has to be fulfilled for the process to be efficient.

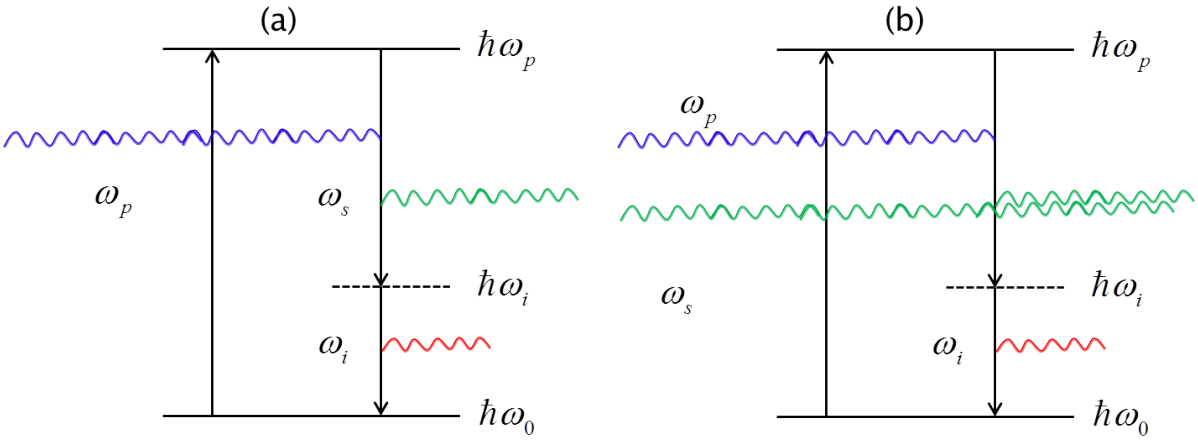

Figure 1.5: *(a) Optical parametric generation and (b) Optical parametric amplification.*

An OPO can be setup by exploiting the combination of OPG and OPA i.e. A nonlinear crystal, such as periodically poled lithium niobate (PPLN) is pumped with an intense pump field which generates signal photons ω_s and idler photons ω_i as a results of OPG Fig. 1.5(b). If the generated signal photons are used as a feedback using high reflective mirrors, i.e. constructing a resonator around the nonlinear medium, the signal photons can be amplified as a results of OPA and idler photons ω_i are generated.

By exploiting temperature tuning or angle tuning of the nonlinear crystal, the phase-matched condition is altered resulting in spectral tuning of the generated fields. An

OPO resonator can be singly or doubly resonant based on the feedback to the nonlinear medium [46].

2 Background Theory

2.1 Upconversion theory

Upconversion is referred to a as a process of converting two photons with lower energies into one photon with a higher energy. The process of upconversion is a second order nonlinear process, i.e. sum frequency generation (SFG) where light of lower frequency is mixed with a pump field and gives rise to light of higher frequency which is equal to the sum of the incoming light frequencies;

$$\omega_{up} = \omega_p + \omega_s \tag{2.1}$$

or

$$\frac{1}{\lambda_{up}} = \frac{1}{\lambda_p} + \frac{1}{\lambda_s} \tag{2.2}$$

where, λ_{up} (ω_{up}) is the wavelength (frequency) of the upconverted light, λ_s (ω_s) is the signal wavelength (frequency) and λ_p (ω_p) is the pump field wavelength (frequency).

$$\vec{k}_{up} = \vec{k}_p + \vec{k}_s \tag{2.3}$$

Here, Eq. (2.3) represents momentum conservation or phase-matching condition. For nonlinear frequency upconversion both the conditions of Eq. (2.2) and 2.3, i.e. energy and momentum conservation, have to be fulfilled for the process to be efficient. The wavelength of the upconverted light is strictly determined by the energy conservation.

Figure 2.1 shows collinear and non-collinear phase-matching which are also called scalar and vector phase-matching. In the case of collinear interaction (commonly used in OPOs), the wave vectors of the beams are directed in one direction while in non-collinear phase-matching, the incident beams are at different angles but still phase-match for a particular frequency. When the phase-matching condition is fulfilled, the field emitted by the individual atomic dipoles that constitute the material adds up coherently in the forward direction [46].

The most common way of achieving phase-matching is to exploit the birefringence (i.e. dependence of the refractive index on the polarization direction of the light field) of the

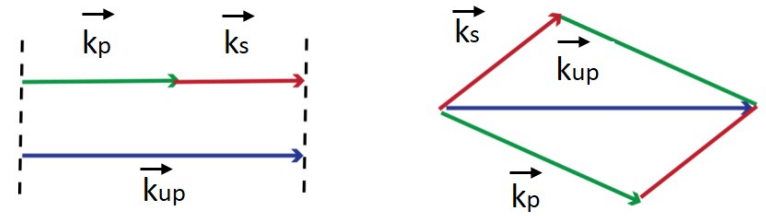

Figure 2.1: *Wave vector $\vec{k}_{up}$ is the wave vector for upconverted field and $\vec{k}_p$ and $\vec{k}_s$ represent the wave vector for the pump and signal field respectively (left) collinear and (right) non-collinear phase-matching.*

material. By carefully controlling the polarization and direction of propagation of all interacting fields, proper phase-matching can be achieved. Typically, angle tuning or temperature tuning of the nonlinear crystal is exploited to achieve phase-matching [19, 47]. In this work, we have utilized both temperature and angle tuning of the nonlinear crystal.

Figure 2.2 demonstrates the relationship of the collinearly phase-matched wavelength with the crystal rotation angle, for the pump wavelength 1064 nm, an AGS crystal with a cut angle of 48° for type-II phase-matching.

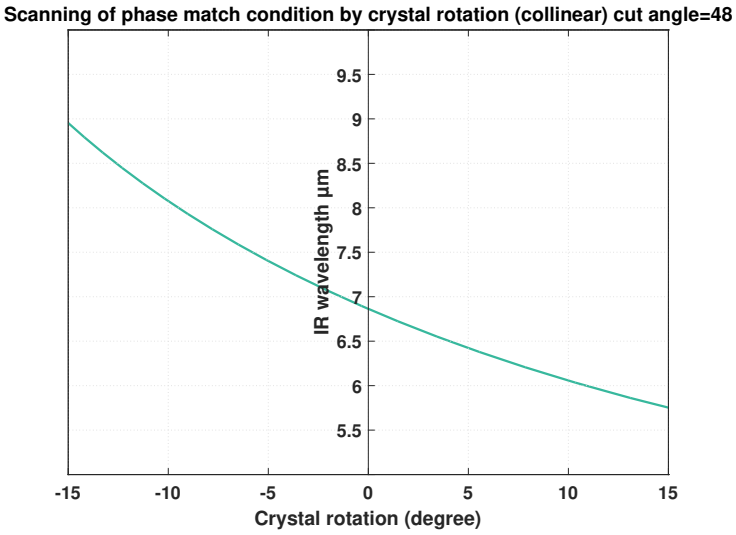

Figure 2.2: *Phase-matched wavelength vs. crystal rotation angle for collinear phase-matching only. The curve is plotted for AGS crystal with a cut angle of 48° using pump field at 1064 nm wavelength.*

Equation 2.4 is used to calculate the collinear phase-matching curve depicted in figure 2.2 where n_o is the ordinary refractive index and $n_e(\theta)$ is the extraordinary, angle dependent refractive index of the respective optical field which can be calculated as [46];

$$\Delta k = 2\pi \left(\frac{n_{o,p}}{\lambda_p} + \frac{n_{e,s}(\theta)}{\lambda_s} - \frac{n_{e,up}(\theta)}{\lambda_{up}} \right) \tag{2.4}$$

$$\frac{1}{n_e^2(\theta_i, \lambda_i)} = \frac{\sin^2(\theta_i)}{n_e^2(\lambda_i)} + \frac{\cos^2(\theta_i)}{n_o^2(\lambda_i)} \tag{2.5}$$

Here, n_e and n_o are principle extraordinary and ordinary refractive indices, respectively, and can be calculated using the Sellmeier equations. Subscript i is used to denote 'up', 's' or 'p' optical fields.

2.1.1 Birefringent non-collinear phase-matching

In this section, the derivation of the non-collinear phase-matching in a birefringent crystal is presented. Figure 2.3 presents the schematic diagram representing non-collinear phase-matching for better understanding of the parameters involved in the derivation.

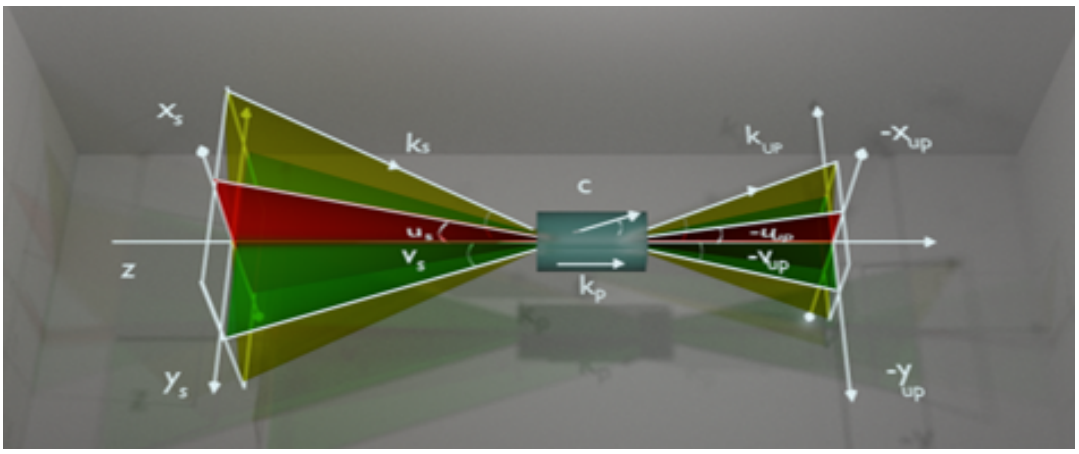

Figure 2.3: *Non-collinear phase-matching depicting input and upconverted angles.*

To calculate the wave-vector mismatch along the direction of k_p (the z-axis) the angle ϕ between the $\vec{k}$ vectors and the z-axis can be found as: $\cos(\phi_i) = \vec{k_i} \cdot \vec{z}$ where $\vec{k_i}$ and $\vec{z}$ are defined as;

$$\vec{k_i} = \left\{ \begin{array}{c} -\tan(u_i) \\ -\tan(v_i) \\ 1 \end{array} \right\} / \sqrt{\tan^2(u_i) + \tan^2(v_i) + 1} \tag{2.6}$$

and

$$\vec{z} = \begin{Bmatrix} 0 \\ 0 \\ 1 \end{Bmatrix} \tag{2.7}$$

Therefore, $\cos(\phi_i)$ can be defined as;

$$\cos(\phi_i) = \frac{1}{\sqrt{\tan^2(u_i) + \tan^2(v_i) + 1}} \tag{2.8}$$

The phase-mismatch Δk along longitudinal and transverse planes, respectively, can be represented as;

$$\Delta k_Z = 2\pi \left(\frac{n_{up}}{\lambda_{up}} \cos(\phi_{up}) - \frac{n_p}{\lambda_p} - \frac{n_s}{\lambda_s} \cos(\phi_s) \right) \tag{2.9}$$

and

$$\Delta k_T = 2\pi \left(\frac{n_{up}}{\lambda_{up}} \sin(\phi_{up}) - \frac{n_s}{\lambda_s} \sin(\phi_s) \right) \tag{2.10}$$

The mismatch Δk along z-axis for two types of phase-matching (i.e. type-I and type-II) can be represented as;

$$\begin{aligned} \Delta k_{ooe} =& 2\pi \left(\frac{n_{e,up}(\theta_{up}, \lambda_{up})}{\lambda_{up}} \frac{1}{\sqrt{\tan^2(u_{up}) + \tan^2(v_{up}) + 1}} - \frac{n_{o,p}(\lambda_p)}{\lambda_p} \right. \\ & \left. - \frac{n_{o,s}(\lambda_s)}{\lambda_s} \frac{1}{\sqrt{\tan^2(u_s) + \tan^2(v_s) + 1}} \right) \end{aligned} \tag{2.11}$$

$$\begin{aligned} \Delta k_{oee} =& 2\pi \left(\frac{n_{e,up}(\theta_{up}, \lambda_{up})}{\lambda_{up}} \frac{1}{\sqrt{\tan^2(u_{up}) + \tan^2(v_{up}) + 1}} - \frac{n_{o,p}(\lambda_p)}{\lambda_p} \right. \\ & \left. - \frac{n_{e,s}(\theta_s \lambda_s)}{\lambda_s} \frac{1}{\sqrt{\tan^2(u_s) + \tan^2(v_s) + 1}} \right) \end{aligned} \tag{2.12}$$

where angle dependent refractive index $n_{e,i}(\theta_i)$ is given by Eq. (2.5). The ordinary refractive index $n_{o,i}$ is in the xy-plane and therefore is independent of angle θ. In order to find the angle θ between the $\vec{k}$-vector and the optical axis of the crystal $\vec{c}$, the dot product of the normalized vectors $\cos(\theta_i) = \vec{k_i} \cdot \vec{c}$ can be calculated; where $\vec{k_i}$ is given by Eq. (2.6) and $\vec{c}$ is defined as;

$$\vec{c} = \left\{ \begin{array}{c} \sin(\theta_{cut}) \\ 0 \\ \cos(\theta_{cut}) \end{array} \right\} \tag{2.13}$$

$$\begin{aligned} \cos(\theta_i) =& \frac{-\tan(u_i)\sin(\theta_{cut}) + \cos(\theta_{cut})}{\sqrt{\tan^2(u_i) + \tan^2(v_i) + 1}} \\ =& \frac{\cos(\theta_{cut} + u_i)\cos(v_i)}{\sqrt{\cos^2(v_i) + \cos^2(u_i)\sin^2(v_i)}} \end{aligned} \tag{2.14}$$

The phase-matching condition for a birefringent nonlinear medium can then be presented as;

$$\Delta k_Z = \cos(\phi_{up})\,\frac{n_{e,up}(\theta_{up}, \lambda_{up})}{\lambda_{up}} - \cos(\phi_s)\,\frac{n_{e,s}(\theta_s, \lambda_s)}{\lambda_s} - \frac{n_{o,p}}{\lambda_p} \tag{2.15}$$

$$\Delta k_T = \sin(\phi_{up})\,\frac{n_{e,up}(\theta_{up}, \lambda_{up})}{\lambda_{up}} - \sin(\phi_s)\,\frac{n_{e,s}(\theta_s, \lambda_s)}{\lambda_s} \tag{2.16}$$

$$\frac{v_{up}}{u_{up}} = \frac{v_s}{u_s} \tag{2.17}$$

To calculate the phase-matched wavelength as a function of incoming angles u and v, Eqs. 2.15, 2.16 and 2.17 are solved simultaneously.

Figure 2.4 represents the phase-matching curve using AGS crystal as a nonlinear medium at different crystal rotation angles as a function of external angle u.

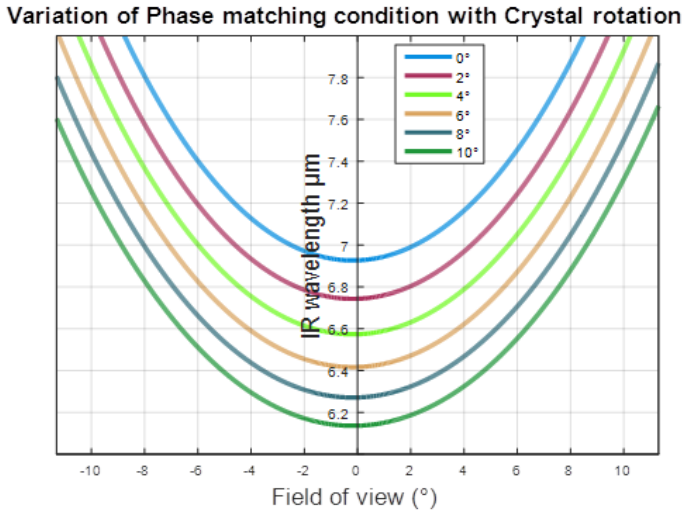

Figure 2.4: *Non-collinear phase-matching using AGS with a cut angles of* 48° *and pump wavelength of 1064 nm. Wavelengths vs. input angles at varying crystal rotation angles.*

Δk_L and Δk_T represent longitudinal and transverse phase-mismatch where ϕ_i is the angle w.r.t. z-axis, and θ_i is the angle with respect to optical axis of the crystal (all the angles are depicted in Fig. 2.3) [48]. As can be seen from Fig. 2.4, by rotating the nonlinear crystal w.r.t. its optical axis, the parabola of phase-matching shifts. This principal is used for the formation of hyperspectral cube [47], which will be explained in section 3.1.

2.1.2 Spectral resolution

When using a broadband light source for upconversion based spectral measurement, spectral resolution is an important parameter. The spectral resolution in upconversion based detection is limited by the length of the nonlinear medium, given a spectral resolution set by the acceptance bandwidth of the nonlinear conversion process. The spectral acceptance bandwidth can be derived from the energy and momentum conservation Eq. (2.2) and (2.3). Taking the derivative of the phase-mismatch with respect to IR wavelength, the value where the conservation efficiency has decreased to half of the peak value can be found. This can be evaluated to give the full-width at half maximum (FWHM) spectral acceptance bandwidth $\Delta\nu_s$ for the mid-IR signal [48].

$$\Delta\nu_s = \frac{0.886}{l}\left[n_e(\theta_s,\lambda_s) - n_e(\theta_{up},\lambda_{up}) - \lambda_s\frac{\partial n_e(\theta_s,\lambda_s)}{\partial\lambda_s} + \lambda_{up}\frac{\partial n_e(\theta_{up},\lambda_{up})}{\partial\lambda_{up}}\right]^{-1} \quad (2.18)$$

Where 'l' is the length of the crystal. Figure 2.5 represent the spectral resolution of the upconversion based detection, when using a broadband IR signal and 10 mm long AGS crystal as a nonlinear medium. The colored lines represent different crystal rotations (wavelength ranges); the solid and dashed lines represent the u and v directions, respectively [48].

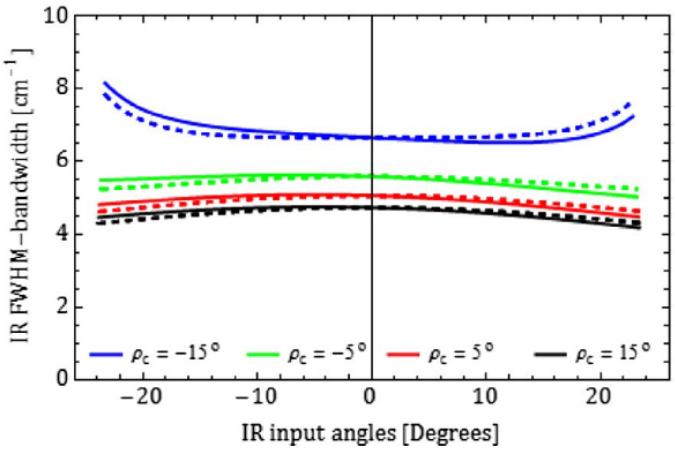

Figure 2.5: *Numerical calculation of the FWHM acceptance bandwidth for the IR signal in a 10 mm long AGS crystal. The colored lines represent different crystal rotations (wavelength ranges); the solid and dashed lines represent the u and v directions, respectively (The figure is taken from Ref. [48]).*

For large non-collinear angles, the spectral resolution is limited by the interaction length and the pump beam diameter, rather than the length of the crystal. Hence spectral resolution deteriorates for increasing non-collinear angles [49] as shown in Fig. 2.5. Hence, the spectral resolution in upconversion based images is not constant, when using broadband illumination. However, in the case of narrowband illumination sources, the spectral resolution is set by the illumination source itself and is constant throughout an image.

2.1.3 Quantum efficiency

The quantum efficiency of CW upconversion and collinearly phase-matched systems is generally calculated for plane wave, non-depleted systems as [46]:

$$QE_{cw} = \frac{16\pi d_{eff}^2 l^2 P_p}{n_s n_p n_{up} c\epsilon_0 \lambda_s \lambda_{up} \omega_p^2} \tag{2.19}$$

where P_p is the pump field power, l is the length of the nonlinear crystal, d_{eff} is the effective nonlinearity of the material. ω_p is the pump beam radius, ϵ_0 is the vacuum permittivity, $c$is the speed of light, n_s, n_p and n_{up} are the refractive indices of the signal, pump and upconverted signal respectively. λ_s and λ_{up} are signal and pump wavelengths respectively.

2.1.4 Imaging setup

Figure 2.6 shows the schematic of an upconversion based imaging setup. A United State Air-Force (USAF) resolution target is used as an object illuminated by mid-IR light (narrowband for simplicity) which, after passing through the target, is focused into the nonlinear crystal using f_1. f_2 forms the back focal plane of the 4f setup. A beam combiner is used to combine the mid-IR signal and the mixing field in the nonlinear crystal. Filters are used to block the residual pump and stray light from reaching the camera. A silicon based camera is used for image acquisition.

It can be seen from Fig. 2.6 that the nonlinear crystal lies in Fourier plane i.e. upconversion takes place in the Fourier plane hence the size of the mixing beam acts as a soft aperture limiting the spatial resolution that can be achieved with the system.

Due to the angular dependence of the phase-matching condition, the upconverted image exhibits a ring-like pattern. The intensity in the ring pattern is governed by a sinc function [46];

$$I_{up} = \mathrm{sinc}^2\left(\frac{\Delta k_z l}{2}\right) \tag{2.20}$$

Figure 2.7 is a schematic representation of the upconversion based images when using broadband and narrowband illumination sources.

Figure 2.8(a) shows a simulated upconverted image at a single crystal rotation setting and Fig. 2.8 (b) shows the line-scan along the white line in Fig. 2.8(a) which reveals sinc^2-like

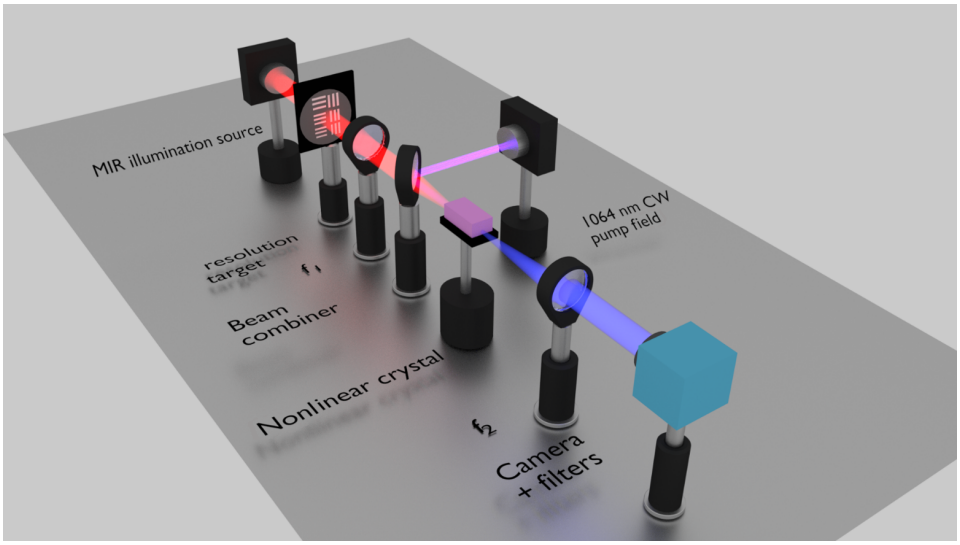

Figure 2.6: *Schematic for 4f-Imaging setup for upconversion based imaging. A USAF resolution target is used as a target illuminated by mid-IR light, f_1 and f_2 form the front and back focal plane of the 4f setup, respectively. A Silicon-based camera is used for image acquisition.*

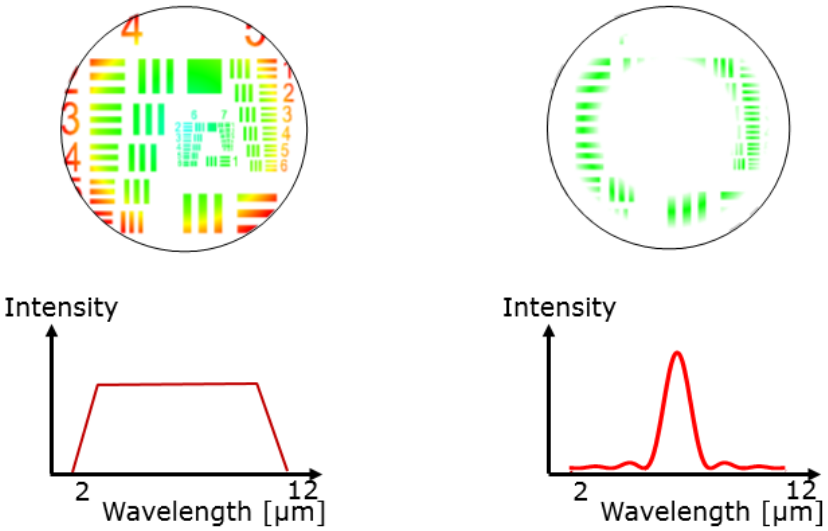

Figure 2.7: *Schematic representation of the narrowband and broadband upconversion images.*

intensity distribution. Scanning the crystal rotation angle, alters the phase-matched angles, thereby, producing rings of varying diameter as shown in Visualization-1. Figure 2.9 represents the snapshots from the Visualization-1.

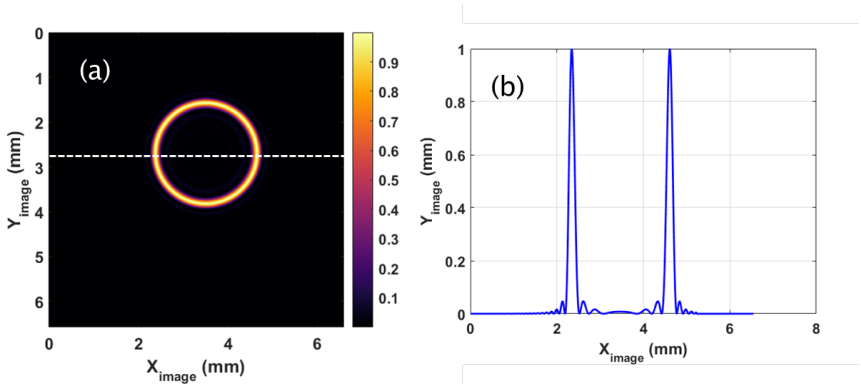

Figure 2.8: *Upconverted image intensity distribution for the case of a narrowband illumination source*

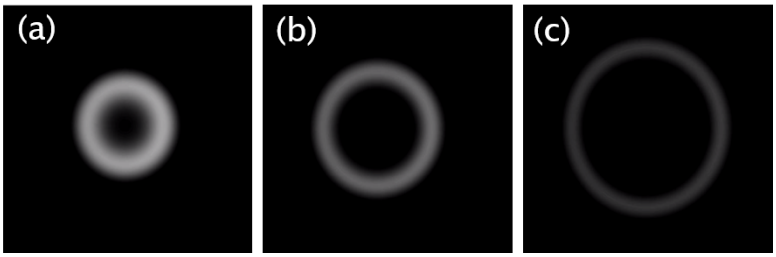

Figure 2.9: *Upconverted image intensity distribution for the case of a narrowband illumination source with Gaussian-intensity profile and varying crystal rotation angles. These images are corresponding frames of the Visualization-1.*

By careful control of the crystal rotation angles and the spectral tuning of the illumination source, a series of narrowband images, i.e. a hyperspectral cube can be produced which is explained in section 3.1.

Figure 2.10 is the schematic representation of the upconverted image formation, where a Gaussian illuminated resolution target is used as an object multiplied with sinc^2-like intensity distribution for phase-matching angle selection and convolved with the pump beam diameter. This is a generic explanation of the upconversion based image formation considering narrowband illumination. The case using broadband illumination is presented in Chapter 3. The narrowband upconverted field can be constructed using a three-step procedure explained below under the assumption of non-depleted interaction [46, 49] and the thin filter approximation [50], equivalent to neglecting diffraction of the two interacting fields inside the nonlinear crystal. The latter assumption allows us to single out the longitudinal component of the phase-mismatch factor.

- First step is a simple de-magnification of the object field: The factor reflects lenses in

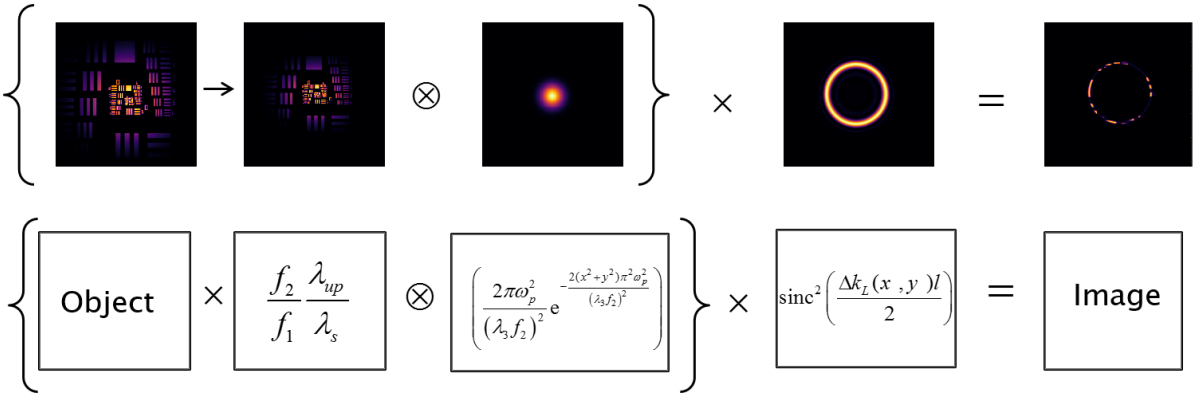

Figure 2.10: *From left to right: The Formation of an upconverted image, involving demagnification due to wavelength conversion (given by transverse phase-mismatch) and a lens system, the* sinc^2*-like intensity distribution and a the blurring effect due to a finite pump beam size.*

the 4f imaging system and the transverse conservation of momentum in the upconversion process [22].

- Secondly, the finite pump beam introduces a blurring in the image, this is taken into account by convolving (acting on the transverse coordinates) the resulting image (field) with a point spread function calculated from the Gaussian pump laser profile inside the nonlinear crystal. Blurring of the upconverted image is similar to that of a thin Gaussian transmission filter, or conceptually as found in a pin-hole camera. However, the Gaussian filter is induced by the nonlinear mixing with the Gaussian pump beam [51].

- The final step is to calculate the sinc-like phase-mismatch factor, along the z-axis, transformed to the image plane. The resulting efficiency scaling factor can be conveniently treated as a multiplicative factor applied point-by-point on the image [47].

The spatial resolution is derived conveniently from the properties of the point spread function above assuming a delta function as object. In order to mimic the traditional Rayleigh criteria with the present Gaussian soft aperture we deploy the $e^{-1} = 36.7\%$ intensity levels of the Gaussian intensity distribution [52]. The resolution R can then be calculated as:

$$R = \frac{f_1}{f_2}\frac{\lambda_s}{\lambda_{up}} \times \frac{2f_2\lambda_{up}}{\pi D_p}\sqrt{2} = \frac{2f_1\lambda_s}{\pi D_p}\sqrt{2} \tag{2.21}$$

The estimated number of pixels in the upconverted image N is;

$$N = \frac{\pi D_s^2}{4R^2} = \frac{\pi^3 D_s^2 D_p^2}{32 f_1^2 \lambda_s^2} \tag{2.22}$$

where D_p is pump beam diameter $(1/e^2)$ and D_s is the IR illumination beam diameter $(1/e^2)$.

2.1.5 Tangential phase-matching

The detailed phase-matching properties of the setup are described in the following. As can be seen in Fig. 2.11(a), the pump and signal beams are aligned at a specific angle ϕ_s with respect to each other. This is explained in Fig. 2.11(b), where the top point of the red circle is seen to be tangential to the blue ellipsoid.

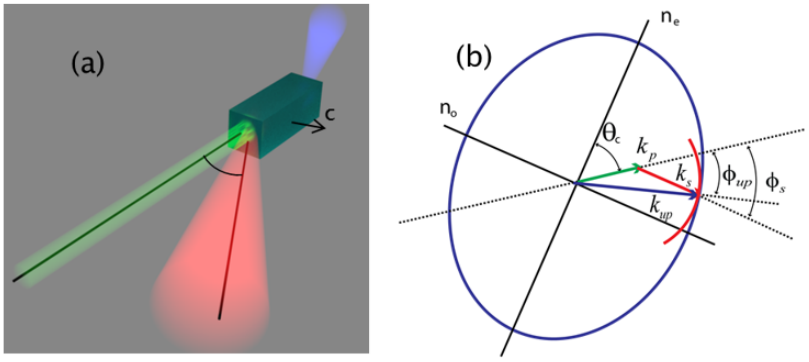

Figure 2.11: *(a)Detailed setup for tangential phase-matching. (b) Diagram in k-space of a type-I upconversion of a signal k_s with a pump k_p producing an upconverted beam k_{up}.*

Using this angle between the signal and pump beam results in concentric ring patterns in the upconverted images when the crystal is rotated.

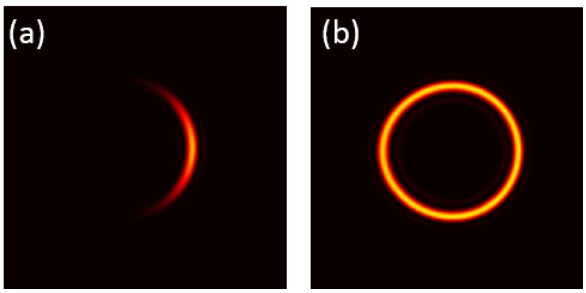

Figure 2.12: *Simulated images for type-I phase-matching using bulk lithium Niobate as a nonlinear medium (a) Collinear phase-matching (b) tangential phase-matching*

.

If the beams are arranged collinearly, only a fraction of the ring is achieved [18, 53, 54]. However, tangential phase-matching offers lower conversion efficiency due to the smaller interaction length than that of collinear phase-matching. This behavior has particularly been observed in case of bulk lithium niobate. The difference between collinear phase-matching and tangential phase-matching can be seen in Fig. 2.12. The figure represents simulated images for type-I phase-matching using bulk Lithium Niobate as a nonlinear medium. Figure 2.12(a) is simulated when the angle between the pump and the signal is chosen to be 0° i.e. collinear phase-matching while Fig. 2.12(b) represents the case when a angle of $\phi_s = 2.7°$ between the pump and signal is used.

2.1.6 Image distortion from crystal rotation

The angular phase-matching acceptance parameters depend on the configuration of the system. As seen from Fig. 2.11, tangential phase-matching is used, meaning that an angle between the pump and signal beam of $\phi_s = 2.7°$ has been chosen.

Figure 2.13 shows the contour lines in crystal rotation steps of 0.1 degree, for (a) collinear and (b) tangential phase-matching, respectively.

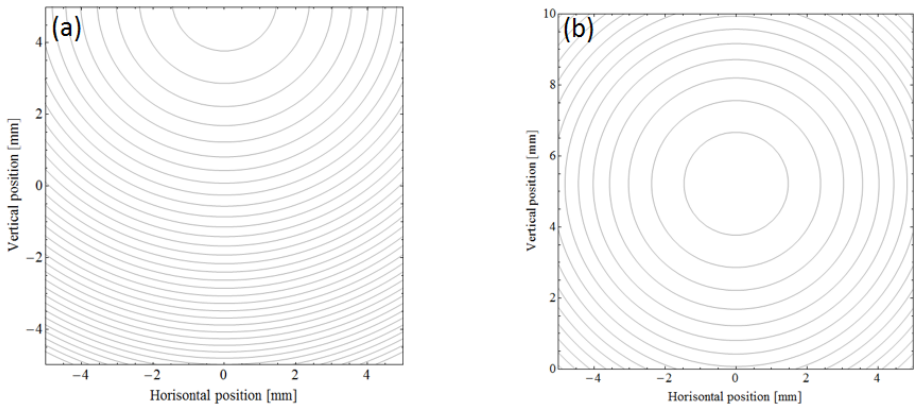

Figure 2.13: *Collinear and (b) tangential phase-matching for crystal rotations in steps of 0.1 degree.*

It is clearly seen from Fig. 2.13 that the crystal rotations angle necessary to covert the 10-mm-aperture field of view is approx. three times larger, starting from collinear interaction, compared to tangential interaction.

Next, the covered image range is plotted as a function of crystal rotation in Fig. 2.14. The red graph shows the angles for optimal phase-matching ($\Delta k = 0$, corresponding

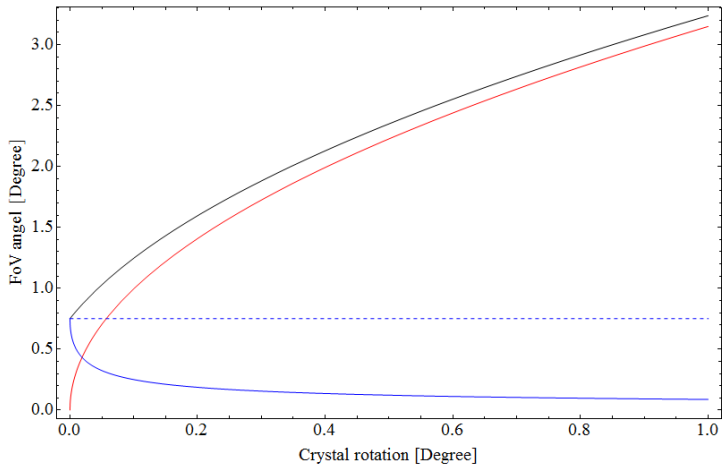

Figure 2.14: *Calculated phase-match ranges as a function of crystal rotation for tangential phase-matching.*

to the position of the contour lines of Fig. 2.13(b)) relative to the image center for tangential phase-matching, while the blue graph shows the acceptance angle (upconverted ring width) for a given crystal rotation. Finally, the black curve shows the field of view as a function of crystal rotation. Rotating the crystal results in a slight change in the refraction angles of the beams going into and out of the nonlinear material in the direction of the rotation, i.e. in the vertical direction in the present case, whereas there is no distortion in the horizontal plane. The resulting distortion in the vertical direction is a difference in the de-magnification of the image depending on the position in the image, the spatially-dependent vertical magnification in the object plane is shown in Fig. 2.15, where (a) shows the collinear case, and (b) shows the case for tangential phase-matching.

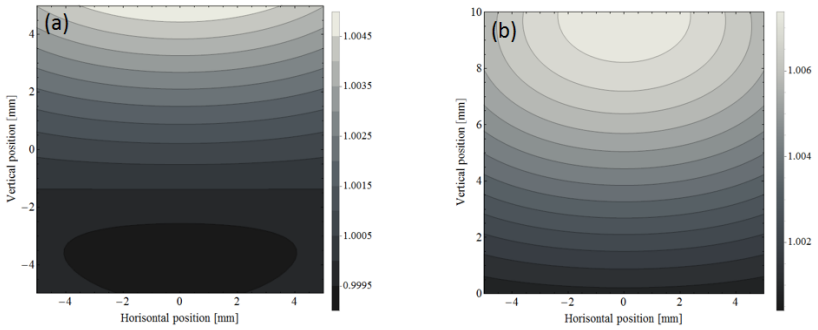

Figure 2.15: *Calculated spatial image magnification variations for (a) collinear and (b) tangential phase-matching.*

In both cases, the distortion is seen to be less than 0.5%, i.e. less than one pixel relative to the center of the image.

2.1.7 Point spread function engineering in upconversion imaging

When using a spatially coherent illumination source, the PSF in the upconversion process can be engineered for spatial filtering, such as phase contrast imaging or dark field imaging of phase or amplitude objects.
Typically, amplitude obstruction filters or spiral phase filters are exploited for edge detection of phase or amplitude objects in linear imaging. These kinds of filtering effects can also be produced in upconversion imaging by modifying the pump beam profile. Spiral phase filters are preferred over amplitude obstruction filters due to better contrast in the filtered images (discussed in more detail in Chapter 6). Figure 2.16 shows a schematic representation of a spiral phase plate.

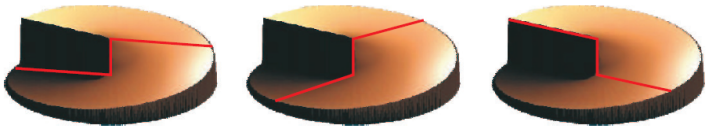

Figure 2.16: *Schematic representation of a typical spiral phase filter. Note that the opposite points are out of phase by π (The Figure is taken from the book [55]).*

Figure 2.17 is the schematic representation of the convolution of the spiral phase with the phase object. It can be observed that the signal is canceled in all the unstructured region of the object due to destructive interference except the edges of the phase jumps.

In this section, the theory of the PSF engineering in upconversion imaging and the numerical model of the phase contrast and edge enhanced imaging are presented. Figure 2.18 is the schematic representation of the setup used for the edge detection in upconversion imaging consisting of a 4f imaging setup where the center of the nonlinear crystal lies in the Fourier plane. Since the pump beam profile effectively acts as a soft aperture in the Fourier plane, its amplitude and/or phase components can be manipulated and used for spatial filtering of the object field through the upconversion process [23].

Figure 2.19 depicts simulated phase pattern of the spiral phase beam with topological charge $m = 1$ and $m = 2$. It can be seen that the phase varies from 0 to 2π for $m = 1$ and 0 to 4π for $m = 2$. The illumination beam incident on the object is assumed to be spatially coherent (but can either be spectrally narrowband or broadband) and collimated

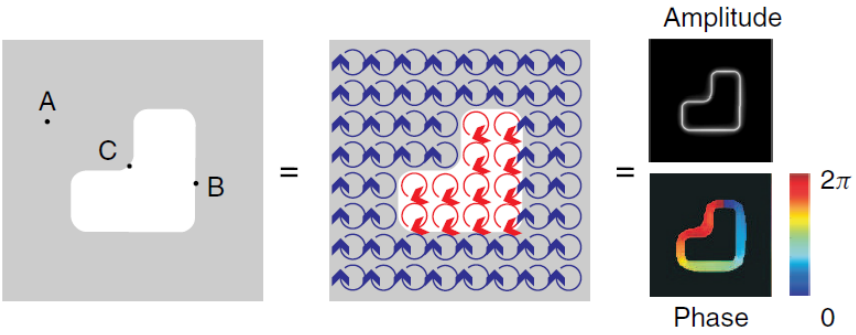

Figure 2.17: *Graphical representation of the convolution of an object with a spiral phase filter: When the integration is carried out, the helical phase profile of the PSF of the spiral phase filter in unstructured regions leads to perfect cancellation of the signal by destructive interference, except at edges where either the phase or the amplitude of neighboring points differ (The Figure is taken from the book [55]).*

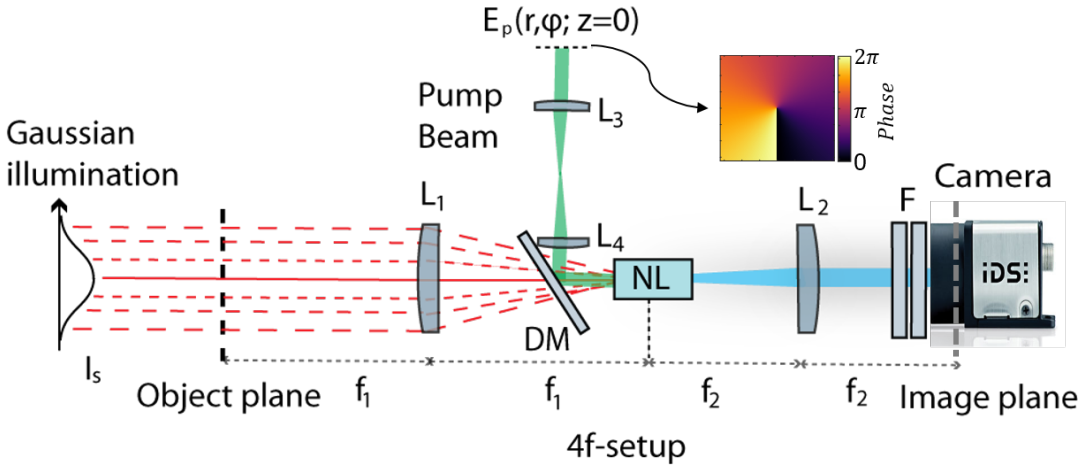

Figure 2.18: *Upconversion phase contrast/dark field imaging system consisting of lenses L_1 and L_2, an IR signal/illumination beam that reads out a phase object, a pump beam carrying a helical phase profile ϕ, a dichroic mirror (DM), a nonlinear (NL) crystal centered at the common Fourier plane of L_1 and L_2, filters (F) and a camera for detecting the upconverted image. Rays of different line styles represent the collinear (red solid line) and non-collinear (red dashed lines) signal angles that can be upconverted with an efficiency determined by the phase-matching condition.*

with a normalized Gaussian intensity profile given by:

$$I_s(x,y) = \exp\left[-2\left(x^2+y^2\right)/\omega_s^2\right] \tag{2.23}$$

where ω_s is the IR beam waist radius in the object plane, i.e., xy-plane. The amplitude transmittance $t_{obj}(x,y)$ in the xy-plane for the case of a phase object can be expressed

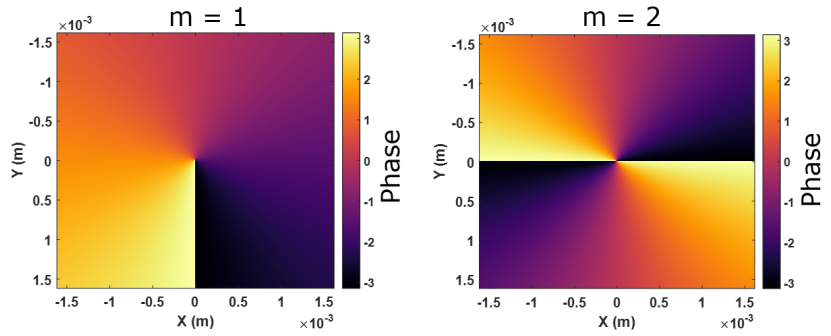

Figure 2.19: *Spiral Phase with topological charge $m = 1$ and $m = 2$.*

as:

$$t_{obj}(x, y) = \exp[i\phi(x, y)] \tag{2.24}$$

where $\phi(x, y)$ is the phase distribution with discrete levels. In this work, we focus on phase objects but it is worth noting that upconversion imaging using spiral phase filter can also be applied to edge detection in amplitude-only objects [23, 24]. A Gaussian beam illuminated spiral phase filter is simulated first with topological charge $m = 1$, then with $m = 2$ and is used as the pump beam (with wavelength λ_p) for the upconversion process. At an initial plane $z = 0$, the normalized electric field of the pump beam with helical phase profile is given by [56]:

$$E_p(r, \phi; z = 0) = \exp\left(-r^2/\omega_p^2 + im\phi\right) \tag{2.25}$$

where ω_p is the pump beam waist radius. Coordinates r and ϕ are the radial distance and azimuth angle, respectively, defined in the initial plane. As mentioned earlier, the pump beam profile can be imaged/projected (using another 4f setup with lenses L_3 and L_4) into the transverse mid-plane of the nonlinear crystal to function as a spatial filter in Fourier plane of the upconversion imaging system. The destructive interference arising in the center of the Gaussian beam illuminated spiral phase filter prevents the low spatial frequency components of the incoming object field to partake in the upconversion process - resulting in edge-enhanced upconverted images. When using topological charge $m = 1$, a typical spiral phase contrast (SPC) imaging can be performed, when changing to $m = 2$, the SPC can only be performed for curved contours in the object [55]. Due to the lack of availability of a $m = 1$ spiral phase plate, we have utilized $m = 2$ spiral phase in experiments in combination with a pin-hole for blurring effect (see Chapter 6). This leads to edge detection based on dark field imaging and not spiral phase filter. The PSF in this case, that describes the image edge-enhancement can be defined as:

$$PSF(f_u, f_v) = \mathrm{circ}(f_r/\Delta f_r)\, \mathcal{F}\{E_p(r, \phi; z = 0)\} \tag{2.26}$$

where $f_r = \sqrt{f_u^2 + f_v^2}$, f_u, and f_v, are the spatial frequency along the horizontal, vertical and radial axis, respectively, in the Fourier plane of the 4f setup used to image $E_p(r, \phi; z = 0)$ in the midplane of the nonlinear crystal, $\mathrm{circ}(f_r/\Delta f_r)$ represents a pin-hole which lies in the said Fourier plane. Varying the circ function radius Δf_r (which scales inversely with the pin-hole radius) adjusts the size of the dark core of the pump for efficient removal of the contribution of low spatial frequency components of the object field in the upconverted image.

When using $m = 1$, there is no need for the pin-hole for blurring effect and Eq. (2.26) can be reduced to;

$$PSF(f_u, f_v) = \mathcal{F}\{E_p(r, \phi; z = 0)\} \tag{2.27}$$

Equation (2.28) describes the intensity of the upconverted image where $\mathrm{sinc}^2[\Delta k(\lambda_{IR}, \theta)\, l/2]$ is a normalized profile describing the efficiency of the upconversion process which is dependent on the longitudinal phase-mismatch Δk (which is a function of the signal's wavelength λ_{IR} and incident angle θ) and length l of the nonlinear crystal [46]. Integrating the $sinc^2$ function over the spectral range of the illumination source, i.e., from λ_1 to λ_2 gives the upconverted intensity [57].

$$I_{up} \propto I_s(\bar{x}, \bar{y}) |t_{obj}(\bar{x}, \bar{y}) \otimes PSF(\bar{x}, \bar{y})|^2 \int d\lambda_s \Gamma(\lambda_s)\, \mathrm{sinc}^2 \left[\frac{\Delta k(\lambda_s, \theta) l}{2}\right] \tag{2.28}$$

Here $\otimes$ denotes the two-dimensional convolution, Γ is the spectral intensity of the IR illumination ($\Gamma = 1$ is assumed for both our narrowband and broadband case).

Equation (2.29) is the scaling relation used to convert $PSF(f_u, f_v)$ to $PSF(\bar{x}, \bar{y})$ and Eq. (2.30) to convert $I_s(x, y)$ and $t_{obj}(x, y)$ to $I_s(\bar{x}, \bar{y})$ and $t_{obj}(\bar{x}, \bar{y})$, respectively. The upconverted wavelength can be calculated using the usual energy conservation i.e., $\lambda_{up} = (\lambda_s^{-1} + \lambda_p^{-1})^{-1}$.

$$(\bar{x}, \bar{y}) = \lambda_{up} f_2(f_u, f_v) \tag{2.29}$$

$$(\bar{x}, \bar{y}) = \frac{\lambda_{up}}{\lambda_s} \frac{f_2}{f_1}(x, y). \tag{2.30}$$

When calculating the intensity of the upconverted image given by Eq. (2.28), an FFT-based numerical simulation is implemented using Matlab. For monochromatic IR illumination, only a single signal wavelength λ_s is used (i.e., the integration is dropped).

In Eq. (2.28), the terms $I_s(\bar{x},\bar{y})$,$t_{obj}(\bar{x},\bar{y})$, and $PSF(\bar{x},\bar{y})$ have been taken outside of the integration even though the scaling relations show that they depend on λ_s. However, for the case of polychromatic/broadband IR illumination used in this study (with spectral bandwidth of only 6.4 nm), we find that the change in λ_{up} and the change in λ_{up}/λ_s ratio from $\lambda_s = \lambda_1$ to $\lambda_s = \lambda_2$ is neglible ($< 1\%$).

3 Upconversion hyperspectral imaging in 5 to 10 µm spectral regime

3.1 Broadband illumination: Globar

This work demonstrates, to the best of our knowledge, the first application of upconversion technology for hyperspectral imaging in the 5 to 10 µm range. The setup consists of an upconversion unit based on AGS as the nonlinear material and a 1064 nm pump laser. A globar i.e. a broadband source is used for illumination. A novel technique for hyperspectral imaging exploiting birefringent non-collinear phase-matching in the nonlinear crystal is implemented together with post-processing of the acquired images. Scanning of the phase-match condition is implemented by rotation of the nonlinear crystal relative to its $\vec{c}$-axis, which enables imaging of every pixel within the field of view (FoV) with full spectral information encoded.

This approach is only viable for imaging when performing the frequency conversion in the Fourier plane of the system (a translation in the Fourier plane coursed by crystal rotation only results in an angle in the image plane, i.e. no change in the position on the camera). Scanning of the phase-match condition for hyperspectral imaging has previously been demonstrated in the 3 µm spectral range by temperature tuning of a PPLN crystal [19], however, leading to a very low image acquisition rate due to a slow thermal tuning rate, as well as power instabilities due to the intracavity nature of that system.

In this study, a broadband, mid-IR hyperspectral imaging system is demonstrated based on nonlinear frequency upconversion. An AGS crystal $5 \times 5 \times 10$ mm^3, cut at 48° is used as the nonlinear medium for SFG of the mid-IR signal and the pump field. A globar is used as mid-IR illumination sources whereas a diode pumped solid-state (DPSS) laser, i.e., Nd:YVO_4 continuous wave (CW) 1064 nm laser delivering up to 1.7 W of power in a fundamental Gaussian mode is used as the pump field.

The upconversion module is presented in Fig. 3.1. Mirrors M1 and M2 form the laser cavity, whereas mirrors M3, M4, M5 and a beam combiner are used to guide the pump

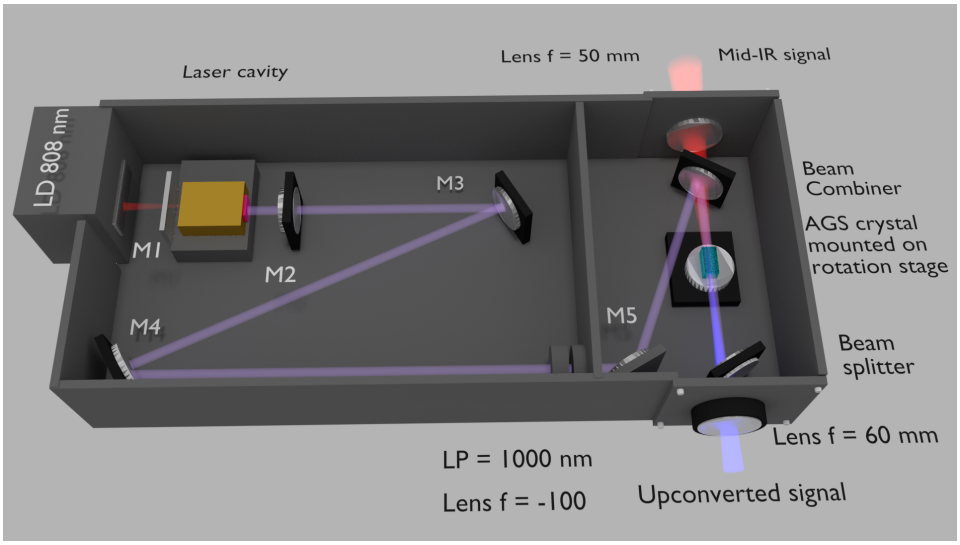

Figure 3.1: *Upconversion unit containing AGS crystal for sum frequency generation. M1 is a concave mirror with curvature R=200 mm with high reflection at 1064 nm and high transmission at 808 nm. M2 is a plane mirror with 90% reflection at 1064 nm, and 10% out-coupling. M3 is a plane mirror and M4 is a concave mirror with curvature R=200 mm to guide light to the nonlinear crystal. Lens with f=-100 mm is used to collimate the converging light.*

laser beam through the nonlinear crystal. A lens with f=-100 mm is used to collimate the converging light and to achieve pump beam diameter of 1 mm in the nonlinear crystal. A beam combiner is used to combine the mid-IR and pump field in the nonlinear crystal.

Non-collinear birefringent phase-matching is exploited; by rotation of the nonlinear crystal the phase-match condition is scanned enabling broad spectral coverage over the full FoV. The theory of non-collinear birefringent phase-matching is described in Chapter 2.

Figure 3.2 shows the imaging system including an illumination source and the upconversion detection system. A USAF resolution target is illuminated by the mid-IR light source which is then magnified using a pair of lenses (f_1 and f_2) by the factor of f_2/f_1. The beam is focused into the nonlinear crystal using lens f_3 for non-collinear phase-matching in the Fourier plane mixing with the 1064 nm pump field with a beam diameter of 1 mm ($1/e^2$ diameter of the Gaussian beam). f_4 forms together with f_3 a 4f-imaging system between the magnified object plane and image plane, where an IDS 1.31 Mpixel CCD camera is used for upconverted image acquisition. A pair of filters and a mirror is used to block stray light and residual pump signal. In this section the images acquired with the globar illumination i.e. a broadband source, is presented. A USAF resolution target (clear optical path, Edmund optics) is used as a test sample carrying well-defined

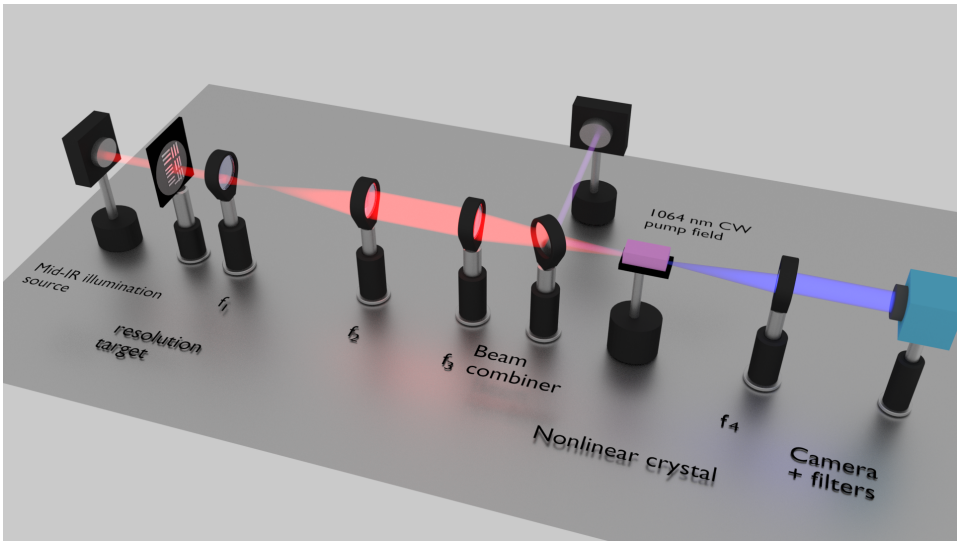

Figure 3.2: *Single-pass upconversion system using globar as illumination sources and a 1064 nm laser pump field for sum frequency generation. Zinc Selenide ($ZnSe_2$) lenses are used for the mid-IR signal, where f_1 and f_2 can be applied for object magnification, f_3 (= 50 mm) is used to focus the object light into the nonlinear crystal for non-collinear upconversion and provides with f_4 (= 60 mm) a 4f-imaging system with the nonlinear conversion occurring in the Fourier plane. Filters (short pass 1000, long pass 900) and a beam splitter is used to eliminate the residual pump and stray light from the upconverted signal. An IDS Silicon camera is used for the image acquisition. A clear optical path USAF resolution target and/or polystyrene film (not shown) is used as an object.*

spatial features to assess the spatial resolution of the imaging system. Furthermore, a polystyrene film (PS) is used, either alone or in combination with the resolution target to impose spectral features to the signal field. The scaling optics is used to resolve smaller spatial features of the sample, however, at the expense of a reduced FoV.

Figure 3.3 shows upconverted images acquired with the Si CCD camera for a crystal rotation of 3°, increasing crystal rotation means decreasing collinear angle relative to the crystal $\vec{c}$-axis (see Fig. 2.4). Figure 3.3(a) shows an upconverted image of the illumination source alone (without any target), demonstrating the FoV of the imaging system as well as the spatial and spectral homogeneity of the illumination source. In Fig. 3.3(b) a PS film is introduced in the object plane, where the dark ring corresponds to the PS absorption line at 6.7 μm (as can be seen in the phase-matching curve in Fig. 2.4). Figure 3.3(c) depicts an acquired image combining resolution target and PS film, note the different scale bar, the FoV is limited by the resolution target. The smallest resolvable element in this image is group 0 element 6 corresponding to approx. 280 µm. Finally, Fig. 3.3(d) shows the upconverted image of the resolution target with a magnification

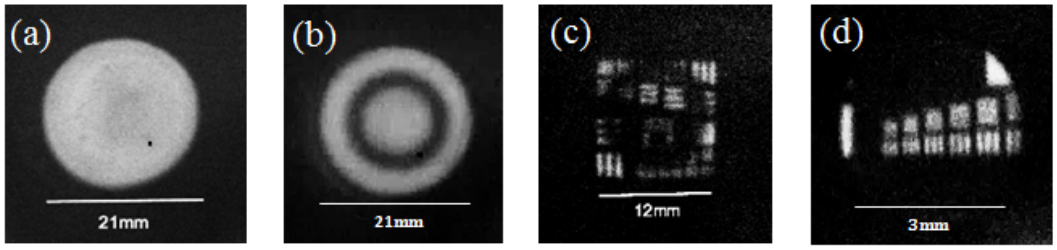

Figure 3.3: *Upconverted images at 3° crystal rotation (with respect to $\vec{c}$-axis) using 500 ms camera integration time (the scale bar refers to the object plane (a) Upconverted image without any sample with full FoV, (b) with PS film showing the absorption line at 6.7 µm (Visualization-2) (c) Upconverted images of USAF resolution target and PS film (Visualization-3), (d) magnification of 6.667 (100/15) is applied to resolve the smallest features of the resolution target i.e. 35 µm.*

(before the upconversion) of 6.667 ($f_2/f_1 = 100/15$) resolving the smallest features of the target (Group 3 element 6) i.e. 35 µm.

The radial wavelength dependence in the upconverted image is dictated by the non-collinear phase-match condition of the upconversion process in the Fourier space [22, 49, 58]. A series of images is captured while rotating the nonlinear crystal where the spectral features of PS can be observed in the 6 to 8 µm range (Visualization-2, corresponding Fig. 3.3(b)). A second series of images is taken while rotating the crystal including both PS film and resolution target (Visualization-3, corresponding Fig. 3.3(c)). The number of spatially resolvable elements is estimated as the ratio of total area (FoV) over the smallest resolvable element, in the object plane (Eq. (2.22)). Approx. 4400 is achieved in this study independent of the scaling optics. The signal to background ratio of the image acquisition can be estimated by the ratio of the camera integration time for the upconverted images relative to the integration time for equivalent intensity of the background i.e. 0.3 s/2 s, (here 0.3 s is used for signal instead of 0.5 s used in Fig. 3.1, because the maximum integration time of the camera is 2 s which was not sufficient for similar intensity of the background compared to signal intensity therefore integration time of 0.3 s is used for signal).

In the following the post-processing of the acquired upconverted images in order to extract monochromatic (here monochromatic refers to narrowband) images is explained. In this approach, the acquired images are simply convolved with a response function for the specific wavelength (and crystal orientation) and summed. To construct monochromatic images, the spatial information, at the wavelength of interest, is extracted from each upconverted image for all crystal rotation angles calculated from the phase-match condition. This is obtained from pixel wise multiplication of the acquired upconverted images and a numerically calculated spectral image response function for the specific

rotation angle of the nonlinear crystal at the wavelength of interest. These predominantly circular monochromatic intensity distributions (corresponding to the different crystal rotation angles) are then summed to form monochromatic images with full FoV. An automated MatLab program is developed for the post-processing of series of upconverted images, captured as a function of the rotation angle of the nonlinear crystal.

The monochromatic image acquisition algorithm can be represented as

$$I_{mono}(\theta_i) = I_{up}(\theta_i) \times I_{\lambda}(\theta_i) \tag{3.1}$$

$$I_{\lambda}(\theta_i) = \left\{ \begin{array}{c} \text{Numerical single-wavelength image response} \\ \text{function at crystal rotation angle } \theta_i \end{array} \right\} \tag{3.2}$$

$$I_{up}(\theta_i) = \left\{ \begin{array}{c} \text{Upconversion image intensity at} \\ \text{crystal rotation angle } \theta_i \end{array} \right\} \tag{3.3}$$

where $\times$ symbolizes a pixel-by-pixel multiplication of the upconverted intensity $I_{up}(\theta_i)$ and the normalized phase-matched wavelength response in the image $I_{\lambda}(\theta_i)$, giving the monochromatic image at wavelength λ at crystal rotation angle θ_i. This step represents the extraction of single-wavelengths from the polychromatic upconverted images. This procedure is repeated for all crystal rotation angles and the full monochromatic image is obtained as the sum of these individual contributions

$$I_{mono} = \sum_{i=0}^{n} I_{mono}(\theta_i) \tag{3.4}$$

I_{mono} represents the monochromatic image at full FoV, when the crystal is rotated in n steps, from 0 to θ_{max} degree. This procedure is repeated for the full spectral range of interest resulting in series of monochromatic images forming the hyperspectral image cube. To obtain high quality monochromatic images in terms of spatial and spectral information, the angular step size of the crystal rotation angle should be kept small enough to reduce the intensity variations within the reconstructed images. This is illustrated in Fig. 3.4, however, normalization of the summed images can be done to allow for lower sampling of the crystal rotation angle. The spectral resolution is limited by the crystal length and pump beam beam size in the crystal (As described in section 2.1.2). Figure 3.4 illustrates simulated sinc-funtion intensity distributions as a function of non-collinear mixing angles at 6.9 µm while the crystal is rotated from 0° to 10° in steps of 0.5°. The dashed line shows the homogeneous intensity profile obtained by summing the narrowband sinc^2-functions, this can potentially be used for normalization of the monochromatic images.

Figure 3.5 shows two monochromatic images acquired by post-processing of a series of upconverted images of a broadband illuminated USAF resolution target including the PS film as shown in Fig. 3.3(c). The series of images is acquired while rotating the

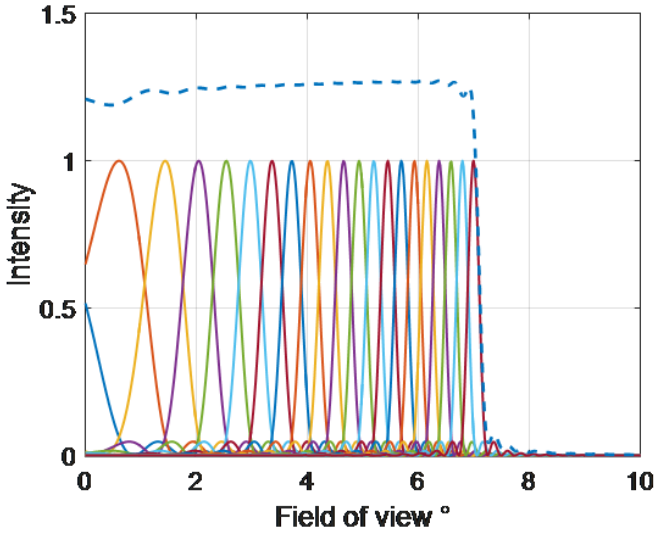

Figure 3.4: *Simulated Sinc-function intensity distribution at 6.9 µm while rotating the crystal from* 0° *to* 10° *in steps of* 0.5°. *Dashed line shows the summation of all the intensity distribution within the full FoV*

crystal from 0° to 20° in steps of 0.5°. Figures 3.5(a) and 3.5(b) show reconstructed monochromatic images of the target at 6.5 µm and 6.7 µm, respectively. Comparing the two images the absorption line of PS at 6.7 µm can be noticed from the decreased intensity contrast. A series of monochromatic images is computed in the 6 to 7 µm spectral range where the PS spectral absorption features are evident, this can be seen as intensity variations in the monochromatic images (Visualization-4). In Visualization 4 (the corresponding snapshots in Fig. 3.5), size scaling of the monochromatic images can be observed depending on the wavelength, by the scaling factor related to transverse phase-matching equation [48].

The spectral bandwidth of the upconversion process is dependent on the crystal length, the pump beam diameter and consequently on the incoming mid-IR angle (as described in section 2.1.2), which is conserved in the post-processing step, hence, the spectral bandwidth in the monochromatic image increase slightly radially in the image. Thus, the spectral resolution deteriorates with increasing mid-IR angles as depicted in Ref. [48] Fig. 3.6.

Figure 3.6(a) shows the measured spectrum of PS film based on FTIR and upconversion. The spectrum measured with FTIR is recorded at 8 cm^{-1} spectral resolution. The FTIR spectrum has better spectral resolution but it can be improved for upconversion based spectrum using longer crystal length. In Fig. 3.6(b) two curves are plotted using upconversion, one based on the central pixel of the images (upc-center) and the other

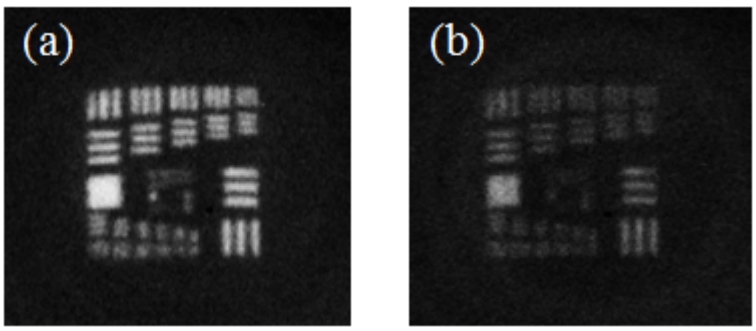

Figure 3.5: *Monochromatic images of USAF resolution target combined with PS film containing both spatial and spectral features acquired by upconversion and post-processing of broadband illuminated target. (a) at 6.5 µm and (b) 6.7 µm wavelength.*

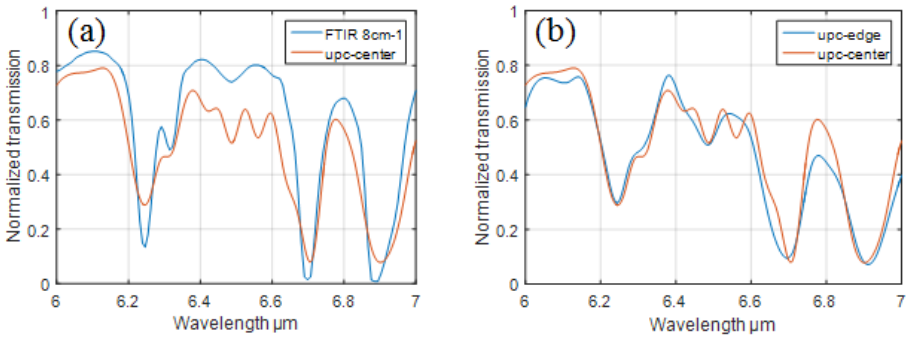

Figure 3.6: *Measured transmission spectra of polystyrene (a) comparing the FTIR measurement with the upconversion (b) comparison of the spectral resolution depending on the position of the images based on upconversion. It can be noticed that the spectral resolution deteriorates along radial direction*

is taken when pixels on the edge of the FoV is considered (upc-edge). It is noted that the spectral resolution for upc-edge is worse than that of upc-center as seen from Fig. 3.6(b).

3.2 Narrowband illumination: QCL

In this section, upconversion based spectral images are presented using a narrow band tunable QCL as the illumination source. The QCL used in this experiment is operated in an external cavity configuration with a tunable diffraction grating enabling selection of the desired wavelength. A Littrow configuration with back facet out-coupling is used

to achieve higher average power, while scarifying some tunability range. The working principle consists of electrical pumping of the QCL crystal and letting the amplified light through an antireflection (AR) coated intra-cavity facet onto the diffraction grating. Only the minus first diffraction order of the desired wavelength will retro-reflect back from the diffraction grating into the QCL crystal and get further amplified. Tunability of the laser is limited by the gain spectrum of the active region, quality of the AR coating on the intra-cavity facet and the diffraction grating efficiency. The utilized tuning range in this set of experiments is from 5.9 to 6.19 µm with a measured linewidth below 4 nm. Average power (at 6 µm) is 4.5 mW, with a pulse repetition rate of 0.5 MHz and a pulse durations of 50 ns, leading to duty cycle of 2.5%. Figure 3.7 shows the output spectra of the QCL used in the experiment. A USAF resolution target is illuminated by the QCL output beam of 1.2 mm diameter. The signal is then magnified using a pair of lens ($f_1 = 4$ mm and $f_2 = 75$ mm) by a factor of 18.75 ($f_2/f_1 = 75/4$). The beam is then focused into the nonlinear crystal using lens $f_3 = 50$ mm for mixing with the 1064 nm pump laser field with a beam size of 1 mm (Fig. 3.2). By employing both crystal angle tuning and QCL wavelength tuning, a series of monochromatic images i.e. hyperspectral cube is achieved. In case of QCL illumination, the monochromatic image acquisition algorithm is straight forward compared to that of the globar illumination. With the narrowband illumination no deconvolution is required, monochromatic images are obtained just by summing the images obtained while rotating the nonlinear crystal. This process is repeated at every QCL wavelength of interest.

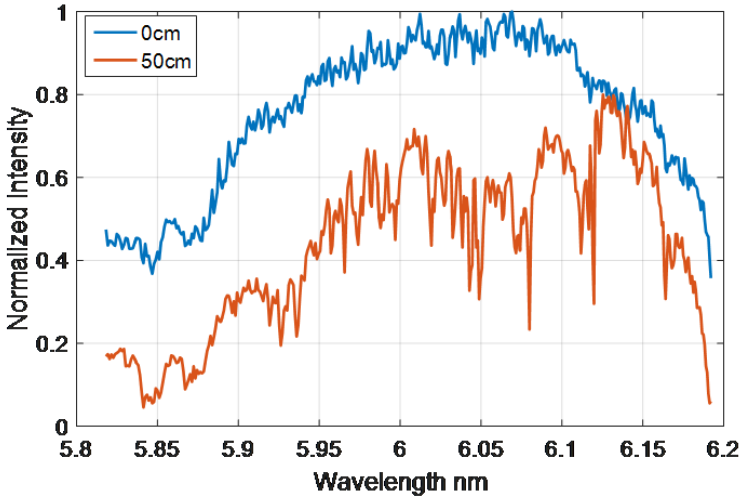

Figure 3.7: *Spectral tuning range of QCL measured with cooled MCT detector at 0 and 50 cm distance away from the laser cavity window. Water absorption lines can be noted in the red curve which corresponds to 50 cm distance from the laser cavity window.*

$$I_\lambda = \sum_{i=0}^{n} I_{up}(\theta_i) \tag{3.5}$$

$$I_{hsp} = I_{\lambda_1}, I_{\lambda_2}, I_{\lambda_3}, \ldots, I_{\lambda_m} \tag{3.6}$$

Where $I_{up}(\theta_i)$ represents the upconverted images at varying crystal rotation angles from 0 to n, I_λ represents a monochromatic image at wavelength λ and I_{λ_m} represents a series of monochromatic images from wavelength λ_1 to λ_m.

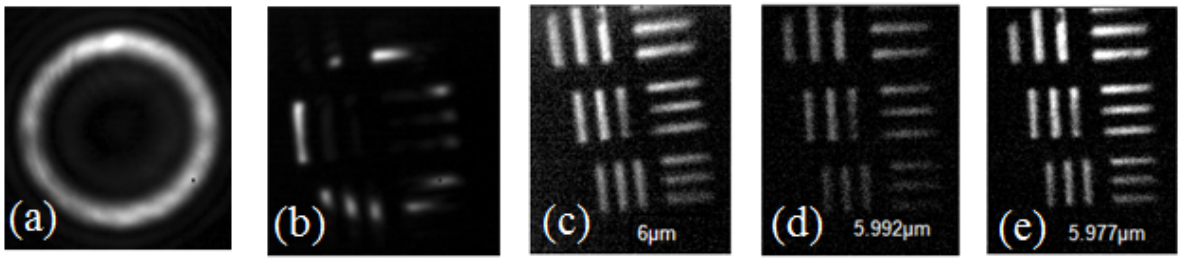

Figure 3.8: *Upconverted images (a) at 6 µm with magnification, with crystal rotated at* 11.05° *with camera integration time 10 ms, 1.5 W of pump power (b) with resolution target (c, e) Monochromatic (post processed) image of the smallest spatial features (14.25 lines/mm) of USAF resolution target at off resonance, and (c) on resonance of water absorption line.*

Figure 3.8(a) and 3.8(b) depicts single upconverted image with the magnification factor of 18.75 ($= f_2/f_1$) without sample and with USAF resolution target as a sample, respectively. The crystal is rotated to 11.05° and the pump power is set to approx. 1.5 W. A Visualization-5 (Corresponding Fig. 3.8(a-b)) has been made which depicts the effect of rotating the nonlinear crystal with respect to the $\vec{c}$-axis when the QCL wavelength was fixed at 6 µm. The crystal was rotated from 9.7° to 12.6° to cover the full FoV. Also speckles can be seen in the upconverted images in Fig. 3.8(c-e) showing the smallest features of the USAF resolution target (14.25 lines/mm i.e. 35.08 µm smallest resolvable element) with spectral water absorption features. The three images are taken ON and OFF resonance of a water absorption line which gives rise to the intensity difference. The measurement is taken by simply utilizing the water content in air with the path length of approx. 50 cm where the humidity in the lab was measured to be 32% at 22.6°C temperature. Visualization 6 (corresponding Fig. 3.8(c-e)) demonstrates the series of upconverted images while spectral tuning of QCL from 6.19 to 6 µm at a fixed crystal rotation angle of 9.752°.

3.3 Comparison of the globar and QCL based upconversion imaging

In this chapter, two different illumination sources were investigated with the same upconversion module and a comparison is made based on the pros and cons of both light sources. Globar, due to its low intensity, offers slow acquisition speed of images. Using the same upconversion module with a globar as an illumination source, the integration time of the camera was set to 500 ms whereas using a QCL leads to 50 times faster image acquisition per frame i.e. 10 ms. However globar, being a broadband source has the advantage of faster acquisition of whole set of data by a single sweep of crystal rotation angle, whereas, in case of QCL the process has to be repeated for every wavelength of interest. The monochromatic image acquisition algorithm is more straight forward in case of narrowband illumination, compared to broadband sources where the deconvolution of every wavelength contribution is required based on the phase-matching, before summing up the individual wavelength contribution to form monochromatic images. Using a narrowband illumination source for upconversion based hyperspectral imaging has the advantage of a constant spectral resolution of the image based on the linewidth of the source itself whereas in case of a broadband source, the spectral resolution is set by the acceptance bandwidth/crystal length of the upconversion device itself even leading to radially varying spectral resolution within a single image.

3.4 Summary

This work is, to the best of our knowledge, the first demonstration of mid-IR hyperspectral imaging based on upconversion technology in 6 to 8 µm spectral range. In this work AGS is used as nonlinear medium and two kinds of mid-IR illumination sources; broadband i.e. a globar and a narrowband source i.e. a QCL is used as an illumination source and mixed with a 1064 nm solid-state laser. The system is compared for the two different illumination sources primarily based on acquisition time and spectral resolution. A series of upconverted images is captured with a Silicon CCD camera while scanning the phase-match condition, i.e. rotation of the nonlinear crystal, which leads to fast acquisition of images containing radially distributed spectral information. No translation of the images was observed which shows that the upconversion is performed in the Fourier plane. A MatLab program is used for post-processing of the images to construct narrowband images based on the scanning of the phase-match condition. USAF resolution target is used as a sample and the smallest features of the target (14.25 lines/mm) have been resolved by applying magnification on the object (mid-IR) side. Water and polystyrene absorption lines have been used as spectral features in conjunction with USAF resolution

target. The imaging system can, in the implemented configuration resolve up to 4400 spatial elements within the FoV, which can be improved further by increasing the beam diameter of the pump laser or the FoV, however, at the expense of decreased intensity.

4 Video-frame-rate, mid-IR upconversion hyperspectral imaging

Nonlinear frequency upconversion provides an alternative route to fast, room-temperature mid-IR spectroscopy and imaging, due to orders-of-magnitude higher sensitivity and speed compared to direct mid-IR detectors [22]. A significant drawback in previous demonstrations of upconversion imaging has been the need for extensive post-processing to obtain a large FoV, which in turn prevents its use for real-time video-frame-rate imaging [19, 20, 47].

In this chapter, a high-speed upconversion mid-IR narrowband imaging system is presented using a synchronously-pumped optical parametric oscillator (OPO) delivering 20 ps pulses tunable in the 2.3 to 4 µm spectral range [45] for mid-IR illumination of the object. A LN crystal acts as the birefringent phase-matched nonlinear medium for the upconversion process, transferring the mid-IR signals to the NIR wavelength range, where a standard CCD camera is then used for image acquisition.

To increase FoV beyond the angular phase-matching acceptance of the nonlinear medium, we revitalize and expand on an idea dating back to the late 1960s, using angular rotation of the crystal [59]. Rotation of the LN crystal angle by a mere 1 degree is implemented by mounting the crystal on a Galvano-scanner (GVS), using "tangential phase-matching" (as described in section 2.1.5). This tiny rotation increases the FoV by a factor of approx. 5 compared to a fixed crystal angle, thus increasing the number of resolvable elements in the upconverted image by a factor of approx. 25. The FoV, using this approach, is limited primarily by the lens optics, well-known from standard imaging configurations. The flexibility provided by the GVS even allows compensation of the Gaussian signal intensity distribution by introducing a nonlinear scan of the crystal rotation angle, enabling a more uniform brightness in the upconverted image. The concept is not specific to this setup and can be applied universally for any upconversion imaging system.

Another important feature of the scanning technique is the elimination of image post-processing for large FoV narrowband image upconversion. Adjusting the crystal rotation cycle time to match the camera integration time, an image with increased FoV is acquired directly without post-processing allowing for video-frame-rate imaging. Narrowband

mid-IR upconversion imaging with a frame acquisition time of 2.5 ms is demonstrated, showing the potential to acquire up to 400 frames per second. The demonstrated spatial resolution is 35 µm within a 10-mm-diameter FoV in the object plane, providing approx. 64 K spatially resolvable elements.

4.1 Experiment

4.1.1 Setup

The setup is shown in Fig. 4.1, the mid-IR OPO is synchronously pumped at 1064 nm by a picosecond (ps) Yb-fiber laser operating at a repetition rate of 80 MHz (Fianium, FP1060-20). The duration of the Yb-fiber laser pulses is 20 ps and the bandwidth is approx. 1 nm. The maximum available average power is 15 W, out of which 10 W is used to pump the OPO, while the remaining 5 W (attenuated to 1.5 W to avoid camera saturation) serves as a pump field for the upconversion process, i.e. SFG.

The synchronous upconversion pumping scheme deployed here inherently locks the mid-IR OPO pulses and the pump laser pulses, minimizing timing jitter at the ps scale. This feature is intrinsic to synchronously-pumped ps OPOs, in contrast to ns-pumped OPOs where the individual output pulse builds up from parametric fluorescence, introducing timing jitter in the ns range [18]. The high temporal stability allows to operate the upconversion setup passively, using a fixed delay line adjusted to synchronize the mid-IR OPO pulse and the pump pulse to coincide inside the nonlinear crystal [18]. Synchronous pumping is highly efficient since the high peak power pulses interact in perfect temporal synchronism, resulting in efficient upconversion.

A MgO-doped periodically-poled $LiNbO_3$ (MgO:PPLN) crystal is used as the nonlinear medium in the OPO, generating the signal and the idler beam. The PPLN crystal is operated at constant temperature. Depending on the desired wavelength, either the signal or the idler beam is used for illumination. The signal wavelength can be tuned in the range of 1.43 to 1.98 µm with a bandwidth of 2 nm. The idler beam correspondingly covers the range of 4.1 to 2.3 µm with a bandwidth of 4 to 6 nm depending on the specific IR wavelength. The illumination bandwidth defines the spectral bandwidth of the narrowband images shown later. Further details of the OPO can be found in [45].In this work, only the idler beam is used for illumination of objects. The idler beam diameter is expanded to approx. 10 mm ($1/e^2$ of Gaussian), which defines the FoV in the object plane. An average power of 750-900 mW (depending on the wavelength) is available in a near-Gaussian intensity distribution. The pump beam for upconversion, i.e. the 1064 nm

laser, has a diameter of approx. 4 mm ($1/e^2$ of Gaussian) inside the nonlinear material.

A bulk LN crystal cut for birefringent phase-matching at an angle of 48° with respect to the $\vec{c}$-axis acts as the nonlinear medium for the upconversion process. The large transverse dimension of the bulk LN crystal compared to its PPLN counterpart, allows the use of a large pump beam diameter, enabling high spatial resolution in the upconverted images (the pump beam here acts as a soft Gaussian aperture, see section 2.1.4) [22]. It is further noted that other bulk crystals, e.g. $ZnGeP_2$ or AGS (as used in the previous chapter), constitute an important class of nonlinear materials available for mid-IR applications beyond 4.5 µm, thus affirming the generic nature of the proposed concept, enabling further extension of the upconversion imaging into the 5 to 12 µm range.

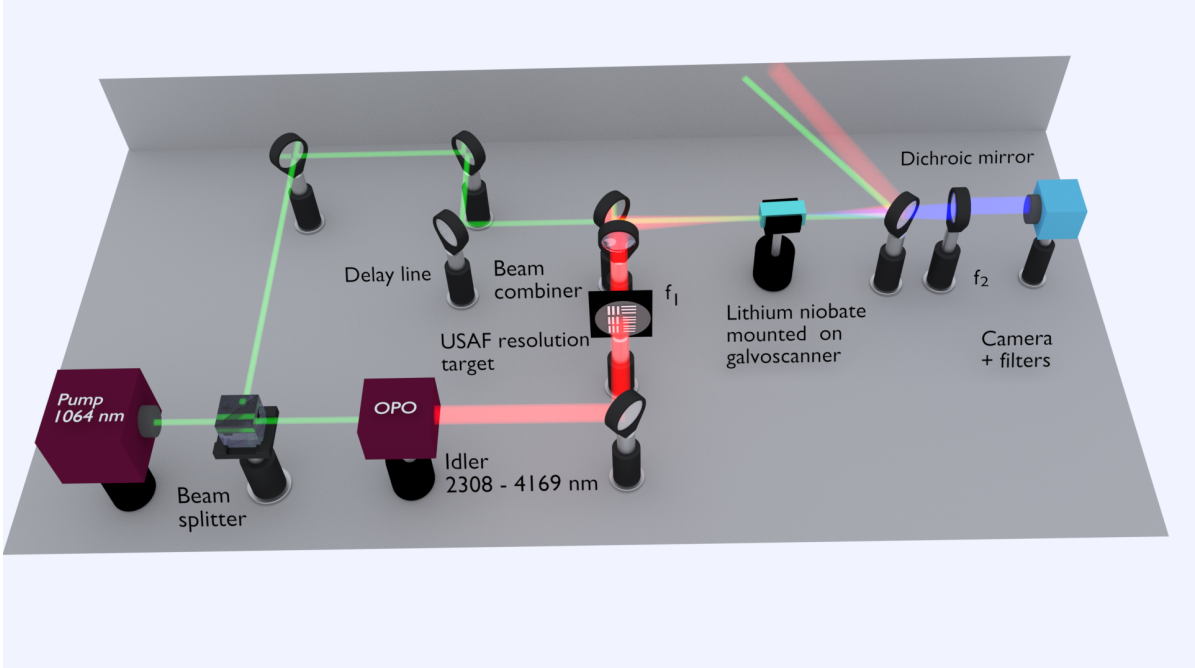

Figure 4.1: *Setup for the upconversion-based imaging, where the idler beam from a picosecond (ps) OPO is used as an illumination source and a synchronized ps 1064 nm laser source is used as a pump source. The beams are spatially and temporally overlapped in the nonlinear crystal (lithium niobate) for efficient upconversion. The phase-matching condition is scanned by rotating the crystal in synchronism with the camera integration time. Lenses, f_1 (50 mm) and f_2 (50 mm, 100 mm), are used at the front and back focal plane of the 4f setup. Filters (short-pass 950, long-pass 700) are used to block the residual pump/stray light.*

The upconversion setup is implemented as a 4f configuration, where the upconversion process takes place in the Fourier plane relative to the object. A first lens, Fourier transforms the two-dimensional mid-IR object field to the center of the LN crystal, where

synchronous upconversion to the NIR takes place. A second lens, Fourier transforms the upconverted NIR signal to form an image at the CCD camera chip [18–20, 47], see Fig. 4.1. A Si-based CCD camera (Andor Luca S) is used for the image acquisition. Filters (short-pass 950, long-pass 700) are used to block the residual pump and stray light from reaching the camera.

Different configurations exist for the frequency upconversion process. Using simple collinear interaction in a birefringent phase-matched material typically leads to a narrow and often highly elliptical FoV (section 2.1) [53]. However, choosing an appropriate off-set angle between the mid-IR signal and the pump beam, one can achieve a larger and more circular FoV. This geometry is commonly referred to as tangential phase-matching [53], see section 2.1.5 for details. As mentioned earlier, for a specific monochromatic/narrowband IR signal and corresponding crystal angle, a uniquely defined cone of mid-IR light is optimally phase-matched, corresponding to a ring pattern when Fourier transformed to the image plane. Changing the crystal angle successively, a set of concentric phase-matched rings will appear, each new ring adding to the FoV.

Angular tuning of the crystal, as proposed by Warner in 1969 [17], is a particularly efficient approach, since a tiny crystal rotation can lead to large change in the mid-IR phase-matching angle. However, at that time this suggestion seemingly had limited impact. Several other approaches to increase FoV have been proposed in recent years, however, these are complicated to implement, of limited generality, or slow in nature [15, 19, 47, 60]. Here we revisit the original idea of angle tuning, now including controlled continuous angle tuning and modern CCD camera technology. A superposition of partially overlapping upconverted images (or ring patterns) at the CCD camera chip, while scanning the phase-matching condition, preserves the image quality, producing a significantly increased FoV.

The need for post-processing of the images has been eliminated by introducing a GVS (Thorlabs GVS011) and image integration by the CCD camera. The nonlinear crystal is mounted on a GVS for automated and controlled rotation of the crystal. An analog/digital signal generator (USB-6211 National Instruments) is used to generate a synchronized voltage signal for the GVS and the CCD camera, respectively, using an external trigger signal (Fig. 4.2). A LabVIEW program then controls the GVS voltage setting to synchronize the GVS with the trigger signal of the CCD camera (Fig. 4.3). By integrating all the upconverted sub-images, while scanning the crystal angle in a predefined range, a large FoV is obtained without the need for post-processing. In practical terms, the GVS sweep averages out the sinc term from the phase-matching condition point by point. In particular, a nonlinear scan pattern can compensate for the Gaussian nature of the illumination source, thus generating a flat response over the full FoV, i.e. producing an isoplanatic imaging system.

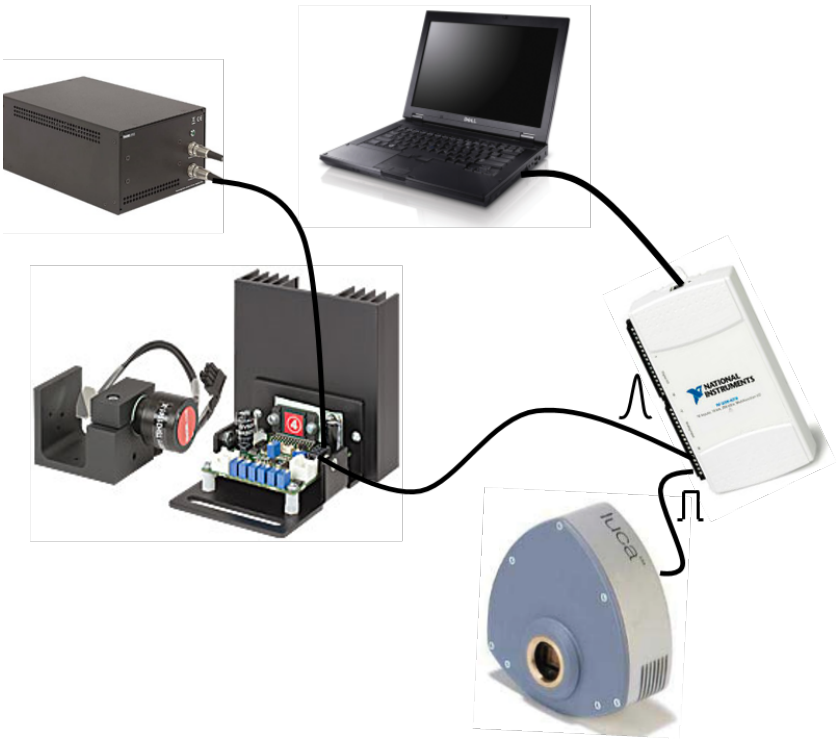

Figure 4.2: *Schematic representation of video-frame-rate electronics.*

Figure 4.2 is a schematic representation of the electronics used in combination with upconversion imaging setup for the video-frame-rate imaging. A National Instrument DAQ device (NI 6211) generates synchronized pulses to trigger the camera and the galvo-scanner. The Labview program controls the synchronized pulses (Fig. 4.3). Thorlabs GVS011 galvo-scanner is used for angular scan of the crystal. The mirror mounted on the scanner is replaced by a crystal holder. The potentiometers of the galvo-scanner circuit need to be adjusted according to the weight of the crystal and the mount.

An Andor Luca S camera is used for synchronous image acquisition. The camera allows the external trigger i.e., the camera integrates only when triggered while the exposure time is set by the pulse width.

4.1.2 Experimental results

In the following, the basic properties of the upconversion setup is investigated. Figure 4.4 is the non-collinear phase matching curves showing internal angle between the pump and signal beam vs. angle of the c-axis relative to the pump field for three different signal wavelengths i.e., 3104 nm, 3939 nm, 3547 nm. Figure 4.5 shows experimentally, as well

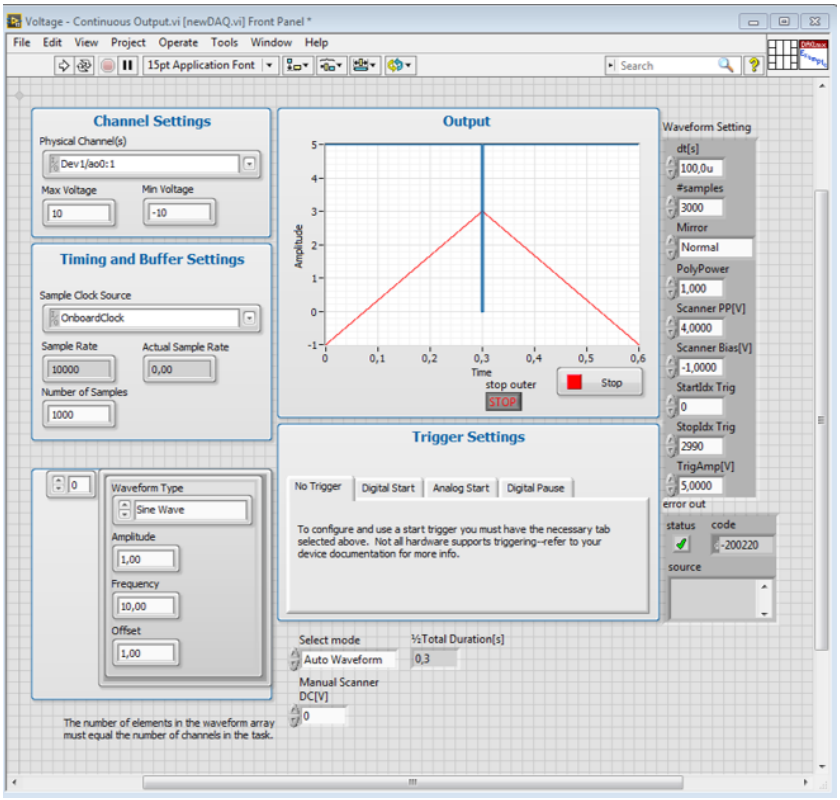

Figure 4.3: *Screen-shot of the Labview program used to generate synchronous pulses for camera trigger and galvanoscanner.*

as theoretically, the upconversion imaging process. A clear path USAF resolution target (Edmund Optics) is inserted in the object plane to demonstrate the spatial properties of the imaging system. Figure 4.5(a-c) shows measured upconverted images for different crystal rotation angles. Figures 4.5(d-f) show their simulated counterparts, confirming good agreement with the experimental measurements. To increase FoV in a narrowband image, the phase-matching condition can be tuned to upconvert different sections (rings) of the object plane, as seen in Fig. 4.5, and then combined to form an image with large FoV.

Figure 4.6(a-b) shows measured upconverted images, where Fig. 4.6(a) is single frame acquisition i.e. tangential phase-matching, and Fig. 4.6(b) is the post-processed upconverted image composed of superimposed individual frames captured manually at crystal rotation angles ranging from $-4.7°$ to $-3.7°$ in steps of $0.1°$. The ratio between the diameters of the two images is a direct measure of the increase in FoV.

The camera integration time for each frame is 0.47 ms, limited by the minimum exposure time setting of the camera. Even then, the pump source had to be attenuated (1.5

W) to prevent the camera from saturation, highlighting the advantage of synchronous upconversion for high quantum efficiency. Figure 4.6(c) shows the individual intensity profiles along the x-axis, while the dotted green line represents the sum of the intensity profiles. The intensity profile of the upconverted image is near-Gaussian, reflecting the intensity profile of the OPO idler beam. Figure 4.6(d) shows the measured beam profile

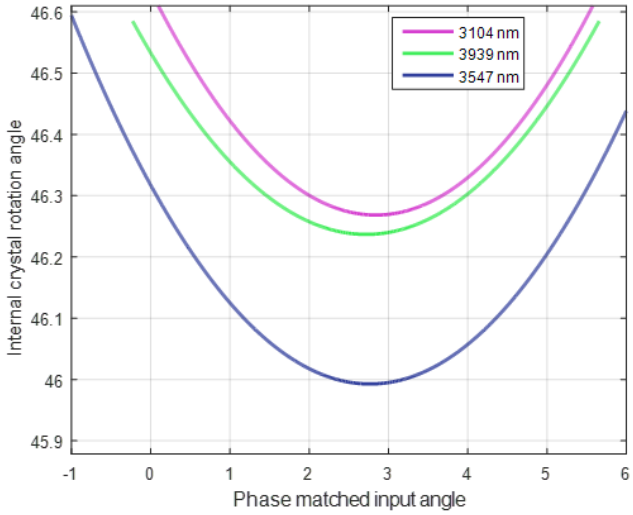

Figure 4.4: *Non-collinear phase-matching curves showing internal angle between the pump and signal beam vs. angle of the $\vec{c}-$ axis relative to the pump field for three different signal wavelengths.*

of the idler illumination source using a standard mid-IR camera. Figure 4.6(e) is the acquired image using the GVS performing a continuous linear scan of the crystal angles and integrating with the CCD camera. Figure 4.6(f) shows a comparison of the intensity profiles measured with the GVS scanner using post-processing with stepwise scanning of the crystal angle and single frame acquisition, using the proposed continuous scanning. Furthermore, the red graph shows the profile from direct detection with the mid-IR camera. The images are very similar, validating the use of continuous scanning using GVS as a practical method to increase the FoV. Figure 4.6(g-i) show the theoretically calculated images corresponding to Fig. 4.6(a-c), using the measured mid-IR beam profile as input.

To experimentally determine the spatial resolution, a standard USAF resolution target (Edmund optics clear path resolution target) is placed in the object plane, see Fig. 4.1. Figure 4.7 shows the upconverted image of the resolution target measured at 3.1 µm using GVS automatized acquisition without the post-processing. From Fig. 4.7(b) it is seen that the smallest feature of the resolution target of approx. 35 µm (14 lines/mm) can be resolved. The camera has a pixel size of 10 x 10 μm^2, whereas the upconverted

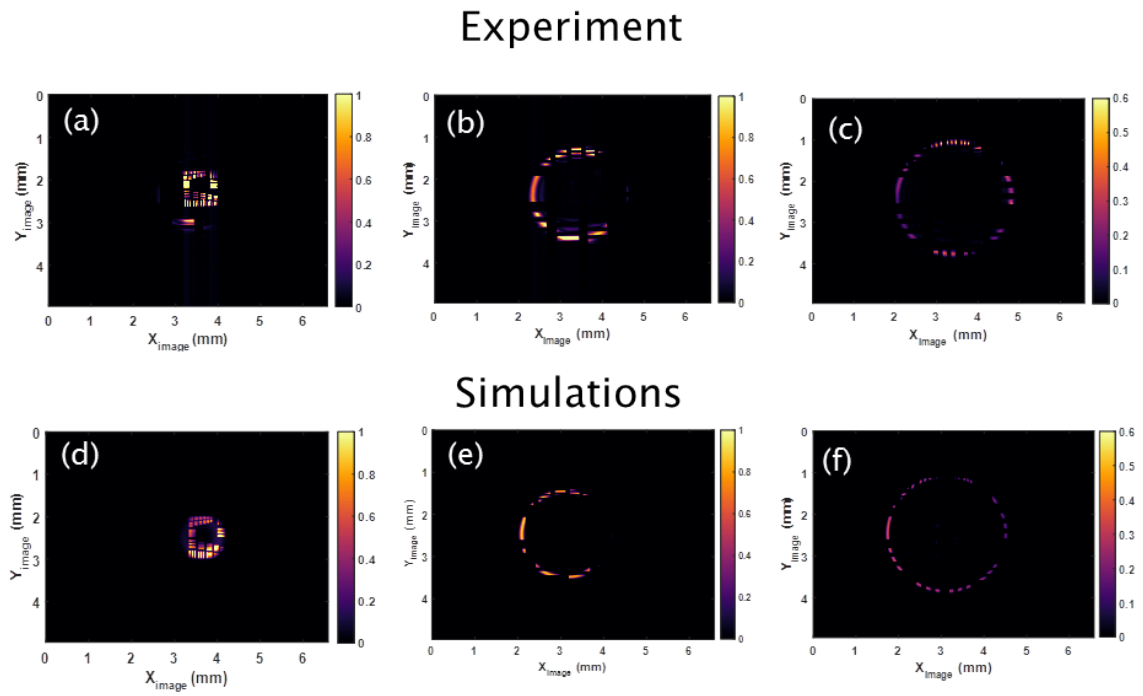

Figure 4.5: *Upconverted images of a USAF resolution target at 3.1 µm by varying the crystal rotation angle (−4.7°, −4.3°, −4.0°), (d-f) The corresponding simulated images at the same angles.*

spatial features on the camera are smaller (i.e. 8 µm) due to the de-magnification imposed by the upconversion process. Therefore, the lens, f_2 , was changed from 50 mm in Fig. 4.7(a) to 100 mm in Fig. 4.7(b). With a FoV of 10 mm in diameter and a resolution of 35 µm, the number of resolvable elements corresponds to approx. 64 K.

Using the parameters from the experiment in Eq. (2.22) i.e., $D_p = 4$ mm, $D_s = 10$ mm, $f_1 = 50$ mm, and $\lambda_s = 3.1$ µm, N equals 65 kpixels with a resolution R equal to 34 µm matching the experimentally estimated resolution of 35 µm, see Fig. 4.7. Although the model used for the calculation of the resolution is for incoherent illumination but still it fits well with the experimental value which is for coherent illumination.

Note that the expressions for R and N in Eq. (2.22) no longer includes the nonlinear crystal's angular acceptance parameters typically limiting the FoV, as commonly the case for upconversion imaging, thus highlighting the uniqueness of the proposed approach.

The pump beam diameter measurement has some uncertainty, which is believed to account for most of the difference between the measured a calculated number of resolvable elements within the FoV. Furthermore, there may be a small degradation in the upconverted image

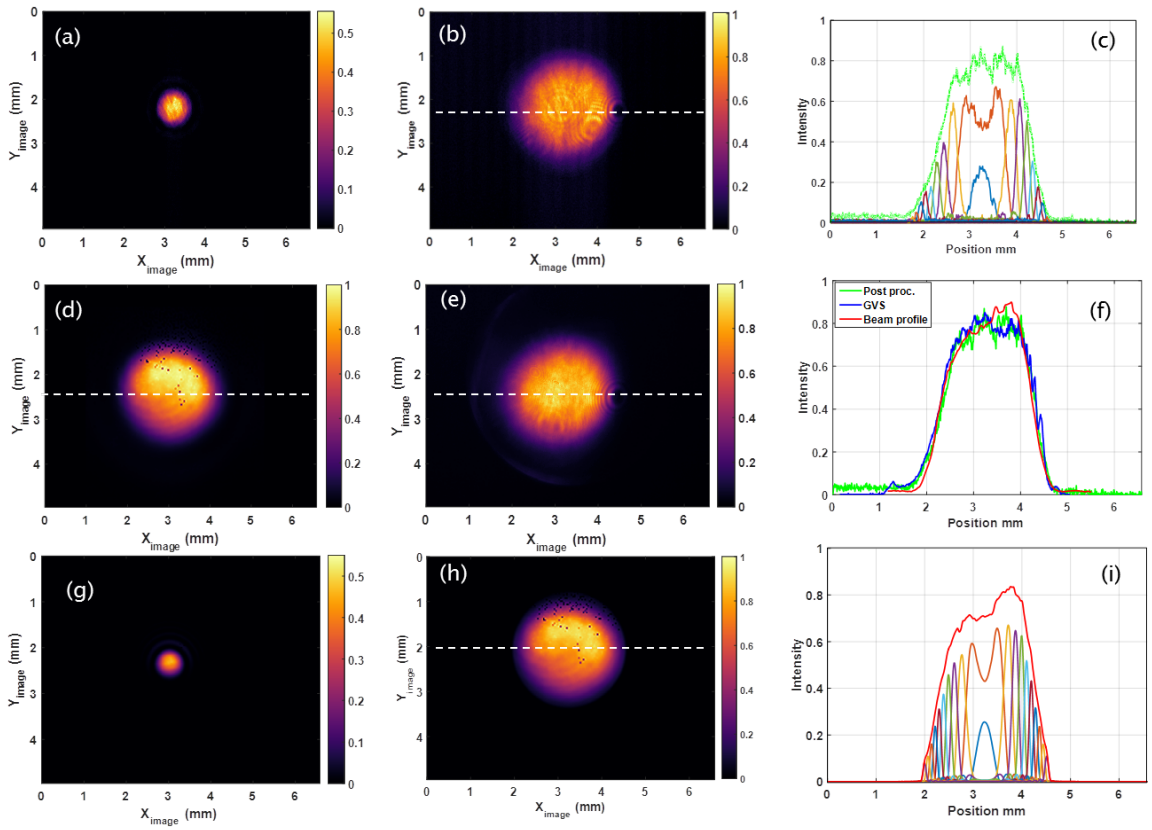

Figure 4.6: *Upconverted images (a) tangential phase-matching (b) rotating the crystal from* $-4.7°$ *to* $-3.7°$ *in step of* $0.1°$ *with respect to* $\vec{c}$*-axis and stitching the images together, camera integration time for each frame is 0.47 ms (c) intensity profile of the individual frames where the dotted line depicts the position in (b). (d) Image of the OPO idler beam acquired using a mid-IR camera, (e) upconverted image acquired using galvoscanner and a camera integration time of 2.5 ms, (f) intensity profile of (e) and (b) compared with intensity profile of (d). (g-i) simulated replica of (a-c) using (d) as mid-IR input.*

quality, caused by non-perfect beam quality of the pump laser or lens aberrations in the system.

The images presented so far all have a Gaussian intensity profile imposed by the mid-IR illumination source itself. To obtain a more homogeneous (top-hat) intensity profile over the full FoV, the angle of the nonlinear crystal can be scanned in a nonlinear fashion, such that the GVS rotates more slowly close to rim of the image compared to the center, where the mid-IR intensity is highest. This results in a more uniform/top-hat intensity profile, as shown in Fig. 4.8(c).

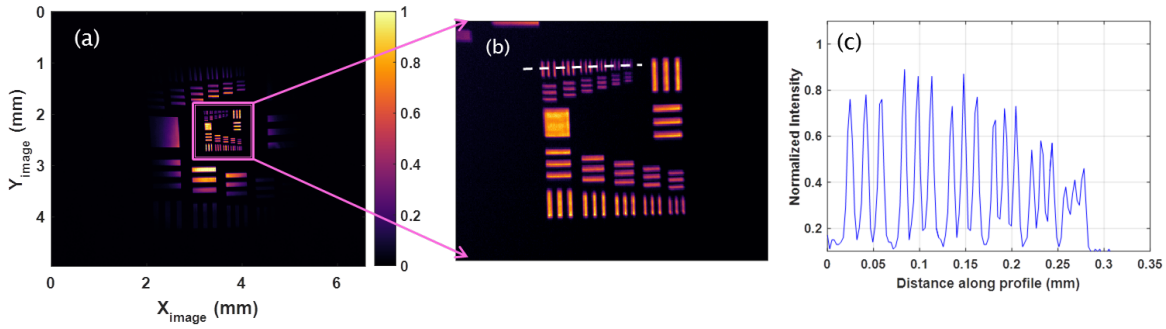

Figure 4.7: *Upconverted image of the resolution target at 3.1 µm rotating the crystal from −4.7° to −3.7° with respect to $\vec{c}$-axis using GVS for crystal rotation synchronous to camera integration time, camera integration time spent on each frame is 2.5 ms (b) magnified version of smallest features of resolution target i.e. square box in (a), f_2 was changed from 50 mm to 100 mm focal length for magnification (c) Intensity profile along the white line in (b) and pink circle highlights the smallest features.*

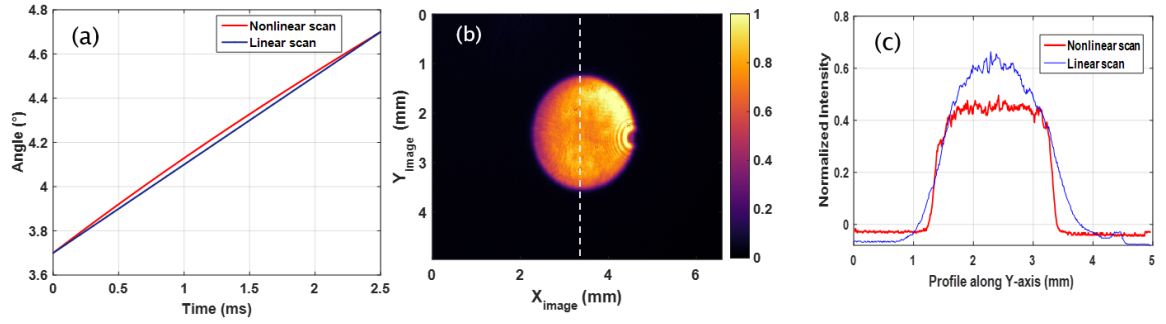

Figure 4.8: *(a) Plot showing the trend of the nonlinear scan (b) Upconverted image with a blank target at 3.1 µm with nonlinear scan, (c) intensity profile of the image with linear and nonlinear scans.*

Figure 4.8(a) shows the linear and nonlinear scan used to produce the top-hat-like intensity profile. Figure 4.8(b) shows the upconverted image at 3.1 µm using the GVS implemented the nonlinear scan. The scan speed is varied relative to the angle for the center part of the image, where θ_i is the crystal rotation angle. Figure 4.8(c) shows the intensity profile along the y-axis of the image in Fig. 4.8(b) using nonlinear scan, i.e. the red curve. Compared to that of a linear scan (blue curve), we do indeed observe a more top-hat-like intensity profile, however, due to a slight asymmetry in the IR beam the full potential was not realized here, see Fig. 4.6(d).

To illustrate video-frame-rate upconversion imaging, butane was sprayed from a gas lighter in the object plane. By tuning the hyperspectral upconversion camera system to match the absorption line of butane at 3.37 µm, a narrowband image is recorded.

Visualization-7 and 8 shows a recorded image sequence while spraying butane gas in the object plane in front of the resolution target, and without resolution target respectively (Fig. 4.9 are the corresponding snapshots). With a 2.5 ms exposure time, the imaging system can acquire 400 frames per second, but here limited to 40 Hz readout time of the NIR camera.

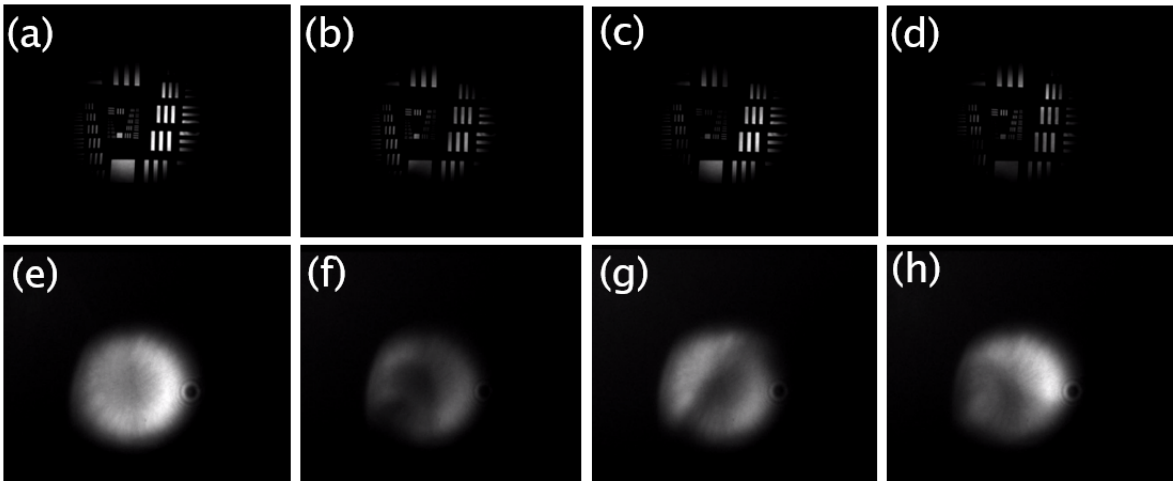

Figure 4.9: *Snapshots of the Visualization-7 and 8 i.e. a recorded image sequence while spraying butane gas in the object plane (a-d) in front of the resolution target, and (e-h) without resolution target respectively*

The signal-to-noise ratio (SNR) of the imaging system is estimated by varying the integration time of the camera. An image was captured at 2.5 ms camera integration time. To estimate the SNR, the infrared illumination beam (i.e. OPO idler beam) was blocked and the camera integration time was increased until the average noise intensity was equal to that of the image intensity, i.e. 225 (arb. units). This required an integration time of 2 s. By assuming that the noise is white in nature, the SNR (the ratio of average signal to standard deviation of the signal) is 424 for 2.5 ms exposure time.

With the parameters used in this work, the QE of the system was estimated using Eq. (2.19) (see section 2.1.3), this yields a $QE_{cw} = 5 \times 10^{-7}$. Considering upconversion of a Gaussian pulse (temporally) with a Gaussian pump pulse (temporally), the pulsed upconversion quantum efficiency can be calculated as $QE_{Gaussian} = QE_{cw}/\sqrt{2} \cdot dc$ where dc is the duty-cycle of the pulses.
Inserting values for the used setup gives a quantum efficiency of $QE_{Gaussian} = 0.02\%$.

Further, considering the large FoV, the phase-match condition in any part of the image is only fulfilled for a fraction of the camera integration time. Considering the QE for imaging a full FoV, we need to multiply with the fraction of the time where any given

part of the object is upconverted, which for our case is approx. 1/10, yielding an image upconversion quantum efficiency of $QE^{image}_{Gaussian} = 0.002\%$, for each of the 64 kpixels elements within the FoV. Note that the $QE^{image}_{Gaussian}$ can be scaled dramatically by using more efficient (and longer) nonlinear crystals such as PPLNs or increasing the mixing peak power.

4.2 Summary

In this section, we have presented, for the first time, a mid-IR narrowband imaging system based on upconversion with an enlarged FoV, operating at video-frame-rate (40 Hz, limited by the camera readout time), without the need for post-processing of the images. In the present setup, a 2.5 ms exposure time still required an attenuated pump beam to avoid camera saturation, showing that a potential frame rate of 1 kHz can be realized using a faster CCD camera. The high efficiency was obtained using a passively synchronized pumping setup. We obtained 64 kpixels in the upconverted image, applying only 1 degree of crystal rotation using tangential phase-matching. This result is in good agreement with the theoretically estimated resolution. The FoV was increased by a factor of 5 compared to a static design, corresponding to an increase of 25 times in the number of pixels. This number can be further increased by applying a larger numerical aperture at the input side, combined with a correspondingly larger crystal rotation angle. Eventually, the angular interrogation of the nonlinear crystal for upconversion will be limited by image distortion, originating from refraction at the crystal surfaces as discussed in section 2.1. Using e.g. a 6 degree rotation combined with tangential phase-matching could provide approx. 370 kpixels. A second approach to increase the number of pixels is by expanding the diameter of the pump beam inside the nonlinear crystal. However, this method will decrease the quantum efficiency of the conversion process. The mid-IR upconversion system operates at room-temperature, unlike other low noise mid-IR cameras with single photon detection capability, and with extremely short response time, here demonstrated with 20 ps pulses. Longer wavelengths can be upconverted using different nonlinear crystals such as AGS (e.g. 5 to 12 µm). We are confident that the simple and generic approach using crystal angle tuning with a GVS, mitigating the restriction of FoV imposed by the nonlinear phase-matching properties, will find widespread use for mid-IR hyperspectral imaging applications. One example has been presented, highlighting the potential for on-line IR imaging of gases. Fast biopsy screening by measuring disease specific compositional changes will be presented in the following.

5 Upconversion imaging of cancer biopsies

A second example of the applicability of the system presented in Ch. 4 is illustrated in Fig. 5.1. Here, the mid-IR illumination beam is scaled by lenses to match the size of a typical medical biopsy, i.e. approx. 2 mm in diameter. The mid-IR is illuminating the tissue sample followed by a magnification to the 10-mm-diameter as used in the previous section. This is used as the object beam for the upconversion imaging system.

The sample under investigation is a tissue micro array containing samples of 35 patients with oesophageal ardenocacinoma and 5 healthy controls. Two consecutive sections have been purchased from Biomax.us. The first section has been mounted on an CaF_2 slide (Crystan) for investigation in the mid-IR. The second one was mounted on a standard histological glass slide to provide a gold standard reference information from a histopathologist via H & E staining. One healthy and one tumour sample have been selected for investigation.

Measuring two images, one with and one without the tissue samples, allows for a pixel-by-pixel calculation of the transmittance through the sample at the illumination wavelength, here at 3.34 µm shown in Fig. 5.2.

5.1 Experiment

Figure 5.2(a) is an image of the cancerous tissue while 5.2(b) shows the healthy tissue. In this example, the spatial resolution in the tissue sample plane is approx. 9 µm, taking into account the scaling systems introduced in Fig. 5.1. Spectral tuning, provided by OPO is exploited to scan the illumination wavelength for the tissue sample. This provides spectral information at every pixel within the image. Therefore, the absorption spectrum at every pixel of the sample can be calculated.

A fringe-like interference/speckles pattern can be noted on the images in Fig. 5.2. This is

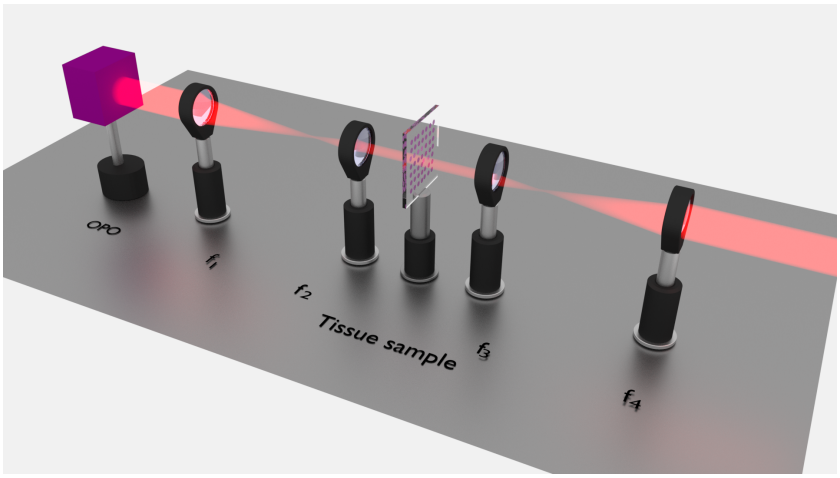

Figure 5.1: *Magnification setup for the imaging of the tissue sample to resolve the smaller features of the sample. The original size of the beam coming from OPO is 10 mm, which is reduced to 2 mm, using a pair of lenses: $f_1 = 250$ mm, $f_2 = 50$ mm. This 2 mm beam illuminates the tissue sample (The size of one sample is roughly 2 mm), the sample shown in the setup contains several biopsy samples mounted on a 1 mm thick CaF_2 substrate. After passing through the sample (red stained for visibility in the setup), the beam is magnified again by 5 times, using a second pair of lens: $f_3 = 50$ mm and $f_4 = 250$ mm. This magnified beam is then used as the object in the upconversion imaging system, as shown in Fig. 4.1.*

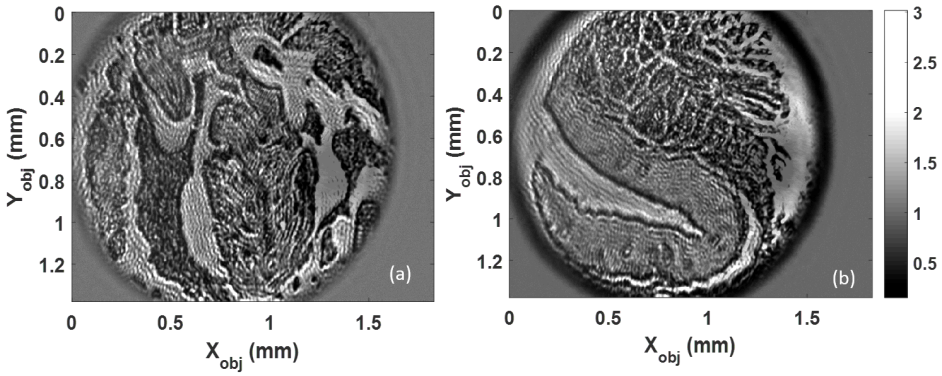

Figure 5.2: *Image of the tissue sample (a) cancerous, and (b) healthy tissue sample, acquired using upconversion at 3.006 µm wavelength*

due to the coherent nature of the illumination source used i.e. the OPO. Coherent light when passing through the sample, gets diffracted from the boundaries of tiny features and phase variations in the sample, when diffracted light with small phase shifts interferes, is can cause fringes/speckles in the image. Furthermore, it can be seen in Fig. 5.2 that the

transmission of the samples overshoots 1, which means that sample contains regions with light intensity brighter than the illumination source. This is also due to the interference of the coherent light in the sample.

A reflective diffuser (ground glass coated with silver), mounted on a spinning disk, is used to scramble the spatial coherence of the light source, see Fig. 5.3. The light coming from the OPO is first reflected from the diffuser and then passed through the magnification system as mentioned earlier in Fig. 5.1. The output angles of the light reflected from diffuser can be in the range of -20 to +20 degree. The strong divergence and large output angles reduce the brightness of the illumination. The loss in the brightness can be reduced by using a smaller input beam (2 mm in our case), however the larger the beam, the more effective the diffuser is to break the coherence of the light beam.

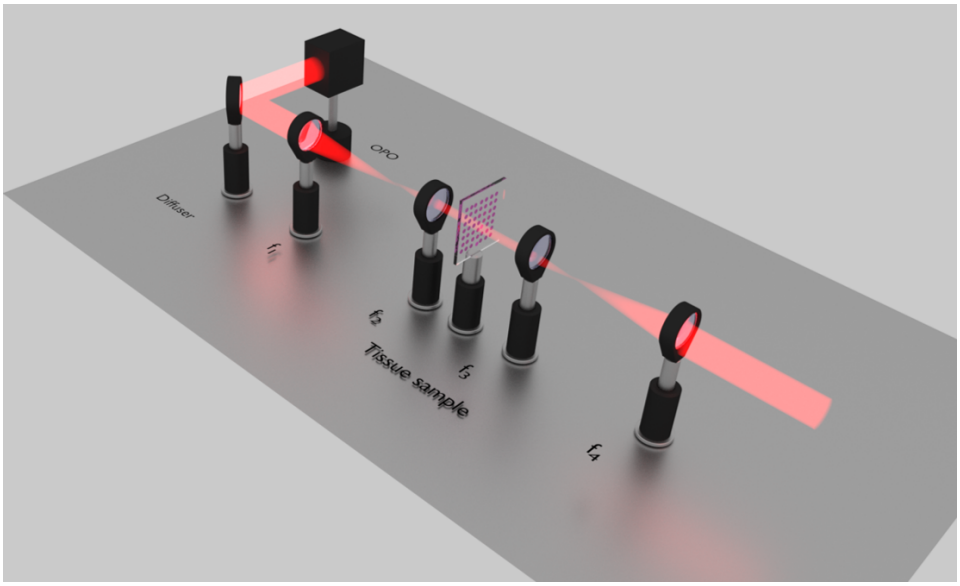

Figure 5.3: *Setup using diffuser*

Figure 5.4 represent the upconverted images using diffuser, where Fig. 5.4(a) is acquired while diffuser was not spinning and Fig. 5.4(b) is acquired when diffuser starts to spin. Figure 5.5 shows the upconverted images of the tissue samples when the diffuser is incorporated in the setup. It can clearly be seen that the speckles have reduced drastically due to the spinning diffuser when compared to Fig. 5.2. Figure 5.6 shows the pathology of the samples annotated from H & E stained slide by a pathologist.

Figure 5.7 shows the comparison of images obtained from FTIR and upconversion. The first row of Fig. 5.7 contains the images of the tissue samples based on FTIR and upconversion, the second row contains the corresponding spectra and the third row represent the clustering.

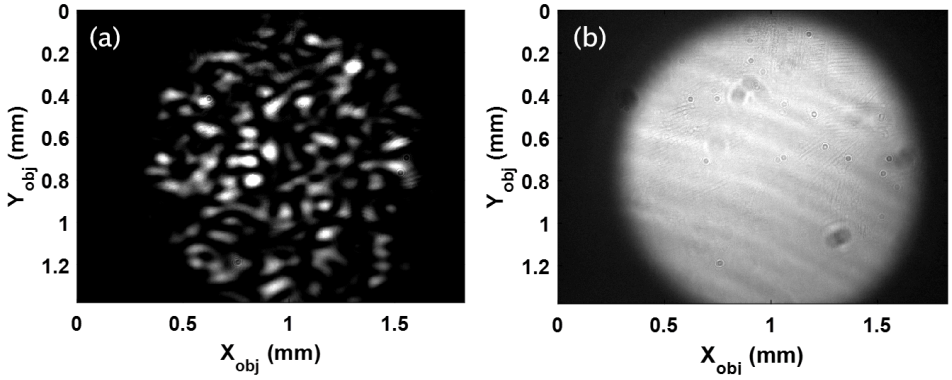

Figure 5.4: *Upconverted images acquired using diffuser at 3.5 µm wavelength with diffuser (a) OFF, and (b) ON*

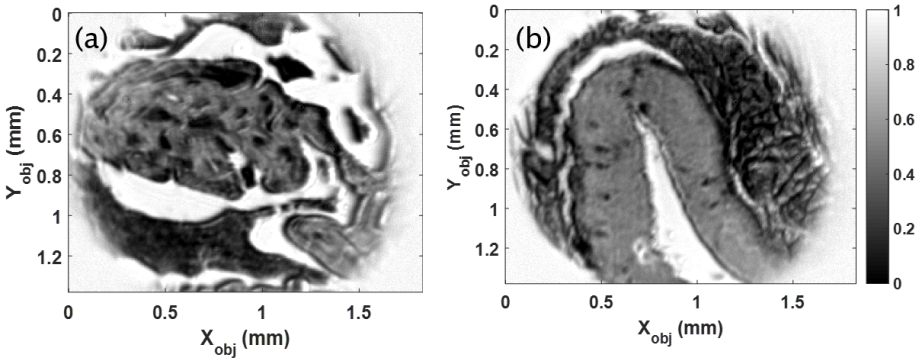

Figure 5.5: *Upconverted images of tissue samples (a) cancerous, and (b) healthy, acquired using diffuser at 3.5 µm wavelength.*

FTIR images were obtained using an Agilent Carry FTIR system (Agilent 620 FTIR microscope coupled with an Agilent 670 FTIR spectrometer). The system consists of a globar illumination source, and a liquid-nitrogen cooled 128 × 128 pixels focal plane MCT detector. A cassegrain IR objective with numerical aperture (NA) of 0.62 and 15 times magnification was used for imaging resulting in an effective pixel size of 5.5 × 5.5 µm. The interferometer was configured to achieve 4 cm^{-1} spectral resolution.

The H & E stained section was imaged under a standard white-light microscope (Zeiss Axio scan). The stained images obtained were assessed by a pathologist for annotation, see Fig. 5.6. The data acquired from the upconversion imaging system was loaded into 'R' via the 'hyperSpec' package. The FTIR images were cropped to match the spectral range of the upconversion system of 2770 to 3345 cm^{-1}. The upconversion spectra where then smoothed using a loes-function. The images where then analysed using R's generic k-means functionality. The annotations obtained from the pathologist where digitalised

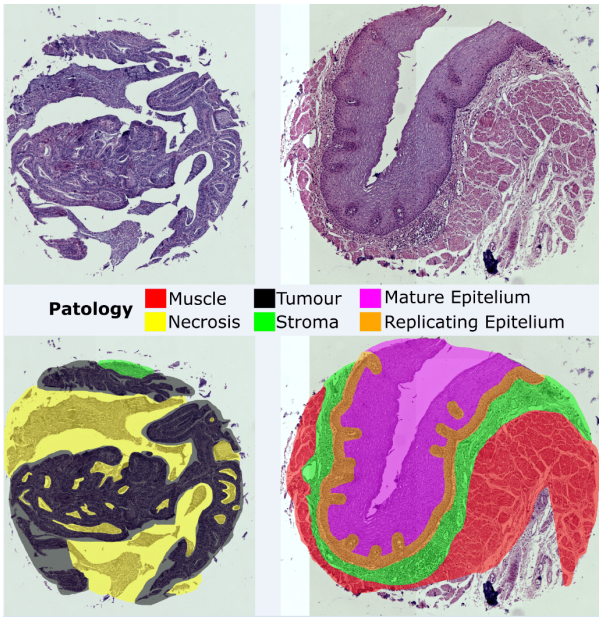

Figure 5.6: *The pathology of the samples annotated from an H & E stained slide by a pathologist*

using the original white-light images. The images were loaded into the open source software GIMP and a false-color mask was drawn manually and exported as a '.png' file.

The mid-IR images obtained from the FTIR as well as from the upconversion system were loaded from the proprietary formats using Matlab. The upconversion data then was corrected for optical distortion caused by the upconversion process, i.e., the wavelength dependent magnification factor attributed to transverse phase-matching condition (see section 2.1).

A great agreement between the images obtained from FTIR and upconversion can be noticed. However, the spectral resolution in the upconversion based spectrum is not as good as he FTIR based spectrum. this might be improved by coarse wavelength tuning. In this experiment, the upconversion based images were acquired for 60 wavelengths. The camera integration time for each upconverted image was 400 ms.

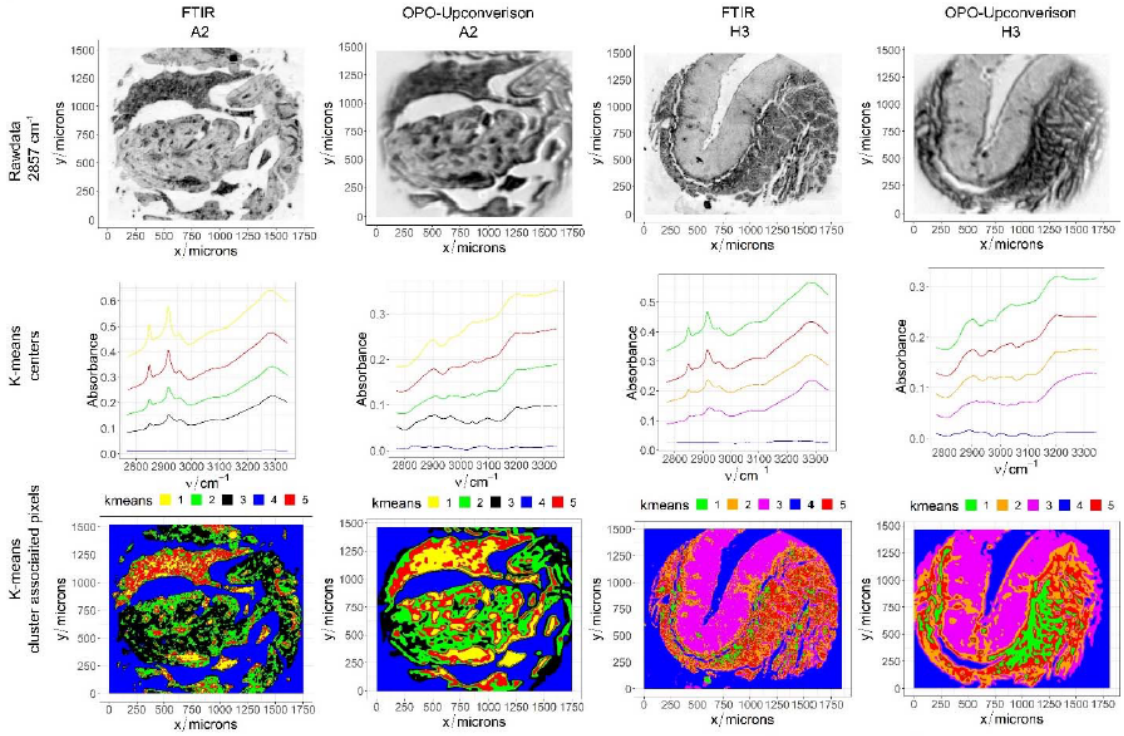

Figure 5.7: *Comparison of upconverted images with FTIR images. First row represent the images of the tissue samples based on upconversion and FTIR. Second row presents extracted spectrum while 3rd row represents clustering.*

Comparison of the mid-IR imaging methods (Ref. [5, 61, 62])						
Imaging methods	**Spatial resolution**	**Acquisition time/frame**	**Spectral resolution (cm^{-1})**	**Spectral range (cm^{-1})**	**Detectors**	**FoV**
FTIR	Diffraction limited	2 min.	4	5000-800	MCT-FPA	140×140 µm^2
SPERO (Daylight solution)	Diffraction limited	90 ms	2	1750-1000	Micro-bolometer-FPA	2×2 mm^2
Confocal microscope	Diffraction limited	2.4 s	1	1940-770	MCT	140×140 µm^2
Upconversion	Diffraction limited	400 ms	4.5	5000-800*	CCD	2×2 mm^2

* In this work, the spectral range of upconversion imaging presented is smaller, but it is

possible to cover the range of $5000 - 800$ cm^{-1} by exploiting different nonlinear media.

5.2 Summary

Here an upconversion mid-IR imaging setup is implemented to image histological sections is demonstrated for the very first time. A tissue biopsy sample containing sections of oesophageal tissue was used for the proof of concept. The pathology of the samples has been annotated from an H & E stained slide by a pathologist as depicted in Fig. 5.6. Sample A2 is a section containing necrotic tumour whereas sample H3 is from healthy tissue. The unstained section of the same sample was measured on a conventional FTIR as well as on the upconversion system.

The upconversion systems achieves comparable performance to the FTIR system regarding image quality (i.e. contrast, spatial and spectral resolution), see Fig. 5.7 row 1, and the system is able to achieve contrast between pathology groups. In Fig. 5.7 row 3 the cluster dependencies of each image pixels are visualised and those somehow match between FTIR and upconversion system but needs more work for improvement. In the tumour sample there is contrast between necrotic (cluster 1 and 5) and tumour tissue (cluster 2 and 3). In the healthy sample there is also clear differentiation between epithelium (cluster 4) and connective tissue (cluster 2, 3 and 5). Furthermore, there is a notable difference in the CH-stretching vibrations absorptions (2950 cm^{-1}) relative to the amide absorption (broad feature above 3200cm^{-1}) between the healthy sample and the tumour sample.

The upconversion based imaging system has potential for fast and automated medical biopsy analysis based on the chemical fingerprint in the mid-IR range, potentially allowing for the use of endogenous molecular chromophores for medical diagnostics, rather than using exogenous staining, as is the gold standard of histopathology.

Note: The FTIR-based part of the work is done by our partner Michael Hermes at Exeter University, UK.

6 Point-Spread function engineering in upconversion imaging

In this section, PSF engineering in upconversion imaging of static and dynamic NIR (1064 nm) phase/amplitude objects is demonstrated resulting in edge-enhanced images in the visible spectral range (635 nm) using SFG in a PPLN crystal. Through the SFG scheme, the Spiral Phase (SP) filter operates at a wavelength (1575 nm) different from that of the signal. This offers some advantages in the absence of high-performance SP filters and cameras operating at the signal wavelength (especially for mid-IR signals). Furthermore, we confirm experimentally and numerically that upconversion PSF engineering can be extended from collinear to noncollinear interactions between signal and pump. Simultaneous collinear and noncollinear edge-enhanced imaging of phase objects in real-time is also demonstrated using broadband illumination with a spectral bandwidth of 6.4 nm, resulting in ten-fold increase in the FoV area of the imaging system.

Edge detection is a well-known technique and has been used for decades to detect spatial variations in amplitude objects or phase variations within an object e.g. caused by the refractive index variations within a cell [63]. The technique is typically performed by filtering the image information in its Fourier domain usually by physical spatial filters of the imaging system [50]. The use of a spiral phase filter that creates an optical vortex or phase singularity is a new technique used to perform edge detection of phase or amplitude objects. However, previous demonstrations of spiral phase contrast (SPC) imaging were limited only to the VIS and NIR spectral regimes [56, 64]. This work presents, to the best of our knowledge, the first demonstration of PSF engineering in upconversion based imaging system with an expanded FoV exploiting collinear and noncollinear phase-matching in PPLN crystal. Two kinds of illumination sources, i.e., a narrowband DPSS at 1064 nm and a broadband supercontinuum (SC) source, are used in combination with a pump source for upconversion, i.e., an Erbium-doped fiber laser at 1575 nm.

Since upconversion takes place in the Fourier plane and the 1575 nm pump beam acts as a soft aperture in upconversion imaging [22], the pump beam profile can be modified/engineered for spatial filtering.

In this work, a combination of spatially varying half-wave plate (SVHWP) sandwiched between two quarter-wave plates (QWP) is used to generate spiral phase/optical vortex in the pump beam [65].

Upconversion based PSF engineering has recently been demonstrated but exploiting only the collinear phase-matching either in second-harmonic generation [24] or sum-frequency generation [46] which leads to limited FoV. Based on the theoretical modeling described in section 2.1.7, simulated images are presented and compared with experimentally acquired images in the following section, using monochromatic DPSS laser and broadband SC source. Also, supplementary numerical results investigate the effects of the finite PPLN crystal size and the vortex core of the pump beam on the upconverted images are discussed. Finally, we summarize our results and discuss some outlook in the end of the section.

6.1 Numerical simulations

Based on the numerical model described in section 2.1.7, PSF engineering in collinear and non-collinear upconversion imaging is simulated. Figure 6.1 illustrates simulated upconversion based edge enhanced images of binary $0-\pi$ phase grating when a monochromatic illumination (@ 1064 nm) source is used at varying PPLN operating temperatures where Fig. 6.1(a-d) are without and 6.1(e-h) are with optical vortex of the pump beam with topological charge $m = 1$ and 6.1(i-l) with $m = 2$.

It can be seen that using $m = 1$ is more advantageous in terms of the contrast as compared to $m = 2$. As mentioned in section 2.1.7, topological charge $m = 2$ is used to detect curved edges (either phase or amplitude) of the object but in the present case, we use it for the principle of dark field imaging using the blurring effect of a pin-hole.

Figure 6.2 shows simulated upconversion based edge-enhanced images of binary $0-\pi$ phase (a,e) grating (b,f) checker-board pattern, (c,g) resolution target (d,h) globe, for the case of broadband illumination source, with optical vortex present in the pump beam where Fig. 6.2(a-d) corresponds to $m = 1$ and 6.2(e-h) to $m = 2$.

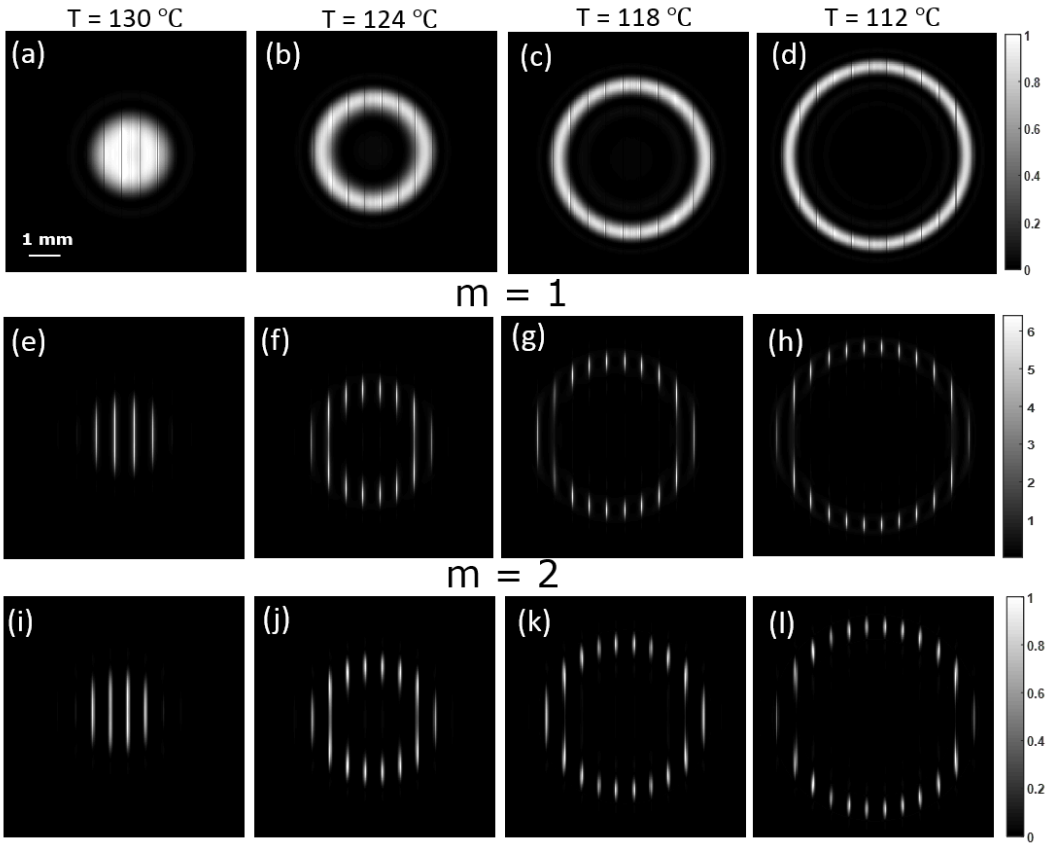

Figure 6.1: *Simulated monochromatic upconverted images of a binary* $0 - \pi$ *phase grating at different PPLN crystal temperature (a,e,i)* $T = 130°C$*; (b,f,j)* $T = 124°C$*, (c,g,k)* $T = 118°C$*; (d,h,l)* $T = 112°C$ *in the absence (a, b, c, d), and presence (e, f, g, h) of a spiral phase filter* $m = 1$*, and (i, j, k, l)* $m = 2$ *applied to the 1575 nm pump beam. Scale bar is 1 mm on the object plane.*

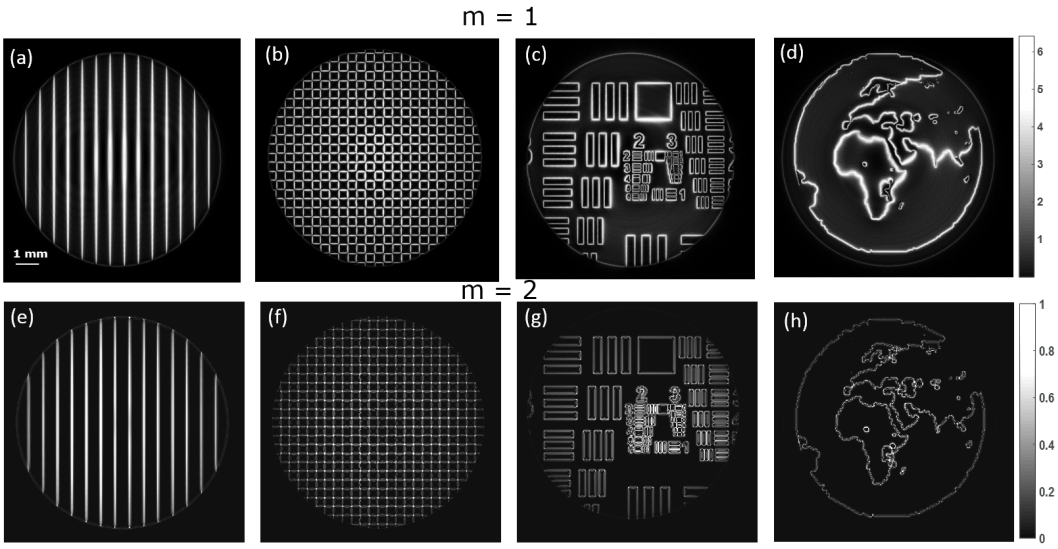

Figure 6.2: *Simulated polychromatic upconverted images of binary* $0 - \pi$ *phase objects i.e. (a,e) bars, (b,f) checker-board, (c,g) resolution target, and (d,h) globe, with spectral range from 1052.9 nm to 1059.3 nm at* $60°C$ *PPLN crystal temperature in the presence of a spiral phase filter applied to the 1575 nm pump beam where (a-d) are simulated using* $m = 1$ *and (e-h) correspond to* $m = 2$*. Scale bar is 1 mm on the object plane.*

6.2 Experimental results

6.2.1 Experimental setup

The experimental setup is shown in Fig. 6.3. Periodically poled lithium niobate (PPLN) crystal (aperture of single channel = 1×1 mm^2, length = 10 mm) is used as a nonlinear medium. A poling period of 11.8 µm is used in this experiment. A 1575 nm CW Erbium-doped fiber laser (@ 500 mW optical power) is used as a pump source for sum-frequency generation whereas two types of signal sources are used, i.e., narrowband and broadband. The narrowband source used is a 1064 nm CW (@ 400 mW optical power), diode-pumped solid-state (DPSS) Nd:YVO_4 laser. Collimation optics is used to produce a 1064 nm beam with beam waist radius of 4 mm. The PPLN temperature is set to $T = 130°C$ for collinear phase-matching of 1064 nm and the mixing field of 1575 nm. The temperature can be tuned for non-collinear phase-matching to upconvert the 1064 nm signal with larger angles of incidence (see dashed red lines in Fig. 2.18), thereby increasing the FoV.

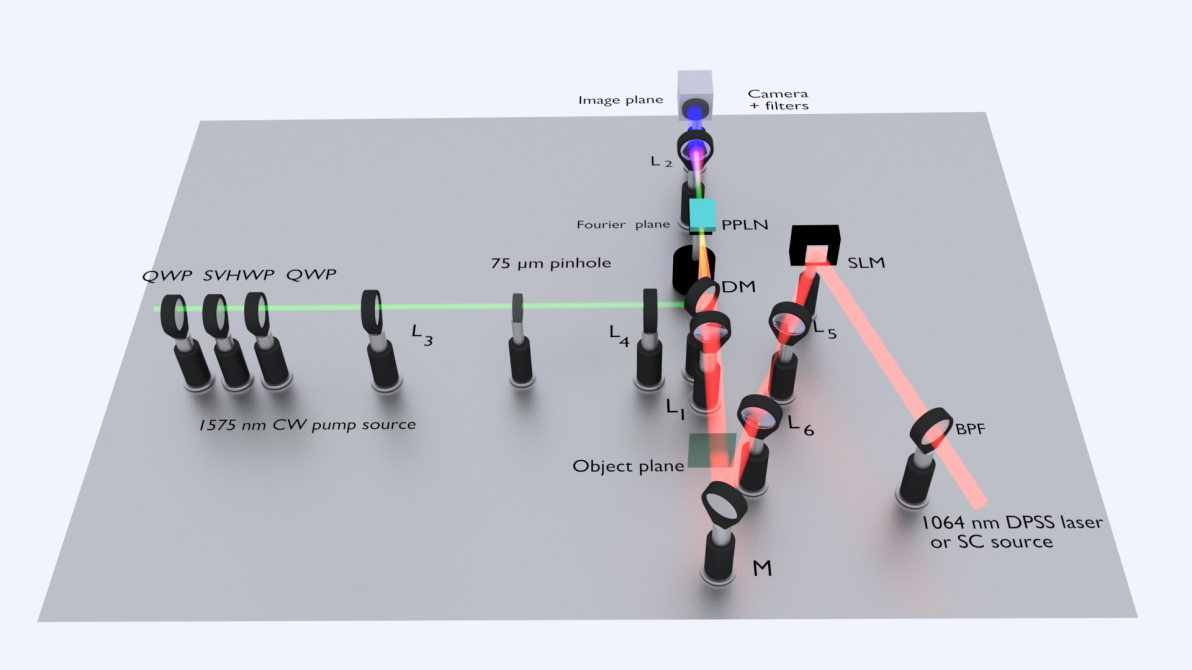

Figure 6.3: *Setup for upconversion based dark field imaging. A PPLN crystal is used as a nonlinear medium for sum-frequency generation. 1575 nm CW fiber laser is used as a pump source while two types of light sources are used as signal/illumination source: (1) monochromatic 1064 nm laser based on Nd:YVO_4 pumped by an 808 nm diode laser, (2) NIR supercontinuum source. A combination of (spatially varying half wave plate) SVHWP sandwiched between two QWPs is used to generate a spiral phase pattern for the pump beam with $m = 2$. An SLM is used to create static or dynamic phase objects. The system consists of three 4f imaging setups: (1) imaging system of the upconversion where the PPLN crystal is in the shared Fourier plane of lenses $L_1(f_1 = 60\ mm)$ and $L_2(f_2 = 45\ mm)$, (2) imaging setup with lenses $L_3(f_3 = 75\ mm)$ and $L_4(f_4 = 45\ mm)$ to project the pump beam with spiral phase onto the crystal plane/Fourier plane of the upconversion imaging system, (3) imaging setup with $L_5(f_5 = 100\ mm)$ and $L_6(f_6 = 200\ mm)$ to project the SLM phase pattern onto the object plane of the upconversion imaging system. A silicon based camera (IDS) is used for image acquisition and spectral filters are used to block the residual pump, unconverted signal and stray light.*

The broadband illumination source used is a NIR supercontinuum (SC) source emitted from a polarization maintaining (PM) single-mode fiber. The SC source beam is also collimated to produce a beam waist radius of 4 mm and is sent through a bandpass filter (BPF) that limits the spectral width to about 10 nm (FWHM) centered around 1056 nm. For broadband illumination, a fixed PPLN temperature $T = 60°C$ is used and the non-collinear signal rays are now phase-matched for slightly longer wavelengths than

the collinearly phase matched wavelength, see Fig. 6.6. A combination of a spatially varying half-wave plate sandwiched between two quarter-wave plates, combined working as a spiral phase plate ($m = 2$) is used in the pump beam path to impose a spiral phase on the Gaussian pump beam [12]. A liquid-crystal-on-silicon spatial light modulator (LCOS-SLM, Hamamatsu) is used to generate static or dynamic phase-only objects to be upconverted.

The setup consists of three 4f imaging systems where the first system (4f-1) is formed using lenses L_1 and L_2 and the nonlinear crystal lies in the Fourier plane of this 4f setup. The second system (4f-2) is formed by lenses L_3 and L_4 which is used to image the pump beam with spiral phase onto the crystal plane, i.e., the Fourier plane of 4f-1. A 75 µm pin-hole is used in the Fourier plane of 4f-2 to blur the size of the vortex core in the center of the pump beam appearing in the Fourier plane of 4f-1, which is important for sufficient spatial filtering i.e. dark field imaging. The size of the dark core of the pump has to be large enough to suppress the upconversion of the low spatial frequency components in order to obtain high-contrast edge-enhancement (see section 6.3 for more details on the effect of varying the vortex core size on the output upconverted image). The third system (4f-3) consists of L_5 and L_6 and is used to scale the SLM phase pattern onto the object plane of 4f-1, to be upconverted with dark field imaging edge-enhancement.

6.2.2 Narrowband illumination

First, the narrowband 1064 nm DPSS laser is used as illumination source for upconversion based dark field imaging. The temperature of the PPLN crystal is set to $T = 130°C$ for collinear phase-matching of 1575 nm and 1064 nm. The temperature can be tuned for non-collinear phase-matching thereby increasing the FoV. Figure 6.4 shows upconverted images of a phase object (a binary 0-π phase grating). Tuning the temperature from $T = 130°C$ to $T = 112°C$, collinear to non-collinear phase-matching is shown. Several images are acquired at different temperature settings of the PPLN crystal, i.e., from $T = 130°C$ to $T = 112°C$ in steps of $2°C$. These images are stitched together to form a large FoV upconverted image (see Visualization-9, Fig. 6.4, 6.5). This process is done for both configurations, i.e., with and without a spiral phase filter. Figure 6.4 depicts four of the images acquired with temperature tuning, with and without spiral phase for spatial filtering. Figure 6.4(e-h) shows that a spiral phase filter in the path of the pump beam can be exploited for high-pass spatial filtering not only for collinear phase-matching but also for non-collinear phase-matching. Typically spiral phase with topological charge $m = 1$ is used for filtering. However due to the lack of availability we have used $m = 2$ spiral phase and blurred it using a pin-hole (see Fig. 6.3) for dark field imaging. By exploiting temperature tuning, the FoV is increased by almost an order of magnitude in this demonstration. Camera integration time is set to 19.3 ms for each frame.

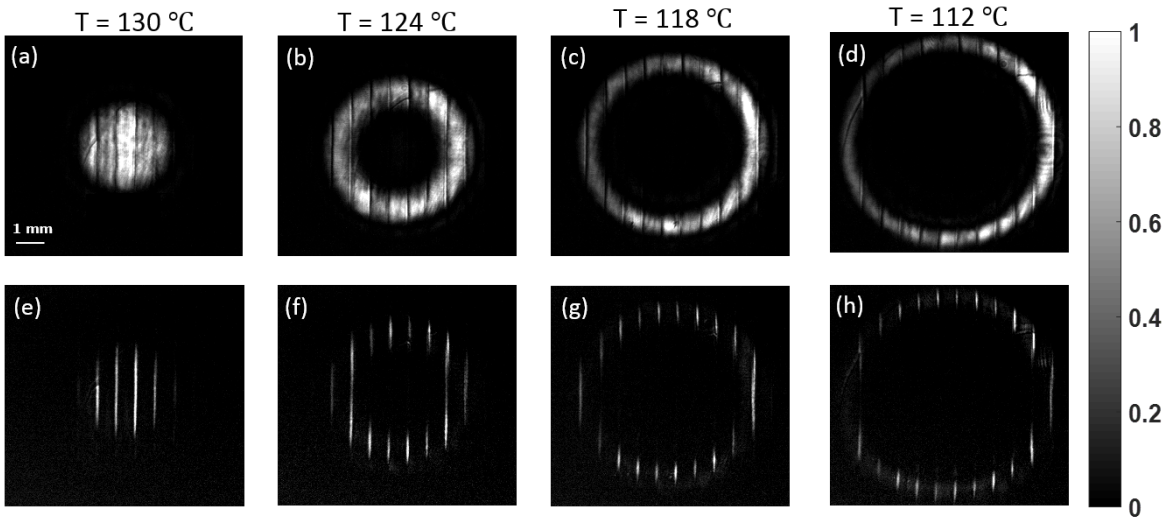

Figure 6.4: *Upconverted images of a binary phase grating object using a monochromatic light source at 1064 nm for various operating temperatures of the PPLN crystal of the upconversion based dark field imaging system. (a-d) and (e-h) correspond to upconverted images in the absence and presence of the spiral phase filter with $m = 2$ for the 1575 nm pump beam, respectively. Scale bar is 1 mm on the object plane.*

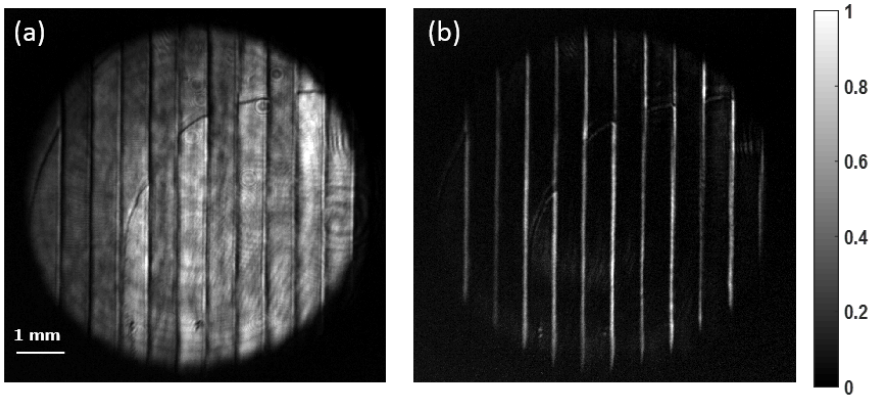

Figure 6.5: *Stitched upconverted images of a binary phase grating object using a monochromatic light source at 1064 nm, based on figure 6.4*

Figure 6.5 represents post-processed monochromatic upconverted images with (Fig. 6.5(b)) and without (Fig. 6.5(a)) spiral phase filter, based on the individual images shown in Fig. 6.4. Figure 6.6 illustrates the calculated phase-matching curves for a PPLN crystal with a poling period of 11.835 µm at different crystal operating temperatures. Dashed line depicts the FoV covered by varying temperature from $T = 130°C$ to $T = 112°C$ for the case of narrowband 1064 nm illumination source. For the case of

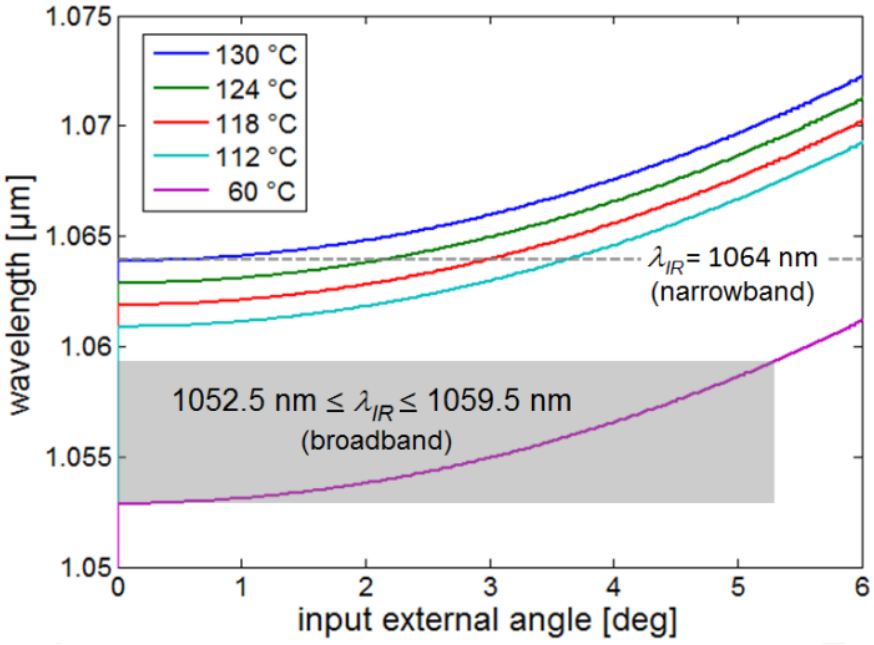

Figure 6.6: *phase-matching curve for PPLN crystal with poling period of 11.835 µm at different temperatures. Intersection points of the curves with the dashed line determine the FoV covered by varying the PPLN temperature from $T = 130°C$ to $T = 112°C$ while using a 1064 nm narrowband illumination source. The gray rectangular region which coincides with the phase-matching curve for PPLN temperature of $T = 60°C$ shows that a large field-of-view ($\theta_{max} = 5.24$ deg) can be achieved for a broadband illumination with a spectral width of 6.4 nm.*

broadband illumination source at PPLN temperature of $T = 60°C$, the relation between FoV and spectral coverage can be estimated.

6.2.3 Broadband illumination

A NIR SC source is also used as an illumination source for upconversion imaging eliminating the need for image post-processing to provide real-time phase contrast (edge-enhanced) imaging with extended FoV. Figures 6.2(a-d) show the simulated upconverted edge-enhanced images of phase-only binary grating, checker-board, and resolution target acquired using broadband illumination i.e. SC source. Figures 6.8(a-d) are the corresponding experimentally obtained images. Whereas, Fig. 6.7 are corresponding images when there is no spiral phase filter used. These images are taken at PPLN temperature of $60°C$ and camera integration time of 100 ms. Visualization 10 shows a real-time video of the upconversion based dark field imaging of a dynamic phase object ($0 - \pi$ binary),

in this case, a spinning globe (@ 10 frames per second) - a representative frame is shown in Fig. 6.8(d) and Fig. 6.7. At 15 s into the visualization, the spiral phase of the pump beam was removed to show the original upconverted image of the dynamic phase object without any spatial filtering (Fig. 6.7(d)).

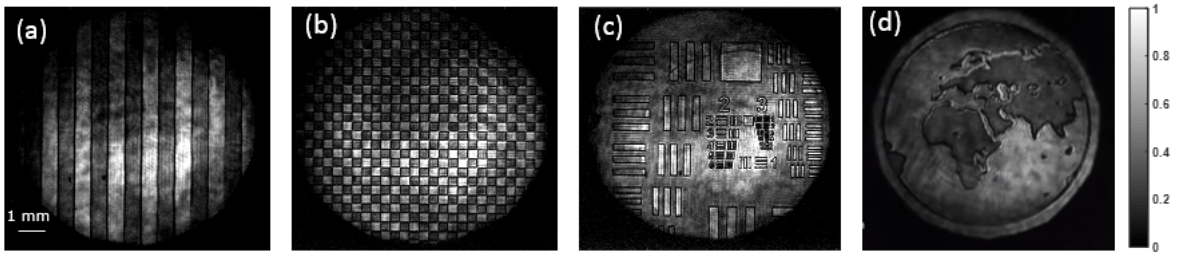

Figure 6.7: *Large field-of-view upconverted images of broadband illuminated SLM with static binary phase objects: (a) grating, (b) checker-board, and (c) resolution target. An integration time of 100 ms is used for each frame acquisition. (d) A representative frame of the upconverted edge-enhanced image of a dynamic phase object, i.e. a spinning globe. Scale bar is 1 mm on the object plane. The large field-of-view corresponds to 6.4 nm effective spectral width of the signal.*

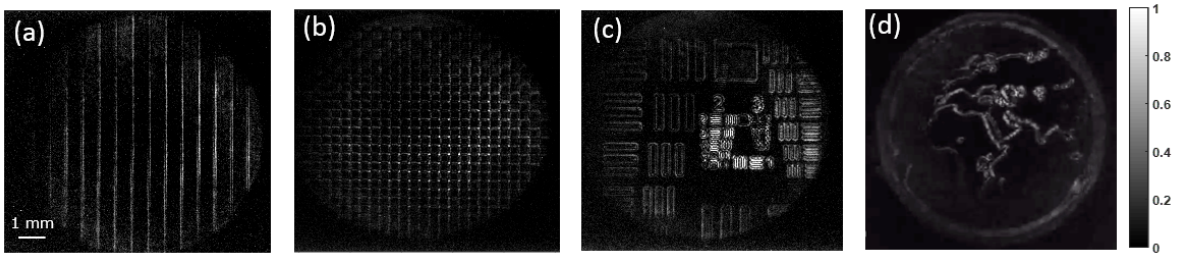

Figure 6.8: *Large field-of-view upconverted images of broadband illuminated SLM with static binary phase objects: (a) grating, (b) checker-board, and (c) resolution target. An integration time of 100 ms is used for each frame acquisition. (d) A representative frame of the upconverted edge-enhanced image of a dynamic phase object, i.e. a spinning globe. Scale bar is 1 mm on the object plane. The large field-of-view corresponds to 6.4 nm effective spectral width of the signal.*

Figure 6.9 represents the upconverted image of a phase-resolution target (0 to π binary phase) when there is no spiral phase filter, see Fig. 6.9(a) and when there is spiral phase filter, see Fig. 6.9(b). If we compare figures acquired using SLM Fig. 6.7 and figure with a static resolution target Fig. 6.9, it can be noted that there is a periodic behavior of intensity at every phase jump in case of SLM, while in case of static phase resolution target, the intensity is homogeneous. This effect is due to the polarization dependence of SLM. Due to the slight tilt of the SLM with respect to the linearly polarized incoming light, the light reflected from SLM gets a slight shift in polarization.

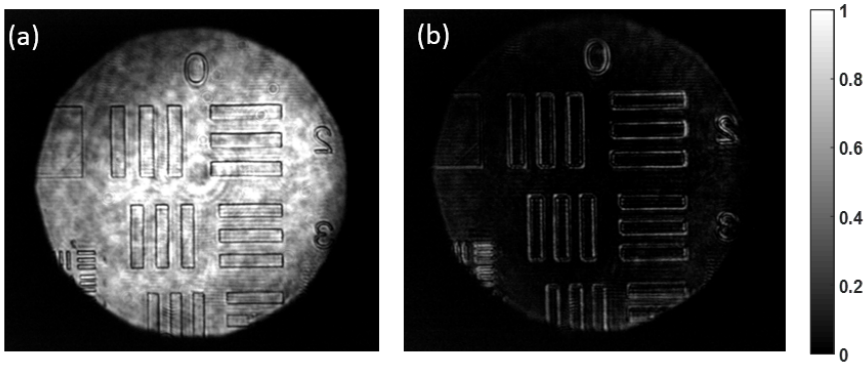

Figure 6.9: *Large field-of-view upconverted images of broadband illuminated static binary phase objects i.e., a resolution target (a) without and (b) with, Spiral phase filter. An integration time of 100 ms is used for each frame acquisition.*

Since the upconversion process is polarization dependent, the result is a slightly different upconversion efficiency for the phase shifted and non-shifted field.

6.2.4 Imaging the Fourier plane

In Fig. 6.10(a-c), three axially displaced planes including the Fourier plane are imaged to inspect the overlap and alignment of the Fourier transform of the object: the checker-board used in Fig. 6.8(b), and the vortex core of the pump beam for optimal high-pass spatial filtering to simultaneously occur with upconversion imaging. The size of the dark core of the pump is manipulated by using a pin-hole in the Fourier plane of 4f-2, as mentioned earlier. The same setup is used to optimally position the PPLN crystal as shown in Fig. 6.10(d).

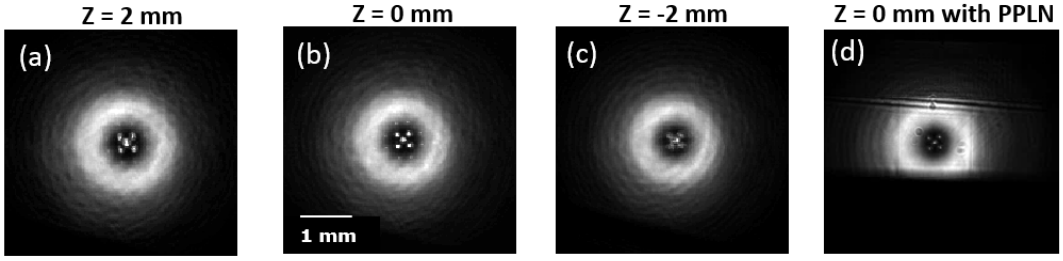

Figure 6.10: *Images showing the well-aligned vortex core of the pump beam with the Fourier transform of the checker-board phase object at different z positions (a-c) without PPLN and (d) with PPLN. $z = 0$ corresponds to the Fourier/focal plane of lens L_1.*

It can be seen in Fig. 6.10 that the object and the pump beam are well aligned and propagate in parallel for z = -2 to 2 mm.

6.3 Additional numerical investigation

6.3.1 Effect of the PPLN crystal aperture size

The 1 mm × 1 mm aperture of the PPLN crystal limits the maximum spatial frequency of the object that can take part in forming the upconverted image. In other words, high spatial frequency components of the object that lie outside the limiting aperture of the PPLN crystal do not get upconverted even if the 1575 nm pump beam incident on the Fourier plane extends beyond the crystal aperture. In the absence of the spiral phase filter, the limited crystal aperture results in blurring of high spatial frequencies of the object. Sharp features that get blurred include phase steps. This is exemplified by the images in Fig. 6.1(a-d) (simulation) and Fig. 6.4(a-d) (experiment), where sharp edges of 0 to π transitions (vice versa) in the object appear in the corresponding upconverted image as dark vertical lines of notable thickness, see Fig. 6.11(i-l). In the presence of the spiral phase filter for the 1575 nm pump, the dark vertical lines are transformed into bright vertical lines over a dark background as shown in Fig. 6.1(e-h) and Fig. 6.4(e-h). Figure 6.11 shows a numerical simulation of the intensity of the pump beam (bounded by the PPLN crystal aperture) and corresponding upconverted images for the same object used in Fig. 6.1 in the collinear case (i.e., $T = 130°C$) but for various PPLN aperture sizes. The 1575 nm pump beam images in Fig. 6.11(a-d) and Fig. 6.11(e-h) correspond to the case in the absence and presence of the spiral phase filter, respectively, in the mid-plane of the nonlinear crystal. Upconverted images in Fig. 6.11(i-l) and Fig. 6.11(m-p) correspond to the pump beam shown in Fig. 6.11(a-d) and Fig. 6.11(e-h), respectively. Numerical results show that as the crystal aperture increases, the thickness of dark vertical lines in the upconverted image (for the case without SPC filter) diminishes i.e., boundaries between 0 and π phase regions become less and less apparent as expected for a pure phase object. For the case with the spiral phase filter, the contrast of the edge-enhanced upconverted images increases as the crystal aperture is enlarged as it no longer truncates the 1575 nm pump beam. Further increase in crystal aperture size does not appreciably improve the image contrast as the finite width of the pump beam now limits the maximum spatial frequency of the object that can be upconverted.

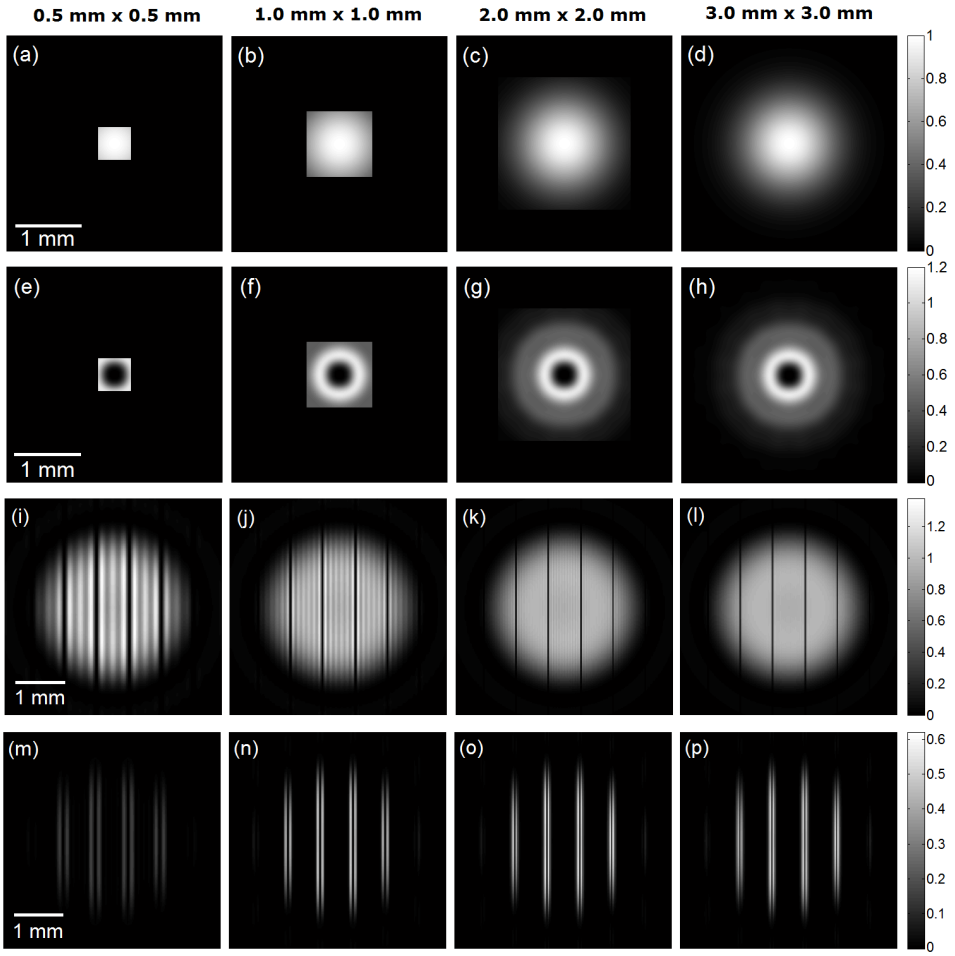

Figure 6.11: *(a)-(d) Lateral intensity profiles of the 1575 nm pump beam in the middle of the PPLN crystal in the absence of the spiral phase filter for increasing crystal aperture sizes (see column labels). (e)-(h) Same as in (a)-(d) but in the presence of $m = 2$ spiral phase filter (and using a pin-hole with radius $r_{PH} = 75$ μm as spatial filter to resize the dark core of the pump). (i)-(l) Upconverted images corresponding to the pump profiles in (a)-(d). (m)-(p) Edge-enhanced upconverted images corresponding to the pump profiles in (e)-(h).*

6.3.2 Effect of the pump beam vortex core size

Using numerical simulation, we have also investigated the effects of varying the dark core size of the pump beam on the resulting upconverted edge-enhanced images when using $m = 2$. As discussed in the previous sections, the size of the pump beam vortex core can be increased by decreasing the pin-hole radius r_{PH} applied in the Fourier plane of 4f-2 of Fig. 6.3. Figure 6.12(a) shows the horizontal intensity profiles of the pump beam

corresponding to $r_{PH} = 75$ µm, $r_{PH} = 150$ µm, $r_{PH} = 600$ µm, and $r_{PH} \to \infty$ along with the normalized intensity of the Fourier transform of the Gaussian illuminated 0-π binary phase grating object. It is worth noting that this approach for generating donut-shaped beams is more photon-efficient than the use of a central obstruction. Unlike the central obstruction, the spiral phase method redirects most of the photons from the center to the side. Figures 6.12(b-e) and Fig. 6.12(f-i) show the transverse intensity profiles of the pump and the corresponding upconverted edge-enhanced images, respectively, for the different pin-hole radii. For $r_{PH} = 75$ µm, the size of the pump vortex core is sufficiently large to suppress the upconversion of the +1 and -1 orders but also (to some degree) the +3 and -3 orders of the 1064 nm object (depending on the object). For $r_{PH} = 150$ µm, the vortex core size is decreased allowing the +3 and -3 orders to enhance its contribution in forming the upconverted image. However, for $r_{PH} = 600$ µm, the vortex core becomes too small such that the +1 and -1 orders strongly contributes in the resulting upconverted image. The +1 and -1 orders correspond to relatively low spatial frequency components and when unsuppressed, their contribution destroys the dark-background edge-enhancement of the upconverted image. Further increase in r_{PH} (i.e., decrease in vortex core size) results in an upconverted image with no edge-enhancement.

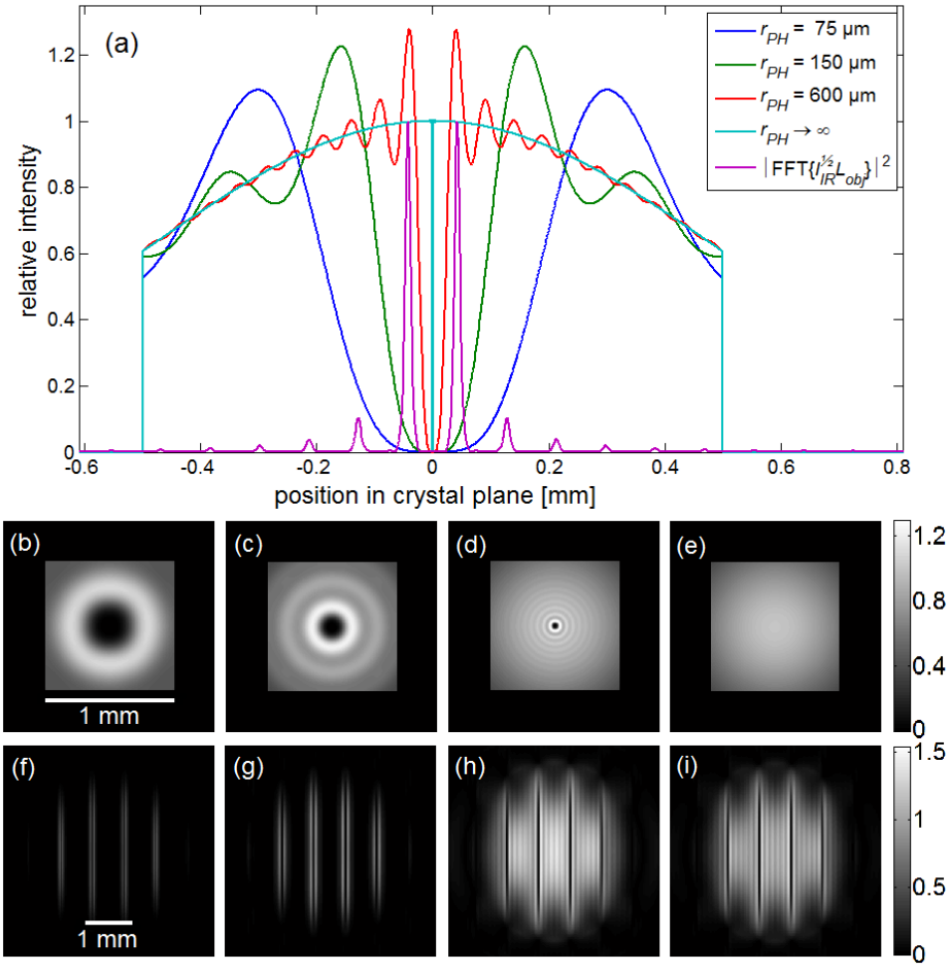

Figure 6.12: *Numerical intensity profiles of the 1575 nm pump beam along the horizontal axis of the Fourier plane (in the middle of the* $1\ mm \times 1\ mm$ *aperture PPLN crystal of the upconversion 4f imaging system) for different pin-hole radius* r_{PH} *used to manipulate the size of the dark core of the pump. The normalized intensity profile of the Fourier transform of a Gaussian illuminated binary phase grating object field (grating period = 0.75 mm as in the experiment) is also included (violet curve) to compare the size of the pump beam's dark core with the position of the spatial frequency components of the object. The horizontal axis lies in the Fourier (crystal) plane and is directly proportional to the object field spatial frequency* f_x*. (b)-(e) Lateral intensity profiles of the pump beam in the middle of the PPLN crystal and (f)-(i) upconverted edge-enhanced images for the case of* $r_{PH} = 75\ \mu m$*,* $r_{PH} = 150\ \mu m$*,* $r_{PH} = 600\ \mu m$*, and* $r_{PH} \to \infty$*, respectively. Fourier lens focal length* $f_1 = 60\ mm$*,* $IR = 1064\ nm$*, and PPLN crystal temperature* $T = 130°C$ *were assumed.*

6.4 Summary

This work is, to the best of our knowledge, the first demonstration of the PSF engineering in upconversion imaging with large field of view, exploiting collinear and non-collinear interaction of the signal and pump fields for SFG. Periodically poled lithium niobate crystal is used as a nonlinear medium for SFG and a 1575 nm erbium-doped fiber laser as a pump source in combination with either of two illumination sources, i.e., narrow band 1064 nm DPSS laser or broadband NIR SC source. A combination of a SVHWP and two QWPs are used in the pump beam path to generate an optical vortex ($m = 2$) and an LCOS-SLM is used to generate static/dynamic phase objects to be upconverted. A numerical model is formulated for upconversion spiral phase contrast/dark field imaging and simulated edge-enhanced images are presented which are in good agreement with experimental results.

When using narrow band illumination, temperature tuning of the PPLN crystal is exploited for non-collinear phase-matching, which when used with image post-processing results in an order of magnitude increase in the field-of-view area. Upconversion based edge-enhanced images with broadband illumination are also presented, providing enlarged field-of-view at fixed temperature, eliminating the need for post-processing. This makes it possible to achieve upconversion based dark field imaging of dynamic phase objects in real-time (i.e., video rates). In addition, the effects of the dimensions of the nonlinear crystal and the size of the dark core of the spiral phase pump beam are discussed. Even larger field-of-view can be achieved by using larger illumination beam diameter and increase in both nonlinear crystal aperture size and pump beam size can result in better spatial resolution.

This work paves the way for transferring dark field imaging or edge detection of phase and amplitude objects (e.g., as a bio-imaging modality in the mid-IR [66]) at various spectral regimes only by manipulating the pump beam or PSF engineering at a fixed wavelength, eliminating the need for broadband IR phase modulators.

7 Conclusion

Upconversion technology is emerging as a promising technique for mid infrared detection due to its high sensitivity and cost efficiency. The focus of this work is primarily mid infrared hyperspectral imaging based on upconversion, in several wavelength regimes.

7.1 Summary of Thesis Achievements

In the first part of this work, long wavelength mid infrared (5 to 10 µm) hyperspectral imaging based on upconversion, to the best of our knowledge, is demonstrated, for the first time. AGS crystal is used as a nonlinear medium due to its broad transparency range [67]. A broadband incoherent, thermal light source i.e. a globar is used as the illumination source and a 1064 nm DPSS laser as a mixing source. The phase-matching condition is scanned via crystal rotation with respect to to its $\vec{c}$-axis which leads to a series of polychromatic images with radial spectral distribution. A post-processing algorithm is developed to achieve a series of monochromatic images, i.e. a hyperspectral cube. In the next step, the illumination source is replaced by a coherent narrowband light source i.e. a QCL with spectral tunability from 5.9 to 6.19 µm. A comparative study of both light sources as the illumination source for the upconversion process is presented based on several parameters such as, spectral resolution, spatial resolution and post-processing algorithm. Globar, due to its low intensity, offers slow acquisition of images. Using the same upconversion module with a globar as the illumination source, the integration time of the camera was set to 500 ms whereas using a QCL leads to 50 times faster image acquisition per frame i.e. 10 ms. However globar, being a broadband source has the advantage of faster acquisition of whole set of data by a single sweep of crystal rotation angle, whereas, in case of QCL the process has to be repeated for every wavelength. The monochromatic image acquisition algorithm is more straight forward in case of narrowband illumination, compared to broadband sources where the deconvolution of every wavelength contribution is acquired based on the phase-matching, before summing up the individual wavelength contribution to form monochromatic images. Using a narrowband illumination source for upconversion based hyperspectral imaging has the advantage of a constant spectral resolution of the image based on the linewidth of the

source itself whereas in case of a broadband source, the spectral resolution is set by the acceptance bandwidth of the upconversion device itself even leading to radially varying spectral resolution within a single image.

In the second task of the project, an upconversion imaging system is developed based on a picosecond pulsed OPO, tunable from 2 to 4 µm spectral regime. The high upconversion efficiency was obtained using a passively synchronized pumping setup. Bulk Lithium Niobate is used as a nonlinear medium, mounted on a galvano-scanner for fast rotation synchronous to camera integration time. This led to monochromatic mid-IR imaging system based on upconversion with an enlarged field of view, operating at video frame-rate (40 Hz), without the need for post-processing of the images. 64 kpixels in the upconverted image were obtained, applying an only 1 degree of crystal rotation exploiting tangential phase-matching. This result is in good agreement with the theoretical estimate resolution. The FoV was increased by a factor of 5 compared to a static design, corresponding to an increase of 25 times in the number of pixels. This number can be further increased by applying a larger numerical aperture at the input side, combined with a correspondingly larger crystal rotation angle. Eventually, the angular interrogation of the nonlinear crystal for upconversion will be limited by image distortion, originating from refraction at the crystal surfaces (see section 2.1.6). Two different examples have been presented, highlighting the potential for on-line IR imaging of gases and fast biopsy screening by measuring disease specific compositional changes.

In the last section of the project, dark field imaging is presented based on upconversion technology. The pump beam profile was modified/engineered for spatial filtering of the object (static/dynamic, phase/amplitude) field, for both, collinear and non-collinear interaction of the input fields. Two kinds of light sources are used for the demonstration of the principle i.e., monochromatic 1064 nm DPSS and near infrared supercontinuum source. A PPLN crystal is used as a nonlinear medium with the mixing field at 1575 nm. A theoretical model is developed which is in good agreement with the experimental results.

7.2 Outlook

Upconversion based mid infrared detection can be transferred to any wavelength regime, limited by the nonlinear medium. In this work, the wavelength regime from approx. 1 to 10 µm has been covered using different nonlinear mediums such as, $AgGaS_2$ (AGS), bulk $LiNbO_3$ and periodically poled lithium niobate. Lithium niobate has transparency range of upto 4 µm [68] whereas AGS is transparent upto 12 µm [69]. Beyond 12 µm, $AgGaSe_2$ can be used which has transparency range of upto 20 µm [70]. Upconversion

based detection has not been demonstrated in this wavelength regime so far which can be of significant interest for many applications in life sciences and gas sensing.
For imaging of the biological samples, it is very important to have high spatial resolution (on the level of cellular level) which is limited by the wavelength (diffraction limited). In case of upconversion imaging the spatial resolution is limited by the crystal aperture size which acts as a mask in the Fourier domain of the upconversion imaging setup. In this work, this limitation was compensated by constructing a magnification setup (telescope) in front of the biopsy sample which consequently reduces the field of view. However, this limitation can be mitigated by exploiting nonlinear crystals of larger aperture sizes [71], which will accept more spatial frequencies for upconversion in the Fourier domain.

Mid-infrared light sources are integral part of the upconversion imaging system. The video-frame rate upconversion system demonstrated during this project relies on an OPO mid infrared light source. The wavelength tuning in a typical OPO is achieved by temperature tuning of the of the nonlinear crystal which is a slow process and makes acquiring a hyperspectral cube a time consuming process. Therefore there is a need for the bright, narrow linewidth mid infrared light sources with fast spectral tuning. QCLs can be considered as a candidate for this purpose but provide with lower brightness than OPOs and might prohibit its use as an illumination source for video-frame rate upconversion based hyperspectral imaging.

Moreover, exploiting more sophisticated imaging optics, such as high NA objectives may help in achieving diffraction limited spatial resolution of the upconversion based images. The technology has the potential to be listed as state-of-the-art in the future for mid-infrared hyperspectral imaging and can be considered at par with well established/commercialized technologies such as FTIR.

Bibliography

[1] D. C. Fernandez, R. Bhargava, S. M. Hewitt, and I. W. Levin, "Infrared spectroscopic imaging for histopathologic recognition", Nat. Biotechnol. **23**, 469 (2005).

[2] A. Travo, O. Piot, R. Wolthuis, C. Gobinet, M. Manfait, J. Bara, M.-E. Forgue-Lafitte, and P. Jeannesson, "IR spectral imaging of secreted mucus: A promising new tool for the histopathological recognition of human colonic adenocarcinomas", Histopathology **56**, 921 (2010).

[3] H. Amrania, G. Antonacci, C.-H. Chan, L. Drummond, W. R. Otto, N. A. Wright, and C. Phillips, "Digistain: A digital staining instrument for histopathology", Opt. Express **20**, 7290 (2012).

[4] R. Bhargava, "Infrared spectroscopic imaging: The next generation", Appl. Spectrosc. **66**, 1091 (2012).

[5] J. Nallala, G. R. Lloyd, M. Hermes, N. Shepherd, and N. Stone, "Enhanced spectral histology in the colon using high-magnification benchtop FTIR imaging", Vib. Spectrosc. **91**, 83 (2017).

[6] J. Houghton, "Global warming", Rep. Prog. Phys. **68**, 1343 (2005).

[7] M. N. Abedin, M. G. Mlynczak, and T. F. Refaat, "Infrared detectors overview in the short-wave infrared to far-infrared for CLARREO mission", in Infrared remote sensing and instrumentation XVIII, edited by M. Strojnik, and G. Paez, (Aug. 2010).

[8] J. Li, U. Parchatka, R. Königstedt, and H. Fischer, "Real-time measurements of atmospheric CO using a continuous-wave room temperature quantum cascade laser based spectrometer", Opt. Express **20**, 7590 (2012).

[9] D. Wang, S. Liang, T. He, and Q. Shi, "Estimating clear-sky all-wave net radiation from combined visible and shortwave infrared (VSWIR) and thermal infrared (TIR) remote sensing data", Remote Sens. Environ. **167**, 31 (2015).

[10] F. D. van der Meer, H. M. A. van der Werff, F. J. A. van Ruitenbeek, C. A. Hecker, W. H. Bakker, M. F. Noomen, M. van der Meijde, E. J. M. Carranza, J. B. de Smeth, and T. Woldai, "Multi- and hyperspectral geologic remote sensing: A review", Int. J. Appl. Earth Obs. Geoinf. **14**, 112 (2012).

[11] D.-W. Sun, *Hyperspectral imaging for food quality analysis and control* (Elsevier, 2010).

[12] A. Rogalski, *Infrared detectors* (CRC Press, 2010).

[13] F. Penaranda, V. Naranjo, L. Kastl, B. Kemper, G. R. Lloyd, J. Nallala, N. Stone, and J. Schnekenburger, "Multivariate classification of Fourier transform infrared hyperspectral images of skin cancer cells", in 24th European signal processing conference (EUSIPCO) (Aug. 2016).

[14] H. F. Grahn, and P. Geladi, *Techniques and applications of hyperspectral image analysis* (Wiley, 2007), 368 pp.

[15] J. S. Dam, P. Tidemand-Lichtenberg, and C. Pedersen, "Room-temperature mid-infrared single-photon spectral imaging", Nat. Photonics **6**, 788 (2012).

[16] J. Midwinter, "Image conversion from 1.6 µm to the visible in lithium niobate", IEEE Journal of Quantum Electronics **4**, 319 (1968).

[17] J. Warner, "Spatial resolution measurements in up-conversion from 10.6 µm to the visible", Appl. Phys. Lett. **13**, 360 (1968).

[18] M. Mathez, P. J. Rodrigo, P. Tidemand-Lichtenberg, and C. Pedersen, "Upconversion imaging using short-wave infrared picosecond pulses", Opt. Lett. **42**, 579 (2017).

[19] L. M. Kehlet, P. Tidemand-Lichtenberg, J. S. Dam, and C. Pedersen, "Infrared upconversion hyperspectral imaging", Opt. Lett. **40**, 938 (2015).

[20] L. M. Kehlet, N. Sanders, P. Tidemand-Lichtenberg, J. S. Dam, and C. Pedersen, "Infrared hyperspectral upconversion imaging using spatial object translation", Opt. Express **23**, 34023 (2015).

[21] L. Huot, P. M. Moselund, P. Tidemand-Lichtenberg, L. Leick, and C. Pedersen, "Upconversion imaging using an all-fiber supercontinuum source", Opt. Lett. **41**, 2466 (2016).

[22] J. S. Dam, C. Pedersen, and P. Tidemand-Lichtenberg, "Theory for upconversion of incoherent images", Opt. Express **20**, 1475 (2012).

[23] S. Junaid, P. J. Rodrigo, P. Tidemand-Lichtenberg, and C. Pedersen, "Point-spread function engineering in upconversion imaging", in High-brightness sources and light-driven interactions (2018).

[24] X. Qiu, F. Li, W. Zhang, Z. Zhu, and L. Chen, "Spiral phase contrast imaging in nonlinear optics: Seeing phase objects using invisible illumination", Optica **5**, 208 (2018).

[25] L. E. Garn, "Fundamental noise limits of thermal detectors", J. Appl. Phys. **55**, 1243 (1984).

[26] C. Draijer, and T. Dalsa, "Microbolometers move thermal imaging into next-gen commercial uses", Photonics Spectra **48**, 58 (2014).

[27] T. P. Pearsall, and M. A. Pollack, "Compound semiconductor photodiodes", in *Semiconductors and semimetals*, Vol. 22, edited by W. T. Tsang, (Elsevier S&T, 1985) Chap. 2, pp. 174–241.

[28] F. Sizov, Z. Tsybrii, V. Zabudsky, O. Golenkov, V. Petryiakov, S. Dvoretsky, N. Michailov, A. Shevchik-Shekera, I. Lysiuk, and E. Dieguez, "Mercury-cadmium-telluride thin layers as subterahertz and infrared detectors", Opt. Eng. **54**, 127102 (2015).

[29] J. T. Wimmers, and D. S. Smith, "Characteristics of InSb photovoltaic detectors at 77K and below", in Technologies of cryogenically cooled sensors and Fourier transform spectrometers II, edited by R. J. Huppi, (Aug. 1983).

[30] B. V. Eerdenbrugh, and L. S. Taylor, "Application of mid-IR spectroscopy for the characterization of pharmaceutical systems", Int. J. Pharm. **417**, 3 (2011).

[31] P. R. Griffiths, J. A. D. Haseth, and J. D. Winefordner, *Fourier transform infrared spectrometry* (Wiley, 2007), 700 pp.

[32] J. Faist, F. Capasso, D. L. Sivco, C. Sirtori, A. L. Hutchinson, and A. Y. Cho, "Quantum cascade laser", Science **264**, 553 (1994).

[33] D. Heydari, Y. Bai, N. Bandyopadhyay, S. Slivken, and M. Razeghi, "High brightness angled cavity quantum cascade lasers", Appl. Phys. Lett. **106**, 091105 (2015).

[34] O. Fedosenko, M. Chashnikova, S. Machulik, J. Kischkat, M. Klinkmüller, A. Aleksandrova, G. Monastyrskyi, M. P. Semtsiv, and W. T. Masselink, "Scaling the output power of quantum-cascade lasers with a number of cascades", J. Cryst. Growth **323**, 484 (2011).

[35] A. Hugi, R. Terazzi, Y. Bonetti, A. Wittmann, M. Fischer, M. Beck, J. Faist, and E. Gini, "External cavity quantum cascade laser tunable from 7.6 to 11.4 µm", Appl. Phys. Lett. **95**, 061103 (2009).

[36] W. T. Masselink, M. P. Semtsiv, A. Aleksandrova, and S. Kurlov, "Power scaling in quantum cascade lasers using broad-area stripes with reduced cascade number", Opt. Eng. **57**, 1 (2017).

[37] R. Centeno, D. Marchenko, J. Mandon, S. M. Cristescu, G. Wulterkens, and F. J. M. Harren, "High power, widely tunable, mode-hop free, continuous wave external cavity quantum cascade laser for multi-species trace gas detection", Appl. Phys. Lett. **105**, 261907 (2014).

[38] N. Bandyopadhyay, M. Chen, S. Sengupta, S. Slivken, and M. Razeghi, "Ultra-broadband quantum cascade laser, tunable over 760 cm^{-1}, with balanced gain", Opt. Express **23**, 21159 (2015).

[39] W. Zhou, N. Bandyopadhyay, D. Wu, R. McClintock, and M. Razeghi, "Monolithically, widely tunable quantum cascade lasers based on a heterogeneous active region design", Sci. Rep. **6**, 25213 (2016).

[40] S. Slivken, A. Evans, J. David, and M. Razeghi, "High-average-power, high-duty-cycle ($\lambda \sim 6$ µm) quantum cascade lasers", Appl. Phys. Lett. **81**, 4321 (2002).

[41] I. Howieson, "Quantum-cascade lasers smell success", Laser Focus World **41** (2005).

[42] R. Maulini, M. Beck, J. Faist, and E. Gini, "Broadband tuning of external cavity bound-to-continuum quantum-cascade lasers", Appl. Phys. Lett. **84**, 1659 (2004).

[43] R. H. Kingston, "Parametric amplification and oscillation at optical frequencies", Proceedings of the Institute of Radio Engineers **50**, 472 (1962).

[44] J. A. Giordmaine, and R. C. Miller, "Tunable coherent parametric oscillation in $LiNbO_3$ at optical frequencies", Phys. Rev. Lett. **14**, 973 (1965).

[45] M. Ebrahim-Zadeh, and S. C. Kumar, "Yb-fiber-laser-pumped ultrafast frequency conversion sources from the mid-infrared to the ultraviolet", IEEE Journal of Selected Topics in Quantum Electronics **20**, 624 (2014).

[46] R. W. Boyd, *Nonlinear optics* (Elsevier, 2008), 640 pp.

[47] S. Junaid, J. Tomko, M. P. Semtsiv, J. Kischkat, W. T. Masselink, C. Pedersen, and P. Tidemand-Lichtenberg, "Mid-infrared upconversion based hyperspectral imaging", Opt. Express **26**, 2203 (2018).

[48] P. Tidemand-Lichtenberg, J. S. Dam, H. V. Andersen, L. Høgstedt, and C. Pedersen, "Mid-infrared upconversion spectroscopy", J. Opt. Soc. Am. B **33**, D28 (2016).

[49] C. Pedersen, Q. Hu, L. Høgstedt, P. Tidemand-Lichtenberg, and J. S. Dam, "Non-collinear upconversion of infrared light", Opt. Express **22**, 28027 (2014).

[50] J. W. Goodman, *Introduction to Fourier optics* (McGraw-Hill, 1996).

[51] C. Pedersen, E. Karamehmedović, J. S. Dam, and P. Tidemand-Lichtenberg, "Enhanced 2D-image upconversion using solid-state lasers", Opt. Express **17**, 20885 (2009).

[52] J. W. Goodman, "Optical methods for suppressing speckle", in *Speckle phenomena in optics* (Roberts and Company Publishers, 2006) Chap. 5, pp. 141–187.

[53] M. J. T. Milton, T. J. McIlveen, D. C. Hanna, and P. T. Woods, "High-efficiency infrared generation by difference-frequency mixing using tangential phase matching", Opt. Commun. **87**, 273 (1992).

[54] G. C. Bhar, S. Das, and P. K. Datta, "Tangentially phase-matched infrared detection in $AgGaS_2$", J. Phys. D: Appl. Phys. **27**, 228 (1994).

[55] M. Ritsch-Marte, "Spiral phase contrast microscopy", in *Twisted photons: application of light with orbital angular momentum* (Wiley, 2011) Chap. 8, pp. 143–154.

[56] V. V. Kotlyar, H. Elfstrom, J. Turunen, A. A. Almazov, S. N. Khonina, and V. A. Soifer, "Generation of phase singularity through diffracting a plane or Gaussian beam by a spiral phase plate", J. Opt. Soc. Am. A **22**, 849 (2005).

[57] H. Maestre, A. J. Torregrosa, and J. Capmany, "IR image upconversion using band-limited ASE illumination fiber sources", Opt. Express **24**, 8581 (2016).

[58] S. Junaid, P. Tidemand-Lichtenberg, and C. Pedersen, "Upconversion based spectral imaging in 6 to 8 µm spectral regime", in Nonlinear frequency generation and conversion: Materials and devices XVI, edited by K. L. Vodopyanov, and K. L. Schepler, (Feb. 2017).

[59] R. Andrews, "Wide angular aperture image up-conversion", IEEE Journal of Quantum Electronics **5**, 548 (1969).

[60] R. Demur, R. Garioud, A. Grisard, E. Lallier, L. Leviandier, L. Morvan, N. Treps, and C. Fabre, "Near-infrared to visible upconversion imaging using a broadband pump laser", Opt. Express **26**, 13252 (2018).

[61] R. Bhargava, "Simultaneous cancer and tumor microenvironment subtyping using confocal infrared microscopy for all-digital molecular histopathology", Proceedings of the National Academy of Sciences **115**, E5651 (2018).

[62] K. Gerwert, "Quantum cascade laser-based infrared microscopy for label-free and automated cancer classification in tissue sections", Sci. Rep. **8**, 2045 (2018).

[63] F. Zernike, "Phase contrast, a new method for the microscopic observation of transparent objects", Physica **9**, 686 (1942).

[64] S. Fürhapter, A. Jesacher, S. Bernet, and M. Ritsch-Marte, "Spiral phase contrast imaging in microscopy", Opt. Express **13**, 689 (2005).

[65] J. Xin, K. Dai, L. Zhong, Q. Na, and C. Gao, "Generation of optical vortices by using spiral phase plates made of polarization dependent devices", Opt. Lett. **39**, 1984 (2014).

[66] K. Haase, N. Kröger-Lui, A. Pucci, A. Schönhals, and W. Petrich, "Real-time mid-infrared imaging of living microorganisms", J. Biophotonics **9**, 61 (2015).

[67] E. Takaoka, and K. Kato, "Thermo-optic dispersion formula for $AgGaS_2$", Appl. Opt. **38**, 4577 (1999).

[68] E. V. Stryland, "Handbook of optics", in (MicGraw-Hill Education, 2009).

[69] F. Rotermund, and V. Petrov, "Femtosecond noncollinear optical parametric amplification in the mid-infrared range with 1.25 µm pumping", Japanese Journal of Applied Physics **40**, 3195 (2001).

[70] D. A. Roberts, "Dispersion equations for nonlinear optical crystals: KDP, $AgGaSe_2$, and $AgGaS_2$", Appl. Opt. **35**, 4677 (1996).

[71] M. Thirumavalavan, S. Sitharaman, S. Ravi, L. Durai, N. L. Jagota, R. C. Narula, and R. Thyagarajan, "Growth of large diameter lithium niobate single crystals by czochralski method", Ferroelectrics **102**, 15 (1990).

[72] L. Dong, Y. Yu, C. Li, S. So, and F. K. Tittel, "Ppb-level formaldehyde detection using a CW room-temperature interband cascade laser and a miniature dense pattern multipass gas cell", Opt. Express **23**, 19821 (2015).

[73] B. E. A. Saleh, and M. C. Teich, "Guided-wave optics", in *Fundamentals of photonics* (Wiley, 2001) Chap. 8, pp. 289–325.

[74] J.-M. Melkonian, M. Raybaut, A. Godard, J. Petit, and M. Lefebvre, "Time-resolved spectral characterization of a pulsed external-cavity quantum cascade laser", in Optics and photonics for counterterrorism, crime fighting, and defence VIII, edited by C. Lewis, and D. Burgess, (Oct. 2012).